Characterization of Labor: a Magnetomyography Approach

Dissertation
der Matematisch-Naturwissenschaftlichen Fakultät
der Eberhard Karls Universität Tübingen
zur Erlangung des Grades eines
Doktors der Naturwissenschaften
(Dr. rer. nat.)

vorgelegt von
Dipl. -Ing. Adrian Furdea
aus Carei, Rumänien

Tübingen
2012

Tag der mündlichen Qualifikation:	16.08.2012
Dekan:	Prof. Dr. Wolfgang Rosenstiel
1. Berichterstatter:	Prof. Dr. Wolfgang Rosenstiel
2. Berichterstatter:	Prof. Dr. Niels Birbaumer

Summary

Premature labor and delivery is a major cause of infant mortality and morbidity. Advances in the fields of medicine and engineering together with a better understanding of the preterm birth related risk factors have successfully reduced their incidence. Despite such advances, in most developed countries the preterm birth rate is still high, accounting for about 85% of infant mortality and more than 50% of the surviving infant's morbidity. The timely prediction of premature labor and delivery can improve the effectiveness of the required treatments. Unfortunately, the techniques employed in current obstetrical practice proved to be inaccurate for the prediction of premature labor and delivery.

The contractile element of the uterus is the myometrium, which consists of smooth muscle cells. The electrical activity (always accompanied by magnetic activity) in form of action potentials (AP) propagates through the myometrial cells causing the contraction of the uterus. Magnetomyography (MMG) is the noninvasive measurement of the uterine magnetic activity by means of equally spaced magnetic sensors arranged in a concave array. The MMG recordings display advantages which renders them suitable for the analysis and characterization of the uterine activity. Compared to electromyography signals, the MMG signals are detectable outside the boundary of the skin without making any contact with the body. Also they are independent on conductivity geometry, i.e. tissue conductivity. The measured electrical activity arises from volume currents flowing (in the body) to the electrode sites and not directly due to the primary current generators.

The current work presents a set of methods designated to identify and characterize uterine contractile activity and its dynamics in MMG signals. The basic process controlling the uterine contraction is the underlying electrical activity in the form of APs which propagate between muscle cells and open ion channels allowing the influx of calcium ions to produce a

contraction. APs occur in groups and form a burst of activity which in humans can last more than a minute. The ultimate goal is to provide a timely prediction of delivery. More precisely, a multi-sensor analysis of the spatial propagation properties of the MMG signals is carried out to identify time segments of uterine burst activity. This type of analysis is of particular relevance because the spreading of magnetic activity in the myometrium results in coordinated contractions (close to term), capable to push the fetus into the birth canal and ultimately lead to delivery. Therefore, the analysis of the spatial propagation properties (within segments of contractile activity), i.e. conduction velocity (CV), could provide a fundamental contribution for the prediction of delivery.

First, a multi-stage approach is introduced wherein Hilbert and Wavelet transforms are employed to automatically identify uterine contraction bursts in MMG data. The signals are decomposed by wavelet analysis into multilevel approximate and detail coefficients. In each level, the signals are reconstructed using the detail coefficients followed by the computation of Hilbert transform, a procedure referred to as the Hilbert transform of the wavelet decomposition (HTWD). To increase the signal to noise ratio, the Hilbert amplitude of the reconstructed signals from different frequency bands (0.1 - 1 Hz) is integrated over all the sensors. Using the affinity propagation clustering technique the contractile bursts are distinguished from the noise level and a single marker for the contractile events is created. The method is applied on simulated MMG data, using a simple stochastic model, to determine its robustness and to seven MMG datasets.

Second, to characterize the dynamics of the contractile activity, a novel approach to calculate the CV of the uterine contraction bursts in MMG signals is introduced. For this purpose, the sensor space is partitioned (according to the x and y coordinates) into four different quadrants (Q) and the contractile bursts are identified at the level of individual sensors using the previously described HTWD approach. The identification is performed within a non-overlapping window and if within the inspection window contractile burst is identified in a quadrant pair (e.g., Q1-2) then the center of gravity (CoG) is computed in each quadrant for each time point (the sum of the product of the sensor coordinates with the Hilbert amplitude of the MMG signals normalized by the sum of the Hilbert amplitude of the signals over all sensors). Following this, the delay between the CoGs is computed

using the high dimension cross-correlation (HDCC) function. This approach is validated by simulating a stochastic model based on independent second-order autoregressive processes (AR2). The proposed approach is applied to serial MMG recordings. The outcomes show an increase in the CV as the subjects approach labor and that it can be considered as a possible predictor of preterm labor.

To conclude, it could be shown that the HTWD approach can be used for the successful identification of uterine contractions. To mark the contractile intervals, a discrete-time binary decision signal was created in each magnetic sensor. The information provided by this approach was further used to determine the CV of the uterine contraction bursts and it was shown that the increase in the CV can be considered as a possible predictor of preterm labor. Significant benefits could be expected from the introduction of MMG signal analysis for routine contraction monitoring. Further clinical validations are required to assess the robustness of the presented methods and to account for physiological differences among subjects.

Zusammenfassung

Frühgeburt ist die Hauptursache für Säuglingssterblichkeit und Säuglingsmorbidität. Die Inzidenz der Frühgeburt konnte durch Fortschritte in der biomedizinischen Forschung und ein besseres Verständnis der Risikofaktoren erfolgreich reduziert werden. Trotz solcher Erfolge, ist die Häufigkeit der Frühgeburt auch in entwickelten Ländern noch hoch und erklärt etwa 85% der Säuglingssterblichkeit und mehr als 50% der überlebenden Säuglingsmorbidität. Eine zeitliche Vorhersage des Eintretens einer Frühgeburt kann die Effektivität der benötigten Behandlungen erhöhen, jedoch sind die gegenwärtig eingesetzten Methoden für die Vorhersage der Frühgeburt zu ungenau.

Das kontraktile Gewebe der Gebärmutter ist das Myometrium, das aus einer glatten Muskulatur besteht. Die elektrische Aktivität (immer begleitet von einer magnetischen Aktivität) in Form von Aktionspotentialen (AP) breitet sich entlang der myometrischen Zelloberfläche aus und verursacht Kontraktionen des Uterus. Die Magnetomyographie (MMG) ist eine nicht invasive Methode für die Messung der magnetischen Aktivität des Uterus. Dabei werden hochsensitive magnetische Sensoren eingesetzt, die es erlauben magnetische Aktivität über das gesamte Abdomen einer Schwangeren zu registrieren. Aus den biomagnetischen Signalen kann die kontraktile Aktivität des Uterus extrahiert werden. Im Vergleich zu elektromyographischen Signalen können MMG Signale auch ohne direkten Kontakt mit der Hautoberfläche erfasst werden. Zusätzlich werden die MMG Signale nicht von der Leitfähigkeit des Gewebes beeinflusst und können auch referenzfrei registriert werden.

In der vorliegenden Arbeit wurden mehrere Methoden entwickelt, implementiert und validiert, die für die Identifizierung und Charakterisierung der kontraktilen Aktivität des Uterus und seiner Dynamik geeignet sind. Das Hauptziel der Arbeit war die Entwicklung eines Methodensets, das die zeitliche Vorhersage der Geburt ermöglichen kann. Dabei wurde die kontraktile Aktivität anhand einer Multi-Sensor Analyse der räumlich-zeitlichen

Muster der MMG Signale untersucht. Die Ausbreitung der magnetischen Aktivität im Myometrium verursacht koordinierte Kontraktionen (kurz vor der Geburt), die den Fötus in den Geburtskanal drücken und schließlich zur Geburt führen.

In einem ersten Analyseschritt wurden Hilbert und Wavelet Transformationen zur Identifizierung der Gebärmutterkontraktionshäufung im MMG Signal eingesetzt. Das Signal wurde mit einer Wavelet Analyse in einem Mehrstufenverfahren in approximierte und detaillierte Koeffizienten zerlegt. Innerhalb jeder Stufe, wurden die Signale mit den detaillierten Koeffizienten rekonstruiert und deren Hilbert Transformation berechnet. Diese Vorgehensweise wurde unter Hilbert-Transformation der Wavelet-Dekomposition (HTWD) zusammengefasst. Um das Signal-Rausch Verhältnis zu erhöhen, wurden die Hilbert-Amplituden der rekonstruierten Signale in unterschiedlichen Frequenzbereichen (0.1 - 1 Hz) über alle Sensoren integriert. Eine Affinity Propagation Clustering Klassifizierung wurde eingesetzt, um die Kontraktionsaktivität vom Rauschen zu differenzieren und einen eigenen Marker für das kontraktile Ereignis zu setzen. Um die Robustheit der Methode zu untersuchen, wurde sie an einem stochastischen Modell mit simulierten MMG Daten getestet. Zusätzlich wurde die Methode an Messdaten von sieben schwangeren Frauen erprobt.

Um die Dynamik der kontraktilen Aktivität zu charakterisieren, wurde im nächsten Schritt ein neuer Ansatz zur Berechnung der Ausbreitungsgeschwindigkeit (conduction velocity - CV) der kontraktilen Aktivität über den Uterus aus den MMG Signalen eingeführt. Dabei wurde der Sensor Raum in vier unterschiedliche Quadranten (Q) aufgeteilt (anhand x und y Koordinaten) und mit Hilfe des vorher erwähnten HTWD Methodenansatzes die Kontraktionsaktivität identifiziert. Die Identifikation wurde in nicht überlappenden Fenstern fester Größe durchgeführt. Wurde innerhalb die Inspektion Fenster Kontraktionsaktivität in einem Quadrant paar (e.g., Q1-2) gefunden, so wurde der Aktivitätsschwerpunkt (center of gravity - CoG) für jeden Quadrant und jeden Zeitpunkt berechnet (die Multiplikation zwischen jede Sensorkoordinate und die Hilbertamplitude des MMG Signals wurde summiert und dann durch die summierte Hilbert Amplitude aller Sensoren geteilt). Danach wird die Verzögerung zwischen den CoGs unter Verwendung der hoch dimensionalen Kreuzkorrelationsfunktion (high dimension cross-correlation - HDCC) berechnet. Dieser

Ansatz wurde durch Simulation eines stochastischen Modells validiert, der auf unabhängigen autoregressiven Prozessen zweiter Ordnung (AR2) basiert. Der vorgeschlagene Ansatz wurde auf serielle MMG Aufnahmen angewandt. Die Ergebnisse zeigten einen Anstieg in der CV in späteren Schwangerschaftswochen. Es wurde auch gezeigt, dass die CV als möglicher Prädiktor für vorzeitige Wehen betrachtet werden kann.

Zusammenfassend wurde gezeigt, dass der HTWD Ansatz für eine erfolgreiche Identifizierung der Wehentätigkeit im MMG Signal verwendet werden kann. Um die kontraktilen Abständen zu markieren, wurde ein zeitdiskretes, binäres Auswahlsignal in jedem magnetischen Sensor erzeugt. Die von diesem Ansatz zur Verfügung gestellten Informationen wurden weiter verwendet, um die CV der kontraktilen Aktivität im Uterus zu bestimmen. Es wurde auch gezeigt, dass die CV als möglicher Prädiktor für vorzeitige Wehen betrachtet werden kann. Der Einsatz der MMG Signalanalyse für die routinemäßige Überwachung der Wehentätigkeit im klinischen Setting könnte wichtige medizinische Nutzen zeigen. Weitere klinische Validierungen, die die physiologische Unterschiede zwischen Probanden berücksichtigen, sind erforderlich, um die Robustheit der vorgestellten Methoden zu bewerten.

To my son and my wife.

Acknowledgements

I would like to thank all people who have helped and inspired me during my doctoral study. I would never have been able to finish my dissertation without the guidance of my supervisors, help from my colleagues and support from my wife, family and friends.

First, I would like to thank Prof. Dr. Wolfgang Rosenstiel for accepting me as his doctoral student, for providing me the opportunity to do research at the Faculty of Science and for his valuable feedback at milestone events.

Prof. Dr. Niels Birbaumer for giving me the opportunity to work at the Institute of Medical Psychology and Behavioral Neurobiology and for providing me with an engaging and challenging research environment.

Dr. Rathinaswamy B. Govindan and Dr. Hubert Preissl for their close supervision, excellent guidance, caring, patience and for sharing their expertise during all these years. Special thanks to the members of the SARA Research Center from Little Rock, Dr. Curtis L. Lowery, Dr. Hari Eswaran, Doug J. Wilson, Srinivasan Vairavan, Pam Murphy, Jessica Temple and Maureen Ware for the very engaging and pleasant collaboration. A big thank you goes to Hubert for letting me drive his fancy car during my time spent at the SARA Research Center.

The fMEG research team in Tübingen, Jana Münssinger, Dr. Isabelle Kiefer, Dr. Rossitza Draganova and Magdalene Weiss.

Prof. Dr. Martin Bogdan for his support and valuable comments during the final preparatory stage of my dissertation.

I would also like to thank my parents, my elder brother and my grandmother for their continuous and intensive support throughout these years. Special thanks also go to my parents in law who also kept encouraging me. I would also like to thank my wife, Tamara for always being on my side, supporting me with kind words and warmth in my time of need.

Last but not least, I wouldn't be able to finish without some wonderful friends to cheer me up and drag me out from time to time from my office. Thank you for being such good friends.

Contents

List of Figures

List of Tables

1

Introduction

It is said that the present is pregnant with the future.
-Voltaire

Premature labor and delivery is an important public health problem as it represents a major and often preventable cause of morbidity and mortality in newborns. Prematurity, often associated with permanent neurodevelopmental disability, occurs when a baby is born before the 37^{th} week of gestation. As a consequence, the immature newborn may require long-term neonatal intensive care at a substantial emotional and financial cost to families and hospitals. According to the European Perinatal Health Report, preterm birth rates varied widely among European countries and ranged from 5.5 to 11.4%, meaning that about half a million babies are born prematurely in Europe every year (Euro-Peristat Project, 2004). The highest percentage of preterm births was registered in Austria (11.4%), followed by Germany (8.9%) and was lowest in Ireland (5.5%) and Lithuania (5.3%). The variation in very preterm births, before 32 weeks of gestation, was less pronounced, and rates for most countries fell within a range of 0.9 to 1.1%. Some of the variation between countries may be due to differences in the way that gestation is determined. According to a previous study, about 85% of infant mortality is accounted for by preterm labor (Maul et al., 2003).
One of the major challenges faced by obstetricians is a proper diagnosis of labor which could be especially useful in the prediction of labor for patients at high risk for premature delivery. To date there is no accurate and objective method available for MMG to predict the onset of labor or to distinguish between false and true labors (Arulkumaran et al., 1991; Garfield et al., 2001; Iams, 2003; Peaceman et al.,

1997; Rabotti et al., 2010a). The objective assessment of uterine activity could also significantly contribute to the timely recognition of eventual complications.

A high percentage of preterm births are the result of either (i) induced delivery or delivery by Caesarean section, also called C-section[1], (ii) spontaneous preterm labor with intact membranes or (iii) preterm premature rupture of the membranes. Common reasons for these types of deliveries are the intrauterine growth restriction (IUGR) or hypertensive disorders of pregnancy, i.e., pre-eclampsia and eclampsia (Goldenberg et al., 2008). IUGR refers to the poor growth of a fetus while still in the mother's uterus. Pre-eclampsia is a medical condition characterized by pregnancy-induced hypertension in the mother accompanied by proteinuria (an excess of serum proteins in the urine). Eclampsia, usually occurring in a patient who already developed pre-eclampsia, is an acute life threatening complication of the pregnancy characterized by the appearance of tonic-clonic seizures.

At present, little is know about the pathogenesis of preterm labor. It is speculated that preterm labor might be the result of either an early idiopathic activation of the normal labor process or the result of pathological insults (Goldenberg et al., 2008; Leman et al., 1999; Maner et al., 2003). To reduce the incidence of preterm delivery, current obstetric interventions focus on inhibiting premature contractions by the administration of tocolytic agents, which temporarily delay the delivery. However, tocolytic therapy involving agents to control the contractibility of the myometrium, e.g. magnesium sulfate and others, is expensive and exposes the patient to unnecessary risks. Therefore, most physicians rely on cervical change before initiating this therapy. In a recent study the use of tocolytic agents is questioned, as their administration fails to demonstrate improvements in neonatal outcome (Kenyon and Peebles, 2011). Instead, the progesterone has been suggested as a future therapeutic candidate to reduce the risk of early birth (Fonseca et al., 2007; Kenyon and Peebles, 2011). However, there is a lack of studies to demonstrate a long-term reduction in neonatal morbidity and mortality from administration of progesterone.

In a review conducted by Garfield and colleagues studies showed that the uterus (myometrium) and cervix pass through a conditioning step in preparation for labor. This step consists of changes in the electrical properties that make muscles more excitable and responsive to produce forceful coordinated contractions (Garfield et al., 2001). At a certain point this process becomes irreversible and delivery cannot be delayed for more than a few days even with tocolytic agents (Garfield et al., 2001).

Preterm labor management is of an even greater concern. Early treatment may result in

[1]For all nomenclatures and abbreviations see the glossary on page 103.

more effective suppression of preterm labor. This often leads to unnecessary treatment and hospitalization of patients who are not in true preterm labor. Accurate diagnosis of preterm labor is only possible through cervical changes such as dilation or effacement. However, even noticeable dynamic cervical change may not be an accurate indicator of true labor, because a high percentage of women with established cervical change do not deliver pre-term when not treated with tocolytics (Cox et al., 1990; Maner et al., 2006). In addition, hospital admissions during false labor are associated with considerably high costs.

Therefore, the development of assessment tools to identify and characterize the course of labor, as well to support accurate prediction of the delivery, would be of great help to physicians.

In order to improve knowledge about the mechanism involved in labor, it is essential to understand the physiological mechanisms that regulate uterine contractions, identify parameters in order to track the stages of labor and relate the changes in such parameters to clinical outcomes.

1.1 The physiology of uterine contractions

1.1.1 Anatomy and biology of the uterus

The uterus is part of the female reproductive system, located inside the pelvis, dorsal to the urinary bladder and ventral to the rectum. The uterus has an important role in the development of the fetus, by providing a safe environment throughout the gestation and later, as term approaches, in the expelling of the fetus through intense contractions.

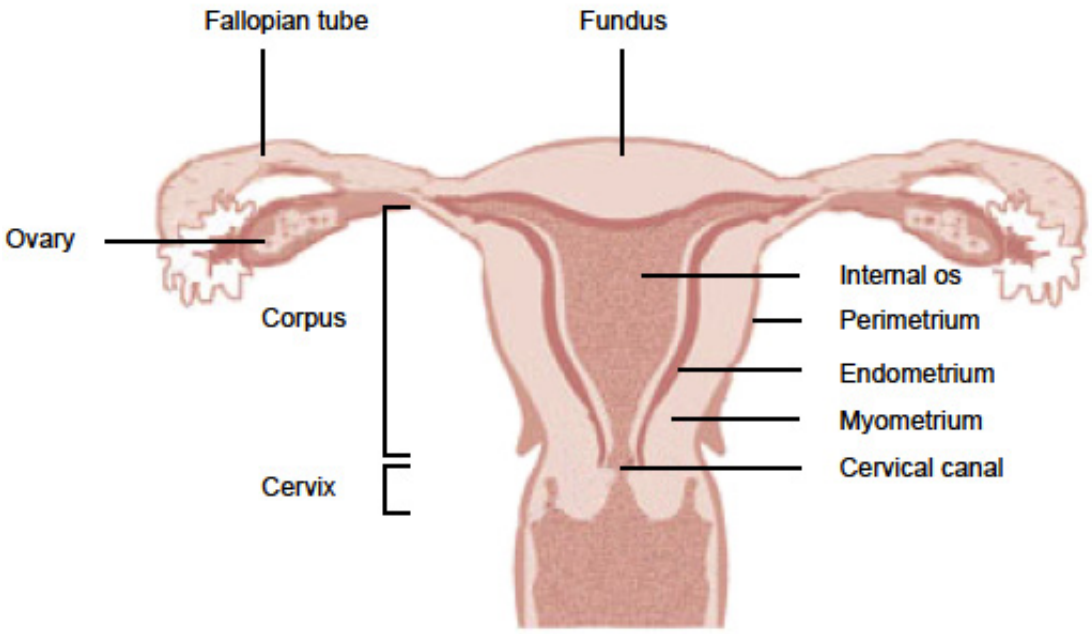

Figure 1.1: Anatomical structure of the non-pregnant uterus. Adapted from the Wikimedia Commons. `http://commons.wikimedia.org/wiki/File:Illu_cervix.jpg`.

The anatomical structure of the human non-pregnant uterus is presented in Figure 1.1. The uterus has a length of approximately 8 cm. Two fallopian tubes enter near its top, dividing the uterus in two parts: the fundus (above the fallopian tubes) and the body (below the fallopian tubes). The narrower, lower end, of the body of the uterus is called the cervix and is made of fibrous connective tissue, with a much firmer consistency compared to the body of the uterus.

The uterine wall (see Figure 1.1) consists of a well-differentiated (i) innermost lining layer also called the endometrium, (ii) a thick muscular inner layer called the myometrium and (iii) an outer layer named the serosa or perimetrium (Chard, 1994).

The myometrium is composed of (i) the outer longitudinal muscle layer and (ii) the inner circular layer. The longitudinal layer consists of bundles of smooth muscle cells which are aligned with the long axis of the uterus. The muscle cells of the circular layer are arranged concentrically but more diffusely around the longitudinal axis of the uterus (Chard, 1994; Csapo, 1954). Early studies have shown that the longitudinal layer is continuous with the circular one and that during pregnancy a coordinated contraction of both layers occurs (Osa and Katase, 1975; Tomiyasu et al., 1988).
For the current work, the particular layer of interest is the myometrium which is responsible for the induction of uterine contractions (Garfield et al., 1998).

1.1.2 Organization of the smooth muscle cell

To understand uterine contractility, a review of the morphology and the electrophysiology of the uterus is necessary.
The myometrium, located between the endometrium and perimetrium, mainly consists of uterine smooth muscle cells (see Figure 1.2), also known as uterine myocytes, arranged in overlapping tissue-like bands (the exact arrangement is still a highly debated topic). In addition, this type of smooth muscle can maintain force for prolonged time periods with very little energy expenditure. In regard to smooth muscles, physiologists point out that, important differences exists between various smooth muscle tissues of the same species and between anatomically and functionally comparable smooth muscles of related species (Fischer, 1944). While striated muscles are organs with a comparable locomotive function and consist of only muscle tissue, smooth muscles are generally, only with few exceptions, elements contributing together with other tissues to the anatomy of the whole organ.
The smooth muscle is composed of small fibers, usually 5 to 10 μm in diameter and approximately 20 to 500 μm in length. In most organs, smooth muscle cells are functionally connected by the so called *gap junctions* (functional syncytium, see Figure 1.3). The gap junction is a structure composed of two symmetrical portions of the plasma membrane from two different adjacent cells.
Three types of filaments have been identified in the uterine smooth muscle cells (i) a thick filament consisting of myosin molecules, (ii) a thin filament consisting of actin molecules and (iii) an intermediate filament which consists mainly of desmin molecules (see Figure 1.3).
The actin and myosin filaments possess different striated arrangements compared to skeletal muscles and have a high number of actin filaments which are attached to dense

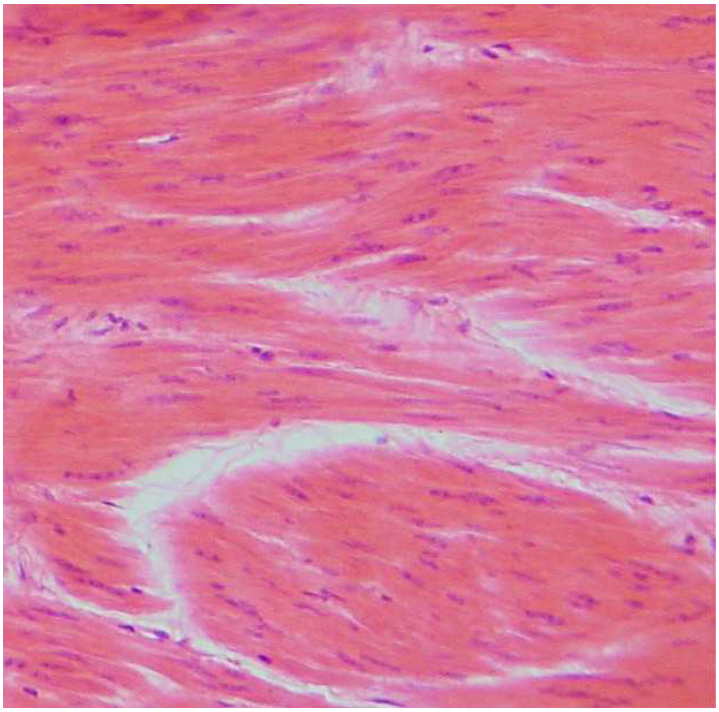

Figure 1.2: Uterine smooth muscle tissue. From `http://commons.wikimedia.org/wiki/File%3AGlatte_Muskelzellen.jpg`. By User:Polarlys (Own work) [GFDL (www.gnu.org/copyleft/fdl.html), CC-BY-SA-3.0 (www.creativecommons.org/licenses/by-sa/3.0/) or CC-BY-2.5 (www.creativecommons.org/licenses/by/2.5)], via Wikimedia Commons.

portions of smooth muscle, known as dense bodies (Chard, 1994). The dense bodies are connected by intermediate filaments, which form an elastic cytoskeleton coupled to the extracellular connective tissue. In addition, the actin and myosin filaments are organized in so called sarcomeres (see Figure 1.3) which are not aligned inside the smooth muscle due to the irregular arrangement of the dense bodies. The amount of actin filaments which are surrounding a myosin filament is variable, but larger compared to those found in the skeletal muscle.

The basic structure of the smooth muscle actin filaments is similar to the structure of actin filaments found in the skeletal or heart muscle. However, the smooth muscle actin filament is considerably longer. Similarly, the smooth muscle myosin filaments are longer compared to their skeletal or heart muscle counterparts and display a rectangular cross-section (Klinke et al., 2009). The myosin molecules are linearly arranged and are characterized by an antiparallel assembly rather than a helical geometry (see Figure 1.3).

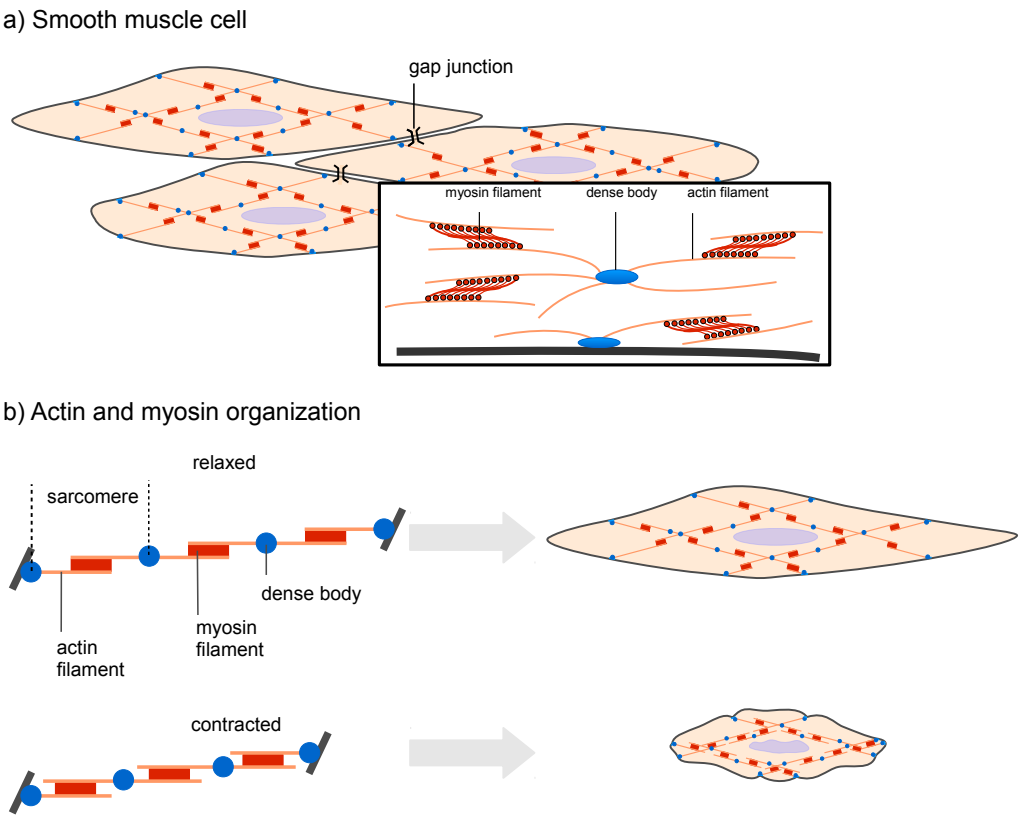

Figure 1.3: Smooth muscle cell organization. a) smooth muscle cells with gap junctions. b) the organization of actin and myosin filaments in sarcomeres. Illustration inspired after (Klinke et al., 2009).

1.1.3 Contractile apparatus of the uterine myometrium

1.1.3.1 Action potential

Cells typically exhibit a voltage potential difference with the inside of the cell being more negative than the outside due to the concentration of potassium (K^+) ions within the cell. In other words, they maintain a voltage difference across the cell's plasma membrane, known as the membrane potential. An excitable patch of membrane has two levels of membrane potential (i) the resting potential, which is the value the membrane potential maintains as long as nothing perturbs the cell, and (ii) a higher value called the threshold potential (Wikipedia contributors, 2012).
While most cells remain at a constant potential and do not vary with time, two types

of cells, smooth muscle and neuronal, are electrically active. Early cell experiments indicated that ionic current flow is voltage dependent (Anderson, 1969). The short-lasting event in which the electric membrane potential of a cell rapidly raises and falls is called an action potential (AP).
For a better understanding of the uterine contractile activity, in the following section, a description of the mechanisms eliciting the AP of the individual smooth muscle cell will be provided.
Figure 1.4 illustrates the ideal AP for typical cells (the actual recordings of APs can be distorted compared to the schematic view due to variations in the electrophysiological assessment techniques). In general, a cell's resting potential is approximately -70 mV due to the K leakage currents and remains at that value until a stimulus is applied. When a stimulus of sufficient magnitude (above the threshold of -55 mV) is applied, the membrane voltage depolarizes. Voltage-gated channels then open and cause quick inward currents of natrium (Na^+) and calcium (Ca^{2+}) ions. This rapid inward flow of positive ions is responsible for reversal of the voltage polarity and contributes to the rising phase of the AP. At approximately +40 mV the Na voltage-gated channels close and voltage-gated K channels open causing the falling phase of the process or repolarization. Because of the large K currents leaving the cell, a transient negative shift known both as hyperpolarization or as a refractory period occurs. This mechanism prevents an action potential from travelling back towards the way it came. Once the voltage-gated K channels close, Na and K pumps continue to balance the ion flow until the resting potential is reestablished (Lodish et al., 2007). The same terminology can be used to describe the activation of the uterine cells. A more detailed description is provided in the following sections.

1.1.3.2 Cell activation

The contractile effort of the myocytes is periodic and arises from the propagation of the electrical activity through the muscle cells in the form of action potentials. The APs are a result of ionic current flow into and out of the cell membrane. The exchange of Na^+, K^+, and Ca^{2+} ions across the cell membrane constitute the ionic currents. Their unequal distribution across the cell membrane creates a potential difference. The ions can be pumped across the cell membrane, against the concentration gradient, by energy that is supplied by the breakdown of adenosine triphosphate (ATP) into adenosine diphosphate (ADP). ATP is a multifunctional nucleoside triphosphate, often referred to as the molecular unit of currency of intracellular energy transfer (Knowles, 1980).

Its main role is to transport energy for metabolism within cells. ATP is produced by photophosphorylation and cellular respiration and is used by enzymes and structural proteins in many cellular processes including muscle action (Knowles, 1980).
At rest, the uterine smooth muscle cell has the following ionic distribution (i) the concentration of Na^+ and Ca^{2+} ions is higher outside the cell (compared to inside) and (ii) the concentration of K^+ ions is higher inside the cell (Chard, 1994). This distribution of ions corresponds to the resting membrane potential. The myometrial

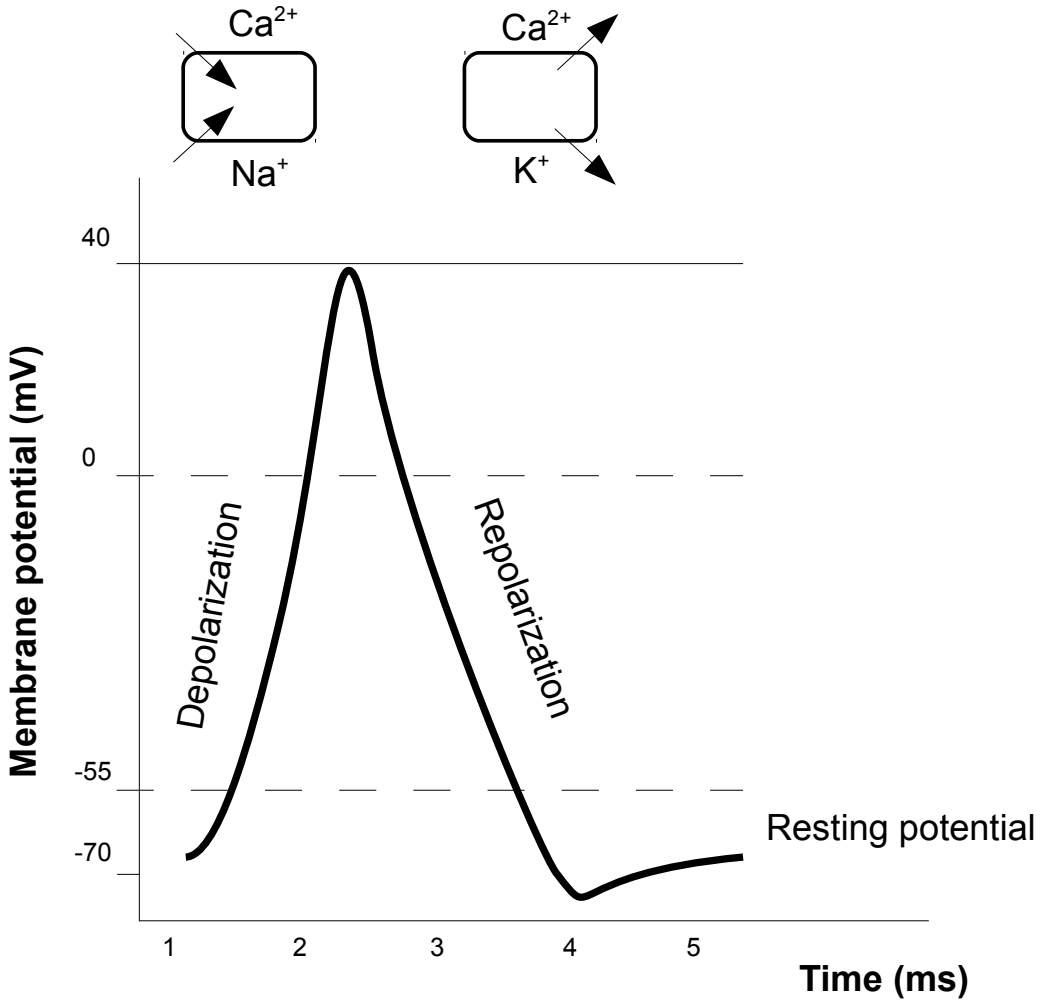

Figure 1.4: Schematic representation of the ideal action potential. Changes of the membrane potential across time (bottom) are shown as a function of the efflux and influx of ions into the smooth muscle cell (top).

cell's resting potential can range from -40 to -60 mV due to the hormonal state (Parkington and Coleman, 2001; Sims et al., 1982). It has been shown that the uterine myometrial cells are electrically coupled by the so-called gap junctions which consist of proteins (Garfield et al., 1995; Maner et al., 2006). When grouped, these proteins create channels of low electrical resistance between cells that facilitate pathways for the efficient conductance of action potentials. There are a few of these channels throughout pregnancy, indicating a poor coupling and decreased electrical conductance. However, as women approach term, the gap junctions increase and form an electrical syncytium which is a prerequisite for proper contractions (Garfield et al., 1995).
The contraction of the myometrium is mainly governed by changes of the Ca^{2+} concentration between extra and intracellular space and by the release of Ca^{2+} from intracellular depots. Specifically, that involves a rise in the intracellular Ca^{2+} concentration from a resting level of about 10^{-7} M to approximately 10^{-5} M.
The source of Ca^{2+} can be (i) intracellular, where Ca^{2+} ions are released from intracellular depots, (ii) extracellular, where Ca^{2+} ions flow into the cell following their electrochemical gradient in response to a change in membrane permeability or (iii) a combination of both (Chard, 1994). Conversely, a reduction of intracellular free Ca^{2+} ions terminates the contraction. The reduction of Ca^{2+} ions occurs either as a result of re-uptake into cellular depots or efflux into the extracellular space (Chard, 1994). However, because the sarcoplasmatic reticulum of the smooth muscle cell is poorly developed, the source of Ca^{2+} causing the contraction is mainly extracellular (Sanborn, 2000). Consequently, diffusion of Ca^{2+} into the cell occurs when the concentration of Ca^{2+} in the extracellular fluid exceeds 10^{-3} M. The average time required for the diffusion is between 200-300 ms (approximately 50 times longer than the diffusion measured in skeletal muscle fibers) (Guyton and Hall, 2010).
Compared to skeletal muscle, smooth muscle cells have many more voltage-gated Ca channels and much fewer voltage-gated Na channels. As a consequence, the generation and propagation of APs in smooth muscle is mainly regulated by Ca channels (in skeletal muscles this activity is mainly regulated by the Na channels) which open and close significantly slower compared to the Na channels. This slow acting mechanism accounts for the slow onset of contraction and relaxation of the smooth muscle tissue in response to the electrical stimulus.
The dynamic of Ca^{2+} concentration is controlled by voltage and receptor controlled channels. This implies that the contraction process of the myometrium can be influenced by changes in the electrical properties and/or the receptor environment. As action potentials propagate over the surface of a myometrial cell, the depolarization

causes voltage-dependent Ca^{2+} channels to open. When this occurs, Ca^{2+} enters the muscle cell traveling down its electro-chemical gradient to activate the myofilaments and elicits a contraction by increasing the size and/or number of actual portals for Ca^{2+} entry (Aguilar et al., 2010). Thus, the increase in Ca^{2+} is considered to be the primary catalyst of the chemomechanical process of smooth muscle contraction.
The repolarization is the result of both the K^+ ion efflux and the inactivation of Na^+ channels. Figure 1.4 shows the relationship between the membrane AP and the inward/outward ion flux in the cell. The inward current carried by Na^+ and Ca^{2+} ions is responsible for the cell polarization and the outward current carried by K^+ and Ca^{2+} ions induces the cell repolarization.

1.1.3.3 Cell coupling

Previous studies have also established that the myometrial electrical activity governs myometrial mechanical contractions (Maner et al., 2006; Tezuka et al., 1995). This behavior was demonstrated in electromyogram (EMG) recordings of the human uterus during pregnancy (Devedeux et al., 1993). Contraction bursts that occur prior to the onset of labor are often perceived by the mothers as periods of perceived contractility. Studies have shown that in various species the gap junctions are sparse throughout pregnancy but increase during delivery (Garfield and Hayashi, 1981; Garfield et al., 1977, 1978; Lodge and Sproat, 1981; Miller et al., 1989; Miyoshi et al., 1998). It was also observed that these gap junctions disappeared within 24 hours of delivery. Gap junction proteins are thought to align themselves and create low-resistant channels (of approximately 1 nm) between the cytoplasm of adjacent cells (see Figure 1.3) to form a pathway for the passage of APs (Garfield et al., 1998, 1977; Miller et al., 1989). The increase in the gap junctions and their electrical transmissions provides better coupling between the cells, resulting in synchronization and coordination of the contractile events of the various myometrial regions in the uterus. The results provide clear evidence that the propagation of the electrical activity over the entire myometrium due to the increase in gap junction areas at term is related to successful progress of labor and delivery of the fetus.
The distribution of gap junctions is not necessarily homogeneous in tissue and the relation between the junction pattern and intercellular communication is poorly understood. The most studied gap junction subunit is the connexin 43 ($Cx43$), a 43-kD protein expressed in myocardium and myometrium as well as in other cells. The results suggest that transcription of the $Cx43$ is induced by activating the proteine kinase

C (PKC) in human myometrial cells (Garfield et al., 1998). The PKC is involved in controlling the function of other proteins through phosphorylation and can be activated by an increased concentration of Ca^{2+} (more details are given in section 1.1.3.4).
Studies conducted by Garfield and colleagues have demonstrated that throughout the pregnancy gap junctions are present at a very low density providing an indicator of poor coupling and limited electrical conductance (Garfield et al., 1977). Conversely, contractile uterine activity during term or pre-term labor is characterized by the presence of a large amount of gap junctions between the myometrial cells (Garfield et al., 1977; Miller et al., 1989). In addition, a study carried out by the same group has shown that the presence of gap junctions is controlled by the regulation of progesterone and estrogen in the uterus. Specifically, progesterone down-regulates and estrogen up-regulates the myometrial gap junction density (Miller et al., 1989).
As previously described, smooth muscle cell voltage-dependent Ca^{2+} channels open as depolarization occurs, allowing Ca^{2+} ions to enter the muscle. Once voltage-dependent Ca^{2+} channels open, a single action potential can initiate a twitch contraction (quick shortening of the muscle) as shown in Figure 1.3. A twitch contraction does not develop force, instead the repeated discharge of the APs contributes to the increase in amplitude of the contraction. In other words, the increments in tension (which are triggered by individual APs) will accumulate as a result of the intracellular free Ca^{2+} ions when APs are discharged at a rate higher than 1 Hz (Marshall, 1962).
The contraction of skeletal muscles is initiated by the nervous system: the moto-neuron triggers an action potential which propagates through the neuromuscular junction to the muscle plate, causing the contraction of the muscle fiber (Guyton and Hall, 2010). Interestingly, neuromuscular junctions that are present in the skeletal muscle do not occur in smooth muscle. In the myometrium the mechanism by which an AP is generated is different. It is believed that the AP burst can originate from any uterine cell. The initiating cells are referred to as pacemaker cells and they can shift from one contraction to another (Lodge and Sproat, 1981).
The concept of a pacemaker in the myometrium has been considered and investigated for many years. It has been suggested that the uterus is myogenic in that it contracts in vivo and in vitro without the need for external stimuli and that any myometrial cell is capable of acting either as a pacemaker or pace-follower (Kao, 1959). However, research employing a variety of histological techniques have not yielded clear evidence of the presence of cells with the histological and electrophysiological properties of a functional pacemaker (Gherghiceanu and Popescu, 2005; Hinescu et al., 2006; Hinescu and Popescu, 2005; Suciu et al., 2007). The key issue about the origin of the electrical

impulse, which initiates the myometrial contraction and the regulation of its direction of propagation, remains unclear in both the pregnant or non-pregnant uterus (Aguilar et al., 2010).

1.1.3.4 Contraction of the smooth muscle cell

The molecular basis of the smooth muscle contraction is represented by the cyclic interaction between the myosin head and the actin filament. During contraction the myosin heads tilt and drag the actin filament (over a small distance of approximately 10 nm), while during relaxation the actin filaments are released. Later on, the myosin heads can rebind to another part of the actin filament and slide along further. A schematic representation is given in Figure 1.3. This mechanism is also known as the cross-bridge cycle, during which the hydrolysis of ATP occurs (Word, 1995). The chemical energy released by the ATP-hydrolysis is transformed by the myosin molecule into active muscular strength. Hence, myosin is regarded as the motor protein of the muscle (Klinke et al., 2009).
In addition, cross-bridges also allow the myosin to pull an actin filament in one direction while simultaneously pulling another actin filament in the opposite direction. As a consequence, smooth muscle cells can contract as much as 80% of their length (skeletal muscles can contract less than 30% of their length) (Guyton and Hall, 2010).
The myosin heads are made of heavy and light protein chains. It has been shown that the contraction and relaxation are regulated by phosphorylation (acquisition of a phosphate group) and dephosphorylation (removal of a phosphate group by hydrolysis) of the myosin light protein chain. Phosphorylation of the regulatory light chain of myosin by Ca^{2+}/CaM - dependent myosin light-chain kinase (MLCK) plays an important role in smooth muscle contraction (Word, 1995). In particular, contraction is initiated by a phosphorylation of myosin by which ATP is degraded into ADP (Guyton and Hall, 2010; Word, 1995). Relaxation is characterized by a low concentration of Ca^{2+} ions, inactivation of MLCK and dephosphorylation of the myosin light chain (Guyton and Hall, 2010).
As already described in the previous sections, compared to skeletal muscle cells, smooth muscle cells have a larger amount of voltage-gated Ca channels and fewer voltage-gated Na channels. Therefore, the generation and propagation of APs in smooth muscle is mainly regulated by Ca channels which open and close significantly slower compared to the Na channels. As a result, there is a very short onset time for contraction and relaxation of the smooth muscle in response to the electrical stimulus (Csapo and

Goodall, 1954). This also corresponds to a slow cycling speed of the myosin cross-bridges in smooth muscle, which is 10 to 300 times slower than in the skeletal muscle (Guyton and Hall, 2010).

To summarize, the myometrium is composed of smooth muscle cells. The basic process controlling the uterine contraction is the underlying electrical activity in the form of APs. APs propagate between muscle cells and open ion channels allowing the influx of calcium ions to produce a contraction. APs occur in groups and form a *burst* of activity which in humans can last more than a minute (Garfield et al., 2005) with the burst frequency around 0.1 Hz. The AP frequency within a burst has been reported to range between 0.1 - 10 Hz (Devedeux et al., 1993) but most of the studies focus on the frequency range 0.1 - 3 Hz (Leman et al., 1999; Marque et al., 1986) or 0.3 - 1 Hz (Garfield et al., 2005; Maner et al., 2003; Rabotti et al., 2010a, 2009). The number of bursts in a given time determines the frequency of a uterine contraction. Consequently, the duration of a burst determines the duration of the uterine contraction and the force generated by the whole uterus is determined by the propagation of APs from cell to cell and the amount of muscle mass involved (Garfield, 1984; Marshall, 1962). Each burst stops before the complete relaxation of the uterus (Marshall, 1962). The electrical properties and the excitability of the myometrial cells can be altered by agents that directly stimulate or inhibit uterine contractions.

1.2 Measurement of uterine contractile activity

1.2.1 Clinical assessment

To date, several different prognostic techniques have been developed to measure uterine contractions. The most commonly used clinical approaches are (i) the tocography (TOCO) see Figure 1.5 (Smyth, 1957), (ii) the intrauterine pressure catheter (IUPC), (iii) the use of biomarkers such as fetal fibronectin (fFN), white blood-cell count (WBC), or corticotropin releasing hormone (CRH) and (iv) the Bishop Scoring System.

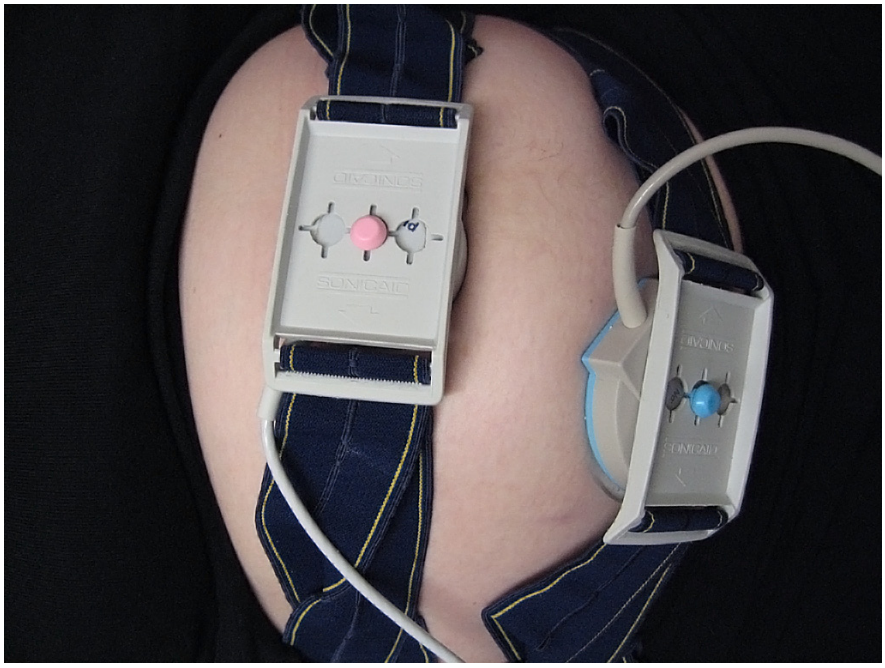

Figure 1.5: Assessment of uterine contractions by tocography. Image freely available from `http://gallery.hd.org`. © Damon Hart-Davis.

The TOCO is the most commonly used non-invasive technique to measure the mechanical deflections produced by the uterine contractions. It is very simple to use and risk free for both, the mother and fetus. The tocodynamometer, a strain-gauge based measurement device, records the deflection of the maternal abdomen during a uterine contraction. The strain on the tensometric transducer, which is strapped on the patient's abdomen, is proportional to the strength of the contraction. The TOCO technique, typically performed in the third trimester of the pregnancy, is widely used by physicians in over 90% of women admitted to labor and delivery units. However, the information obtained is limited, may not detect all uterine contractions and can

not differentiate contractions that will subside spontaneously from those that will lead to delivery. In addition, the frequency of contractions does not reflect the force of the labor (Buhimschi et al., 2003). Another major drawback of this instrument is the susceptibility to maternal motion artifacts. As a consequence of these uncertainties, patients will be either all treated as having preterm contractions or their treatment will be delayed until cervical change occurs (Garfield et al., 1998). In addition, tocodynamometric assessment of uterine contractile activity is very difficult in obese patients.

The IUPC represents a golden standard in the current obstetrical practice as it can provide an accurate assessment of uterine contractions. The IUPC is an invasive method that measures the intrauterine pressure via a catheter (Devedeux et al., 1993). It can be used only after a certain dilatation of the cervix is reached (late stages of pregnancy, close to delivery). A change in pressure inside the uterus is reflected by displacement of the fluid in the catheter.

While the IUPC is more reliable and accurate than TOCO, it is an invasive procedure that requires the rupture of the amniotic membranes, thus limiting its use to patients with complicated delivery. Therefore, the risk that complications might occur when using the IUPC increases significantly. Due to the poor predictive power of the TOCO and the invasive nature of the IUPC, neither technique has been beneficial in the accurate prediction of preterm labor or the diagnosis of true labor at term.

The predictive power of biomarkers was also investigated. The fFN is a fibronectin protein produced by fetal cells, found in the birth canal of pregnant women, between the chorion and the decidua. The use of fFN has been proposed for the prediction of preterm labor and the management of women with symptoms of preterm labor. Some studies reported successful use of fFN in the prediction of actual premature birth (Iams, 2003; Lockwood, 2001), while others suggest that fFN has limited predictive value and conclude that there is no sufficient evidence to recommend its use (Berghella et al., 2008; Garfield et al., 2001; Hellemans et al., 1995; McNamara, 2003).

In a recent study, Hill and colleagues used recursive partitioning to identify gestational age-specific threshold values for infectious and endocrine biomarkers to predict preterm delivery (Hill et al., 2008). They have found that according to gestation age, two biomarkers, namely corticotropin releasing hormone (CRH) and white blood-cell count (WBC), provide a relatively high prediction accuracy for preterm delivery. Although studies of biomarkers have improved the understanding of the mechanisms of disease leading to spontaneous preterm birth, most potential biomarkers (of preterm birth) investigated in women with predisposition to preterm labor are similar with respect

to diagnostic performance and accuracy (Goldenberg et al., 2005). That is, negative predictive values are superior to positive predictive values and the tests are usually more specific than sensitive (Berghella et al., 2008; Hill et al., 2008; McGregor et al., 1995). A high negative predictive value has also been observed for salivary estriol (McGregor et al., 1995).

The Bishop Scoring System is a pre-labor scoring system to assist in predicting whether induction of labor will be required (Bishop, 1964). The total score is achieved by assessing the following five components during vaginal examination: position of the cervix, cervical dilatation, cervical effacement, cervical consistency and fetal station. However, the Bishop score was not found to contribute to a reduction in preterm labor (Garfield and Maner, 2007).

The current state-of-the-art in labor monitoring can be summarized as follows (i) intrauterine pressure catheters provide the best information but with limited usability due to their invasive nature (rupture of the amniotic membranes), (ii) presently available uterine monitors such as TOCO are uncomfortable, less accurate and depend on the examiner for proper placement, and (iii) the predictive power of biomarkers is not sufficient for a successful diagnosis and (iv) the Bishop Scoring System has not lead to a reduction in preterm labor. While cervical change and the frequency of contractions are probably the two most frequently used clinical methods for assessing labor, there is still a high amount of controversy regarding the best way to evaluate and quantify the uterine contractile activity.

1.2.2 Electrophysiological assessment

Two methods are currently employed to record the electrophysiological activity of uterine contractions: (i) the electromyography/electrohysterography (EMG/EHG), recorded by electrodes attached to the abdomen and (ii) a newly established method, the magnetomyography (MMG), based on recordings of the magnetic fields that correspond to electrical fields. These techniques measure the electrical/magnetic activity on the surface of the maternal abdomen, which is a result of a sequence of bursts or groups of action potentials that are generated and propagated in the uterine smooth muscle tissue - the myometrium. The term EHG is more specific, as it strictly refers to the electrical activity of the myometrial cells. However, in the context of uterine activity, the terms EHG and EMG are often used to described the same activity. Therefore, for the sake of simplicity, the term EMG will be used throughout this thesis to refer to the electrical activity of the uterus.

1.2.2.1 Electromyography

The uterine electrical activity, which reflects the original process of muscle fiber excitation due to the propagation of the APs, can be measured by means of internal and abdominal surface electrodes. The EMG recordings of uterine activity date back to 1931 when Otto Bode used a galvanometric device to record the activity of the human uterus during labor for the first time (Bode, 1931). His work unveiled a technique with great potential as it provides a non-invasive and inexpensive assessment of uterine contractile activity. However, decades later, EMG measurements are still not adopted in obstetric practice, despite sustained scientific evidence that the EMG signal is representative of the electrophysiological changes occurring in the myometrium (Buhimschi et al., 1997; Buhimschi and Garfield, 1996; Buhimschi et al., 2003; Garfield et al., 2005; Maner et al., 2003).

Noninvasive EMG recordings have been extensively studied with an emphasis on both time (Buhimschi et al., 1998; Duchene et al., 1990; Verdenik et al., 2001) and frequency domain (Doret et al., 2005; Garfield et al., 2005) parameters for the prediction of labor. Garfield and colleagues performed simultaneous recording of the EMG activity directly from the uterus and the abdominal surface of rats (Buhimschi and Garfield, 1996). They were able to conclusively show that the signals recorded from the abdominal surface correspond to those generated in the uterus, suggesting that similar techniques can be used in humans. The recording of EMG activity on the human uterus using abdominal electrodes was also reported (Garfield et al., 1998).

Other studies have shown that the power density of uterine EMG bursts in patients during active labor peaked at 0.71 ± 0.05 Hz as compared to non-laboring term (0.48 ± 0.03 Hz) patients (Garfield et al., 2005, 1998; Maner et al., 2006). In addition, the power density peak values were comparatively low for non-labor patients with respect to patients in active labor. The EMG has a high temporal resolution. However, because of the differences in the conductivities of tissue layers, the EMG signals are often filtered during their propagation to the surface of the abdomen.

1.2.2.2 Magnetomyography

All electrophysiological phenomena that occurs inside the human body are characterized by the flow of ion currents which can be detected by a measurement of potentials inside or on the surface of the human body (Baumgartner, 1995; Preissl, 2005; Rogalla and Barker, 1991). While the EMG technique allows successful assessment of uterine contractions, another method of observing biomagnetic signals is magnetomyography (MMG). MMG, the magnetic counterpart of the EMG, is a noninvasive technique that measures the magnetic fields associated with APs (see Figure 1.6).

MMG measurements are conducted externally, using sensitive magnetic sensors called superconducting quantum interference devices (SQUID). A SQUID is a very low noise magnetic field sensor, which converts the magnetic flux threading a pickup coil into voltage allowing the detection of weak magnetic signals. Since the SQUIDs rely on the physical phenomena found in superconductors they require cryogenic temperatures for proper operation. Therefore, the array of SQUIDs is immersed and cooled in liquid helium (at approx. -270° C), in a special vessel called a dewar.

The MMG recordings possess some important properties which renders them suitable for the analysis and characterization of the human biomagnetic activity. Compared to EMG signals, the MMG signals are detectable outside the boundary of the skin without making any contact with the body. Also they are independent of conductivity geometry, i.e. tissue conductivity. The measured electrical activity arises from the volume currents flowing (in the body) to the electrode sites and not directly due to the primary current generators. Therefore, the uterine EMG signals suffer from some degree of attenuation by the time they reach the surface of the maternal abdomen. By contrast, magnetic field recordings are more strongly coupled to the primary currents and are much less dependent on tissue conductivity boundaries. Thus, compared to the electric field, the magnetic field observed outside the human body offers a much more precise representation of the underlying activity.

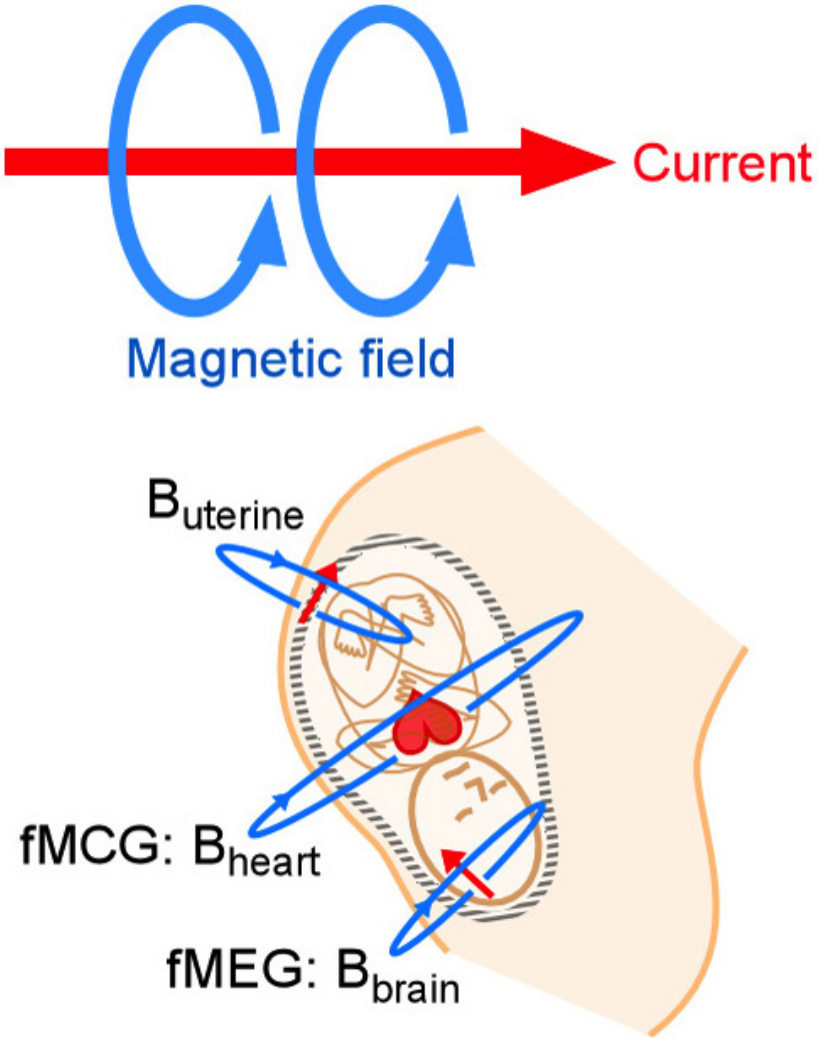

Figure 1.6: Magnetic field generation. Magnetic fields are generated by different biological processes such as fetal magnetocardiogram, fetal magnetoencephalogram, uterine contraction, maternal magnetocardiogram or bladder contraction. The image is courtesy of UAMS, Sara Research Center.

During a MMG recording detection of the signal is made outside the boundaries of the skin, that is, without any electrical contact with the body. Further, the MMG recordings provide a higher spatio-temporal resolution compared to EMG, as the spatio-temporal resolution obtained from the abdominal surface electrode recordings is limited based on the electrical properties of the abdomen and the practical difficulties of placing

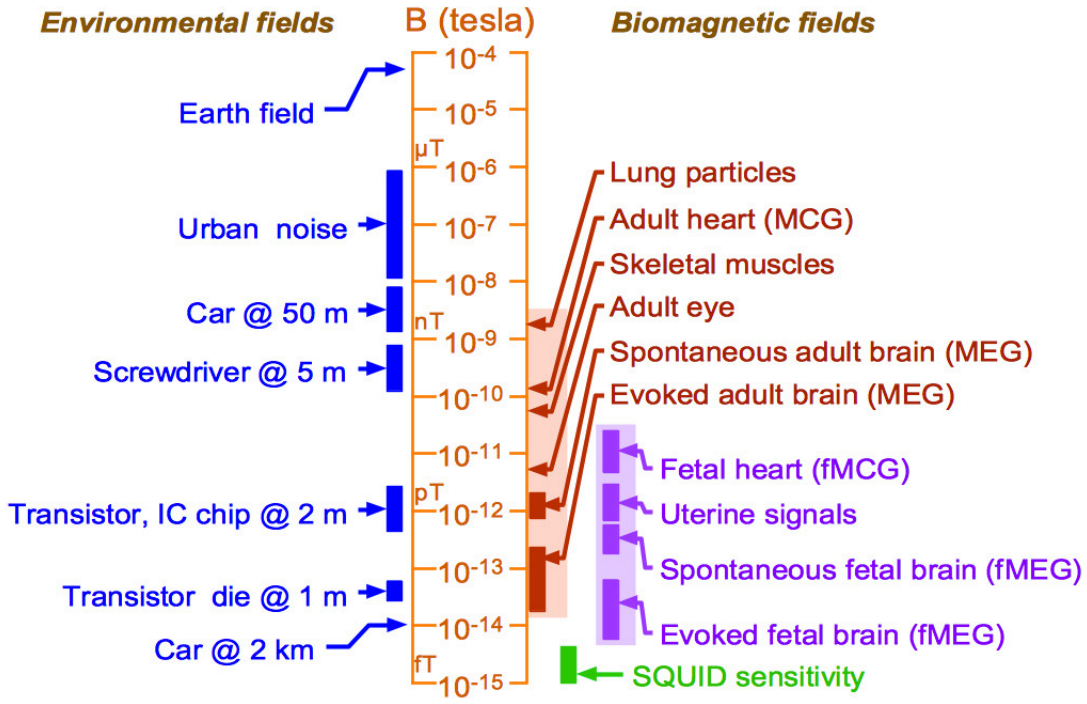

Figure 1.7: The strength of magnetic fields. Image kindly provided by J. Vrba, Vancouver.

numerous electrodes on the mother (Eswaran et al., 2009). In addition, the MMG recordings are independent of any kind of references, which ensure that each sensor mainly records localized sources.

MMG measurements span a frequency range from about 10 mHz to 1 kHz and field magnitudes from about 10 fT for spinal cord signals to about several pT for brain rhythms.

Figure 1.7 illustrates a few examples of magnetic field strength to provide the reader information regarding the magnitude of the MMG signals. It should be noted that the Earth field magnitude is about 0.5 mT and the urban magnetic noise about 1 nT to 1 T. This corresponds to a factor of 1 million to 1 billion larger than the MMG signals. Such large differences between signal and noise requires a very high accuracy of noise cancellation. Therefore, the system must be placed in a magnetically shielded room, to avoid the interference of the strong environmental noise and external magnetic fields with the biomagnetic fields generated by human organs.

First MMG recordings of spontaneous uterine activity were reported by Eswaran

and colleagues, demonstrating the feasibility of the technique (Eswaran et al., 2002). The measurements were carried out with a system called SARA (SQUID array for reproductive assessment), CTF Systems Inc. Port Coquitlam Canada (see Figure 1.8). The system consists in primary superconductive quantum interference device (SQUID) magnetic sensors that are spaced approximately 3 *cm* apart in a concave array that covers the maternal abdomen from the pubic symphysis to the uterine fundus and laterally over a similar span. The surface of the array is curved to match the shape of

Figure 1.8: The SARA I system. Left: General view of the system. Right: the concave array of sensors. The image is courtesy of UAMS, Sara Research Center, Little Rock, USA and CTF Corporation, Canada.

the gravid abdomen. To allow SQUIDs to record the MMG signals, the mother must simply lean forward against the smooth surface of the array. Thus the SARA system is capable of obtaining electrophysiological data from the entire fetus and maternal reproductive system in a passive, consistent and non-invasive manner.
Because strong environmental noise and external magnetic fields can interfere with the human biomagnetic fields, SARA was installed in a magnetically shielded room (Vakuumschmelze; Hanau, Germany).
There are currently two such systems installed worldwide. The first SARA system, called SARA I, is operational since May 2000 at the University of Arkansas for Medical Sciences (UAMS), at the SARA Research Center, Little Rock, USA. As of September 2008 a second SARA system, called SARA II, is in operation at the University of

Tübingen, fMEG Center, Tübingen, Germany. Compared to the system installed at the UAMS, SARA II provides a slightly better coverage of the perineal region, consequently covering a slightly larger surface of the gravid abdomen. For an overview of the organization and labeling of the magnetic sensors in both systems refer to the Appendix, Figure A.1.

1.3 Automatic detection of uterine contractile activity

The automatic detection of uterine contractions has been attempted by different studies. Radhakhrishnan and colleagues attempted to detect uterine contractions in EMG using higher-order zero-crossing analysis (Radhakrishnan et al., 2000).

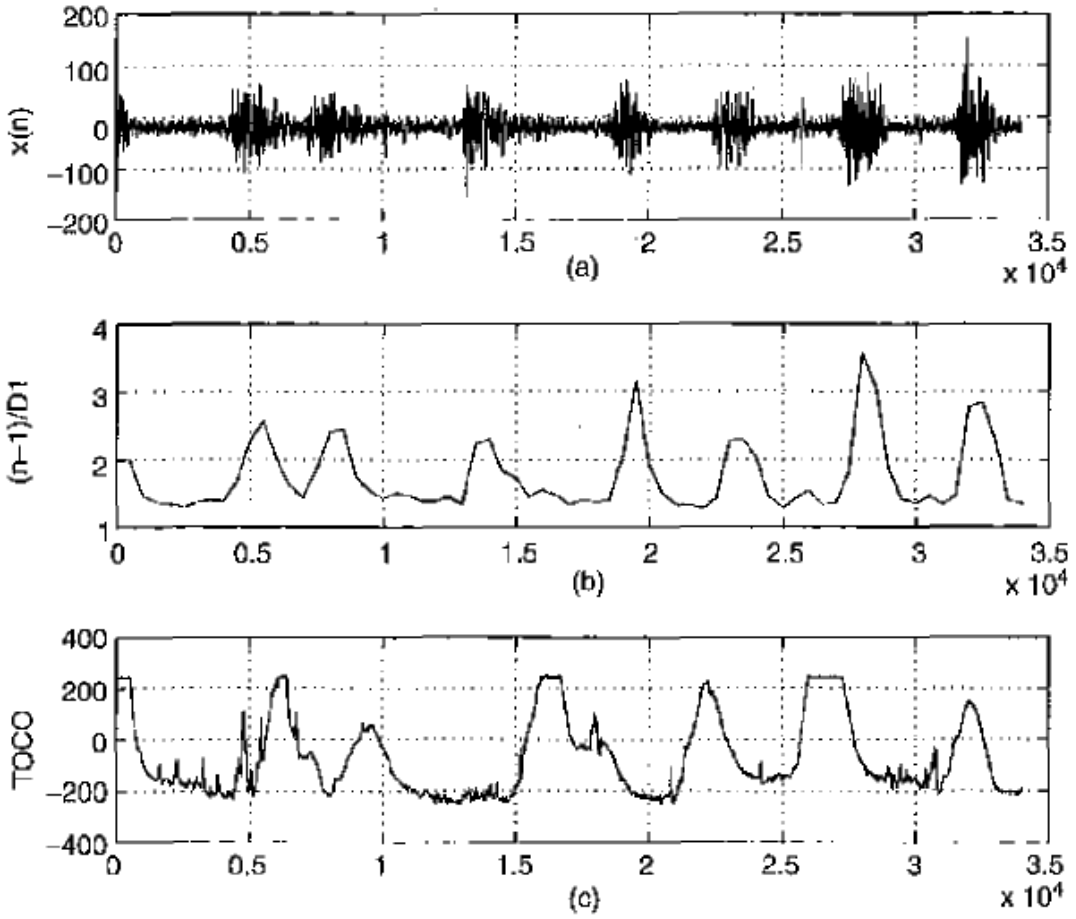

Figure 1.9: Application of the zero-crossing method. (a) EMG data of a subject in the 38^{th} week of gestation. (b) The peaks of the first-order normalized zero-crossing counts. (c) The TOCO recording of the subject. Image from (Radhakrishnan et al., 2000), © 2000 IEEE.

In addition to EMG measurements the authors performed TOCO and IUPC recordings on the investigated datasets to compare the outcomes of their proposed method. They have observed that the discriminating power of the higher-order crossing counts $D(i)$ decreased as the order i increased ($i > 2$).
The method was applied to a subject, in non active labor, in the 38^{th} week of gestation,

see Figure 1.9. In (a) the processed uterine EMG is presented. In (b) the peaks of the normalized first-order zero-crossing (FOZC) counts coincide with the segments where contraction occurs. Figure 1.9 (c) presets the TOCO recording from the same subject. The authors discuss the feasibility of this technique and conclude that (i) the first-order zero crossing method is the most suitable to discriminate between contractile and non-contractile events and (ii) the results are consistent with the TOCO and IUPC recordings. However, the method lacks threshold detection and does not take into account the frequency characteristics of the signal.

Based on the assumption that the uterus remains quiescent throughout most of the pregnancy but close to the time of delivery its electrical activity increases, a generalized synchronization index, as an indicator to track the spatial patterns of uterine myometrial activity, was proposed by Ramon and colleagues in (Ramon et al., 2005). The synchronization of a sensor pair was inferred from a statistical tendency to maintain a constant phase difference over a given period of time (one should note that during that same time frame the analytic phase of each sensor may change markedly).

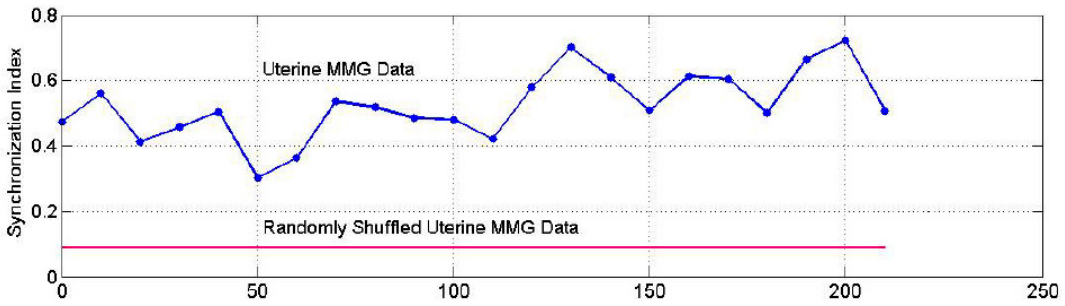

Figure 1.10: Synchronization index. Figure from (Ramon et al., 2005). Permission to reuse granted according to the terms of the BioMed Central Open Access license agreement. `http://www.biomedcentral.com/about/license`.

The phase differences between two sensors were computed by subtracting the cumulative linear phase (the unwrapped phase of the analytic signal) of one sensor from the other. Synchronization between the phases of two signals was computed using Shanon's Entropy Function (Shannon and Weaver, 1998).

$$e(t) = -\sum_{i=1}^{N} p_i \ln p_i \tag{1.1}$$

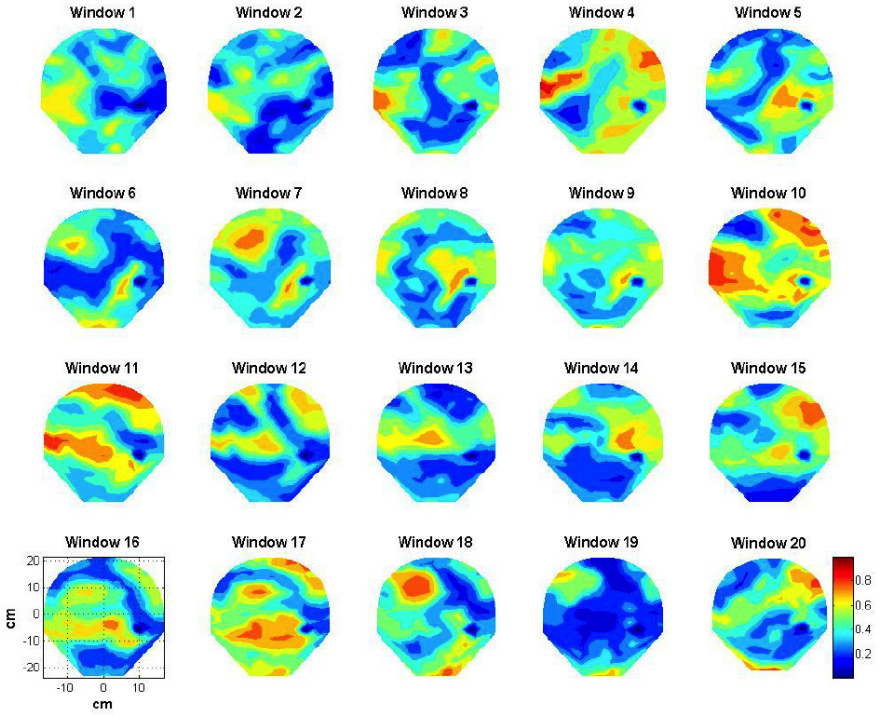

Figure 1.11: Spatial patterns of the synchronization indices across the inspected windows. The synchronization indices are computed within 20 sec stepping windows. Figure from (Ramon et al., 2005). Permission to reuse granted according to the terms of BioMed Central Open Access license agreement. `http://www.biomedcentral.com/about/license`.

where p_i is the relative frequency of finding the phase difference modulus of 2π in the i^{th} bin (N represents the number of bins). To compute the phase difference in a 20 s stepping window, a total of $N = 100$ bins were used. Because $e(t)$ can vary between zero and $e_{max} = ln(N)$, further normalization was necessary which yielded the generalized synchronization index (see Figure 1.10).

$$q(t) = \frac{e_{max} - e(t)}{e_{max}} \tag{1.2}$$

The authors computed the generalized synchronization index in regional coil-pairs for six pregnant women with a gestational age (GA) ranging from 29 to 40 weeks. For any given coil, the coil-pair consisted of the surrounding six coils. This resulted in 21 unique combinations of coil pairs and synchronization indices.
The index was computed for a 4 minute segment (which included at least two contractions) and at points when the subjects reported perceivable contractions. For a

comparative analysis, the magnetic field data was randomly shuffled in each channel and followed by the computation of the synchronization indices. The authors show that the synchronization indices of the unshuffled (original) data are much higher compared to the synchronization indices of the randomly shuffled data (red horizontal line in Figure 1.10) and conclude that the synchronization indices (see Figure 1.10) and their spatial distributions describe uterine contractions. Figure 1.11 shows the spatial patterns of the synchronization indices across the inspected windows and computed within a 20 s stepping window. The intensity scale is normalized in the range of zero (blue) to one (red), with red areas indicating higher synchronization.

In a recent study La Rosa and colleagues used a multiple change-point estimator along with the K-means clustering algorithm to detect uterine contractions in selected regions (see Figure 1.12) of a SQUID sensor array (La Rosa et al., 2008). The channels were modeled by a time varying auto regressive (AR) model. A segmentation algorithm based on the Schwarz Information Criterion (SIC) was used to estimate the time-instants of changes in the parameters. To discriminate contractions, features such as the time segment power, i.e., root mean square (RMS), and the dominant frequency component, i.e., first-order zero-crossing (FOZC), were evaluated. A discrete-time binary decision signal, indicating the presence of a contraction, was created by applying an unsupervised clustering algorithm to classify the RMS values. The detection of multiple change points was performed using a binary search algorithm. Figure 1.13 (a) illustrates a down sampled and filtered (0.2 - 0.4 Hz) MMG signal with vertical grid lines indicating the estimated change points. In Figure 1.13, (b) and (c) show the RMS and FOZC computed on the estimated time segments. It can be observed that the FOZC poorly estimates the presence of a contraction in the investigated frequency range. Figure 1.13 (d) presents the clusters obtained after applying the K-means algorithm on the RMS values. Figure 1.13 (e) shows the binary decision signal and in (f) the time-intervals are illustrated where the mother reported the presence of a contraction.
However, in practice, the approach performed well only for a group of channels from the same patient, suggesting that a different model for segmentation should be attempted. Moreover, this approach does not take into account information from all of the sensors. In addition, the K-means clustering technique needs *a-priori* specification of the number of clusters in the data. The authors use three cluster centroids to discriminate the contractions from noise. From the very nature of this setting, this approach will always erringly identify some segments as contractions even though they may not be present

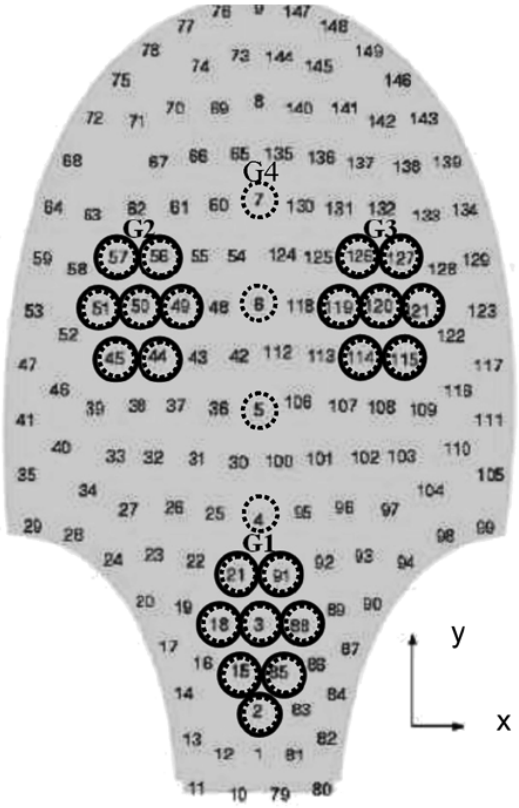

Figure 1.12: Sensor array with selected regions. Complete circles indicate the group of channels G1, G2, G3 and the dotted lines indicate the group of channels G4. Figure from (La Rosa et al., 2008), © 2008 IEEE.

in the data. On the other hand, if the dataset contains a long single contraction, by construction, their approach will label some parts of the uterine contraction as noise. Finally, since the frequency content of the electrical burst activity corresponding to the uterine contractions changes with time (Garfield et al., 2005), a simple spectral analysis (RMS for this particular case) may not be sufficient to objectively capture the uterine contractile activity.

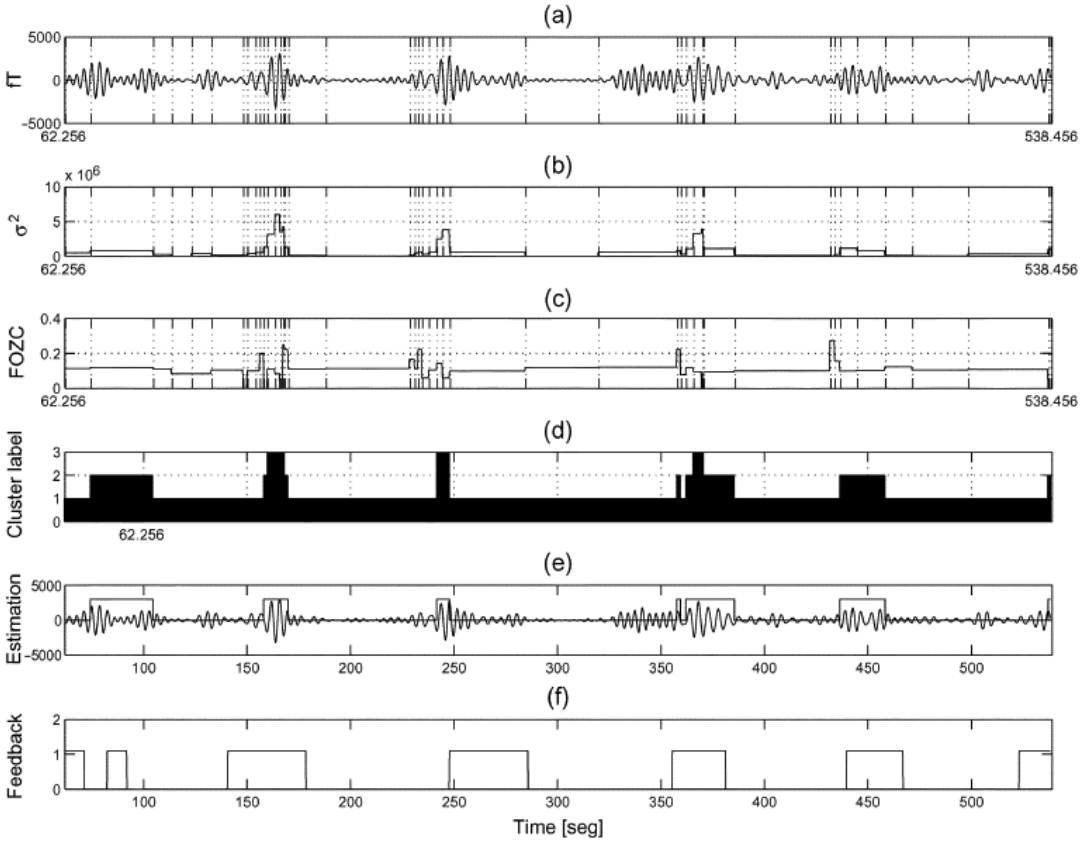

Figure 1.13: Steps in obtaining the discrete-time binary decision signal. (a) Preprocessed channel with grid lines indicating the estimated change points, (b) RMS in each time segment, (c) first-order zero-crossing in each time segment, (d) cluster groups using RMS features, (e) estimated contractions segments, (f) time segments with contractions according to the patient feedback. Figure from (La Rosa et al., 2008), © 2008 IEEE.

2

Aim of the work

The present work is mainly motivated by the need for noninvasive tools in the assessment of uterine contractions and in the accurate prediction of labor. This need is raised, one one hand, due to a compromise between accuracy and invasiveness - a compromise which is still present in the monitoring methods currently used in clinical practice. On the other hand, there is a lack of methods available for MMG which can provide a better understanding of the process leading to labor. Knowledge about the nature of contractions will ultimately allow a timely treatment of premature labor.

Based on the underlying physiological processes described in the previous chapter, the current work introduces a set of signal processing methods, developed with the purpose to improve the interpretation of current MMG measurements for the perspective of clinical applications. Though the techniques developed here are demonstrated on MMG signals, they can be easily applied to multisensor EMG signals as well.

The main goal of the thesis is to develop a new method for the analysis of MMG signals which allows the uterine contraction monitoring and preterm delivery prediction during pregnancy.

A major part of the thesis is dedicated to the detection and identification of the uterine contractile activity measured using a magnetic sensor array. A novel multi-stage method is introduced which takes into account the signal's properties from different frequency bands.

Another important objective of the thesis is to characterize the dynamics of the contractile activity to provide a timely prediction of delivery. In particular, a multi-sensor analysis of the spatial propagation properties of the MMG signals is carried out. This type of analysis is of particular relevance because the spreading of magnetic activity in the myometrium results in coordinated way in order to develop sufficient

force to expel the fetus. Therefore, the analysis of the spatial propagation properties, i.e., conduction velocity, could provide a fundamental contribution to the prediction of delivery.

2.1 Methods developed for the dissertation

The goal of this dissertation was to develop a set of methods that would allow the automatic detection of uterine contractile activity and the computation of the conduction velocity (CV) of the propagating MMG signals. The methods were evaluated both on synthetic data and on serial MMG recordings collected from healthy pregnant women.

2.1.1 Automatic detection of uterine contraction bursts

To date there is no accurate and objective method available for MMG to automatically detect the uterine contraction bursts or to predict the onset of the labor. Currently available methods for the detection of uterine contractile activity in MMG recordings do not take into account the variations of the frequency content of the electrical burst activity with time. It has been shown that the power density of uterine bursts in subjects during active labor peaked at $0.71 \pm 0.05\ Hz$ as compared to non-laboring term patients $0.48 \pm 0.03\ Hz$ suggesting a shift in the power of the signal from lower-frequency to higher-frequency (Garfield et al., 2005, 1998; Maner et al., 2006). A time-frequency analysis could be employed to identify the burst locations. However, such an analysis would be sensitive to the amplitude modulation of the signal hindering the reliable and objective detection of bursts with low amplitude. Hence a simple spectral analysis may not be adequate to capture the uterine contractile activity. To overcome this inconvenience the current work introduces a new multi-stage approach for the automatic detection of uterine contractile activity, which is based on the combination of Hilbert-wavelet transforms and model based threshold fitting. By design, the method will always take into account information coming from the frequency band with the highest power. Expressed differently, it keeps track of the shift in the power of the signal (from lower to higher frequency bands) with the progression of gestation. Therefore, it is expected that the proposed approach will provide a more accurate estimate of the contractile events compared to current approaches. A schematic representation of the developed method is shown in Figure 2.1. The green area highlights the steps representing the own contribution to the development of the method.

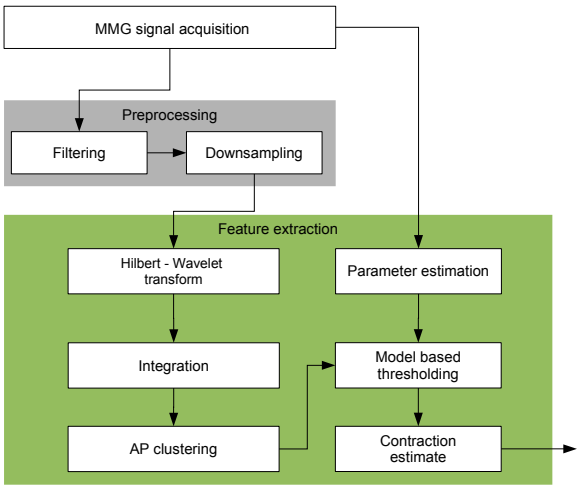

Figure 2.1: Methodology for the detection of uterine contractions. The detection algorithm is applied to multi-sensor MMG signals. The green area highlights the steps representing the own contribution to the development of the method.

Multi-sensor MMG signals will be recorded with the SARA system. The acquired signals will be preprocessed according to section 3.4, downsampled, partitioned in 30 s disjoint inspection windows and analyzed in the time-frequency domain using the second order Daubechies discrete wavelet *db2*. The variance of the wavelet coefficients will be computed as an equivalent to the spectral power and can be used to characterize the underlying dynamics. However, as higher decomposition levels are reached, fewer coefficients will be available and as a consequence the spectral power cannot be reliably computed. To overcome this impediment, the signal will be reconstructed using the wavelet coefficients (at each level of decomposition) and to quantify the power in each frequency band the Hilbert transform of the reconstructed signals will be computed. The MMG power will be clustered into different components by using the affinity propagation (AP) clustering technique. The aim is to identify and discard the noise components. The definition of noise level is however ill defined in the MMG data. Therefore, another novelty introduced in the current work is a model based thresholding. The outcomes of the AP together with the threshold derived from the proposed model will be used to delineate contractile bursts from the background activity. Based on this information, a single discrete-time binary decision signal or *contraction marker* will be created to indicate the presence or absence of a contraction during a MMG recording.

2.1.2 Conduction velocity of the uterine contraction

The spreading of the coordinated electrical activity (and the resulting magnetic activity) in the myometrium is a prerequisite for effective contractions (Garfield et al., 1988). The CV of the propagating MMG signal could provide a fundamental contribution for the prediction of delivery. The fourth chapter of this thesis introduces, for the first time, a method to compute the CV in MMG signals. Because the computation of CV needs information from the level of individual sensors, the approach presented in the previous section will be extended to encompass all magnetic sensors. That is, for each sensor a contraction marker will be computed using the power information from the respective sensor. By creating a marker for every sensor, it is likely that the contraction detection method becomes more susceptible to artifacts introduced by movement of the subject. To overcome this inconvenience, the current work introduces an artifact detection method, which relies on the analysis of the maternal magnetocardiogram (mMCG) signal. Figure 2.2 presents the methodology of the movement artifact identification.

In a next step, the detection of the uterine contractile activity will be performed

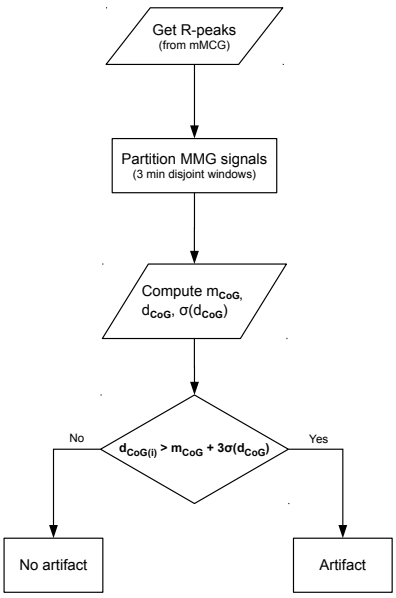

Figure 2.2: Schematic representation of the movement detection algorithm.

in each sensor within a 30 s sliding non-overlapping window. Samples labeled as movement artifact will be discarded from further analysis. The sensor space will be subdivided (according to the 2D coordinates of the sensors) into four quadrants (Q) or regions. Such partitioning would also allow to investigate the interaction between different regions of the uterus. To compute the delay (i) pairwise combinations of quadrants will be investigated (e.g., Q1-2, Q1-3, etc.), (ii) the inspection windows wherein contractile activity simultaneously occurs in any given quadrant pair will be further analyzed (the algorithm will perform further operations only if the number of active sensors (NAS), that is, the amount of sensors wherein contractions were detected, exceeds the preset value of ten sensors) and (iii) the delay between the center of gravities (CoG), that correspond to different quadrants in a pair, will be computed using the high dimension cross-correlation function (HDCC) described by (Smilde et al., 2009). Figure 2.3 presents the schematic representation for the computation of CV.
Once the delay is assessed the CV can be easily computed by dividing the euclidean distance between CoGs that belong to different quadrants in a pair, and the amount of time by which they are delayed. The performance of HDCC will be assessed and validated by means of event based simulation, wherein a stochastic model (based on a second order autoregressive process) is evaluated. Finally, the relationship between the gestational age and the CV computed in serial MMG recordings will be investigated by means of statistical analysis.

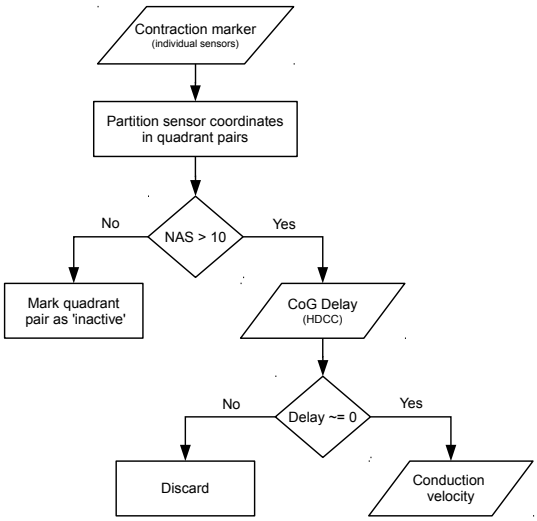

Figure 2.3: Methodology for the computation of the conduction velocity.

3

Uterine contraction identification by global power

This chapter provides a description of the method which was developed to automatically identify and mark the uterine contractile activity. Identification is performed using the information collected from MMG multi-sensor data. The first two sections provide the basic theory of the Hilbert and wavelet transform and highlight some of their important properties. Important details regarding the Hilbert transform of the wavelet decomposition (HTWD) are given in section three. According to this new approach uterine contraction bursts can be successfully identified in MMG signals. The combination of HTWD introduced in this chapter was published in (Furdea et al., 2009).

3.1 Introduction

In early gestation the uterine myometrial activity is infrequent and is characterized by low amplitude values. The quiescence of the uterus during the early gestational age is due to the poor electrical coupling among the smooth muscle cells. As subjects approach term, the increase in the number of gap junctions (see section 1.1) leads to the formation of an electrical syncytium - a prerequisite for proper contractions (Garfield et al., 1995).
Low resistance electrical paths are formed which allow the propagation of electrical activity from cell to cell in the form of an action potential (AP) (Buhimschi and Garfield, 1996; Garfield and Hayashi, 1981). Thus, the uterine contractile activity results from the excitation and propagation of the electrical activity in form of APs which occur in groups and is referred to as *burst*. As subjects approach term and especially during labor, the bursts become more frequent with higher amplitude values. It has been shown that the changes of the electrophysiological properties of the uterine smooth muscle tissue also correlate with the increase of the intrauterine pressure (IUP) (Garfield and Maner, 2007).
The frequency content of the electrical burst activity corresponding to the uterine contractions changes with time (Garfield et al., 2005). A time-frequency analysis could be employed to identify the burst locations. However, such an analysis would be sensitive to the amplitude modulation of the signal. As a consequence, a reliable and objective detection of bursts with low amplitude can not be performed. Hence a simple spectral analysis may not be adequate to capture the uterine contractile activity. In the present chapter, a combination of Hilbert-wavelet transforms (time frequency analysis) and affinity propagation clustering (APC) algorithm (Frey and Dueck, 2007) followed by threshold fitting are introduced with the aim to identify the uterine contractions. While wavelet transform decomposes the MMG signals into different frequency bands, the Hilbert transform quantifies the power in each frequency band. After this step, the APC technique and threshold fitting are applied on the Hilbert amplitude to create a discrete-time binary decision signal that would indicate the presence of a contraction. For the sake of simplicity, the discrete-time binary decision signal will be further referred to as *marker*.

3.2 Hilbert transform

The Hilbert transform represents the only singular operator in one dimension rendering it one of the the most important linear operators in harmonic analysis. The Hilbert transform has a profound impact on several theoretical and physical problems across a wide range of disciplines (e.g. theory of modulation, problems in Fourier convergence, complex analysis, etc.). In signal processing the Hilbert transform (HT) is a linear operator which takes a given signal $x(t)$ and produces a function $h(t)$ within the same domain, simultaneously providing the analytic representation of $x(t)$. The HT has become a basic tool in Fourier analysis, offering a concrete means for realizing the conjugate of a given series. For a signal $x(t)$, the HT $h(t)$ is defined by the following

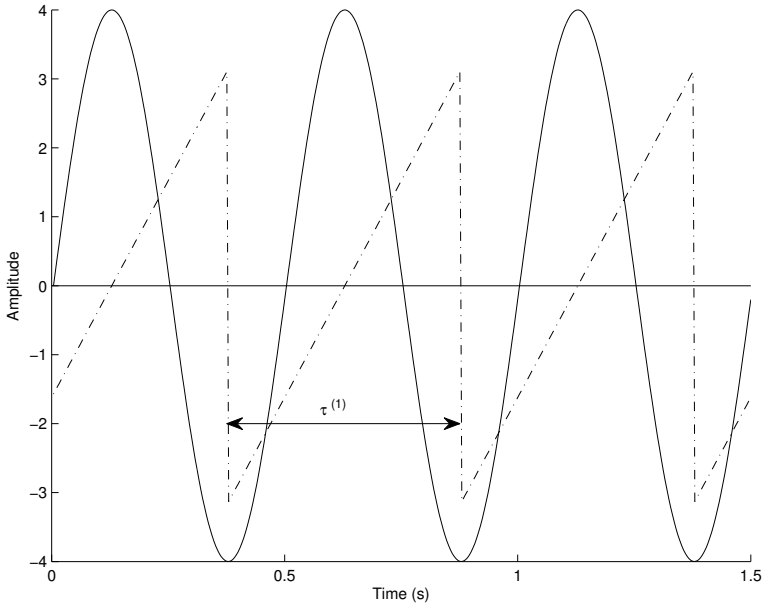

Figure 3.1: An example of phase slip - A sine wave with a periodicity of 0.5 sampled at 250Hz was used. The dashed line indicates the result of phase slip at $-\pi/2$. $\tau^{(1)}$ corresponds to the periodicity of the sine wave and represents the difference between consecutive phase slips.

convolution integral:

$$h(t) = \frac{1}{\pi} PV \int_{-\infty}^{\infty} \frac{x(\tau)}{(t-\tau)} d\tau \tag{3.1}$$

where PV denotes Cauchy's principal value (Pandey, 1996). The representation as a complex analytical signal for $x(t)$ together with its HT $h(t)$ is given by:

$$f(t) = x(t) + i \cdot h(t) \tag{3.2}$$

where $i = \sqrt{-1}$, $t = n/SF$, n is the sample number and SF is the sampling frequency of the signal in Hz. The Hilbert transform of a signal with non-zero mean has zero mean (Mertins, 1999).
Equation 3.2 also allows to define the Hilbert phase (HP) as:

$$\varphi(t) = \tan^{-1}\frac{h(t)}{x(t)} \tag{3.3}$$

and thus, renders possible the study of the instantaneous phase of the signal. When the magnitude of successive phase differences

$$|\varphi(t_{i+1}) - \varphi(t_i)| \tag{3.4}$$

exceeds π the HP exhibits slips, as presented in Figure 3.1.

3.3 Wavelet transform

A signal can be expressed as the sum (possibly infinite) of a series of simple oscillating functions (sines and cosines), also known as a Fourier expansion. The Fourier transform characterizes the global frequency content of the signal and hence the time varying nature of the frequency can not be reliably studied with this approach.
Wavelets can overcome this impediment in that they are able to represent the signal in the time and frequency domain at the same time. The wavelet analysis procedure is to adopt a wavelet prototype function $\psi(t)$ sometimes called *mother wavelet*, which is confined in a finite interval. Temporal analysis is performed with a contracted, high-frequency version of the mother wavelet, while frequency analysis is performed with a dilated, low-frequency version of the same wavelet, that is, *daughter wavelets* $\psi_{(a,b)}(t)$ are formed by translation b and contraction a. The pair (a, b) defines a point in the right half plane $\mathbb{R}_+ \times \mathbb{R}$. An individual wavelet can be defined as follows:

$$\psi_{(a,b)}(t) = |a|^{-1/2}\psi\Big(\frac{t-b}{a}\Big) \tag{3.5}$$

The projection of a function x on the subspace of scale a can be represented as:

$$x_a(t) = \int_{\mathbb{R}} WT_\psi\big\{x\big\}(a,b) \cdot \psi_{(a,b)}(t)db \tag{3.6}$$

where ψ has a zero integral. The continuous wavelet transform of the finite energy function of x is the family of coefficients WT defined by:

$$WT_{\psi}\{x\}(a,b) = \langle x, \psi_{a,b} \rangle = \int_{\mathbb{R}} x(t)\overline{\psi_{a,b}(t)}\, dt \tag{3.7}$$

with $a \in \mathbb{R}_+$ and $b \in \mathbb{R}$ (Misiti et al., 2007).
To obtain the discrete wavelet transform, instead of the family of wavelets introduced in 3.5 one can use the family of wavelets indexed by $\mathbb{Z}$:

$$\psi_{(p,n)}(t) = a_0^{-p/2}\psi(a_0^{-p_t} - nb_0) \tag{3.8}$$

with $a_0 > 1$, $b_0 > 0$ fixed and $p, n \in \mathbb{Z}$. The discrete wavelet transform of the function x can be defined by:

$$WT_{\psi}\{x\}(p,n) = \langle x, \psi_{p,n} \rangle = \int_{\mathbb{R}} x(t)\overline{\psi_{p,n}(t)}\, dt \tag{3.9}$$

with $p, n \in \mathbb{Z}$ (Misiti et al., 2007).
Because the original signal or function can be represented in terms of a wavelet expansion (using coefficients in a linear combination of the wavelet functions), data operations can be performed using just the corresponding wavelet coefficients. In addition if the wavelet coefficients are truncated below a certain threshold, a sparse representation of the data can be obtained.

3.4 Global power based contractile activity identification

The duration of a uterine contraction varies between 40 and 60 s (Devedeux et al., 1993; Maner and Garfield, 2007) with MMG activity typically preceding the contraction. Based on the results reported in earlier studies (Garfield et al., 2005, 1998; Maner et al., 2006) the focus was set on the following two frequency bands (i) low frequency 0.1 - 0.4 Hz and high frequency 0.4 - 1 Hz. In order to obtain these two frequency bands via wavelet analysis, the signals were down sampled to 32 Hz. The downsampling operation significantly reduces the computational time required by the subsequent analysis and is performed without aliasing due to the high rate at which MMG signals are sampled (usually over 1 kHz).

To effectively capture the low frequency activity, it is essential to remove artifacts such as maternal/fetal magnetocardiography (mMCG, fMCG) and maternal breathing. For this purpose, the data is band pass filtered between 0.1 - 1 Hz to eliminate the mMCG/fMCG and further notch filtered between 0.25 - 0.35 Hz to suppress the prominent signal induced by the maternal breathing. For all filtering purposes a fourth order Butterworth filter with zero phase distortion is used.

The preprocessed signals are partitioned in 30 s disjoint inspection windows and a small portion at the end of the signal which is not integer multiple of the inspection window is discarded from the analysis. Data $x_i(t)$ from the i^{th} sensor are convoluted with second order Daubechies discrete wavelet *db2* to produce approximate and detail coefficients as follows:

$$W_x(u, 2^j) = \sum_{t=0}^{N-1} x(t)\psi^*_{j,u}(t) \tag{3.10}$$

where $W_x(u, 2^j)$ contains the wavelet coefficients (approximate $c_j(u)$ and detail $d_j(u)$) at time u at scale 2^j in j^{th} level of decomposition. Detail coefficients $d_j(u)$ can also be independently computed as follows:

$$d_j(u) = \int \phi_{j+1,u}(t)x(t)dt \tag{3.11}$$

where $\psi(t)$ and $\phi(t)$ represent the mother and father wavelet, respectively and $\psi(t)$ is represented as the linear combination of $\phi(t)$.

In broad sense, the approximate coefficients correspond to the low-pass coefficients and capture the trend in the data whereas the detail coefficients correspond to the high-pass coefficients and keep track of the fluctuations in the data. Most of the wavelets frequency decompose the signals in a dyadic fashion. Thus, at $(j+1)^{th}$ level

of decomposition the wavelet coefficients become half in number compared to j^{th} level. This is equivalent to downsampling the data into half compared to the previous level. Based on this argument if we consider SF as the sampling frequency in Hz, at j^{th} level of decomposition, we will have frequencies ranging between $SF/2^{j+1}$ and $SF/2^{j}$ (this is analogous to band pass filtering the signal in the frequency bands of $SF/2^{j+1}$ and $SF/2^{j}$). In wavelet analysis, the signal in a desired frequency band can be obtained by performing inverse wavelet transform using only the detail coefficients that correspond to the frequency band. Nine levels of decomposition are used which allow to focus on the frequency of the uterine contraction (0.1 - 1 Hz).
In addition to time-frequency decomposition property, the *db* wavelets also effectively remove the (linear or nonlinear) trends in the data. The order of the wavelets determine the order of the trends (first, second, etc.) up to which it can remain orthogonal. Because the MMG data are trend free the inclusion of higher order terms is not necessary and the *db2* approach is sufficient (Hussain et al., 2009).
Usually, the variance of the wavelet coefficients is computed as an equivalent to the spectral power and is used to characterize the underlying dynamics. However, as higher decomposition levels are reached, fewer coefficients will be available and as a consequence the spectral power cannot be reliably computed. To overcome this impediment, the signal is reconstructed using the wavelet coefficient (at each level of decomposition) and finally in each band the Hilbert transform of the reconstructed signals is computed. In the chosen 30 s inspection window the mean value of the amplitude of the analytic signal is computed as an equivalent to the power of the signal. Let $y_{j,s}(k)$ represent the power of the signal from the sensor s at the j^{th} level of decomposition where k is the average of the inspection time window. To improve the signal level, in the next step $y_{j,s}(k)$ are integrated over all the sensors and from all the frequency bands. To discriminate between the contraction and non contraction periods, $y(k)$ is partitioned using the algorithm described in (Frey and Dueck, 2007) and in section 3.4.1.
Prior to the Hilbert transform of the wavelet decomposition (HTWD) approach, two additional methods were considered as possible candidates for the identification of the uterine contractile activity, see Appendix B.

3.4.1 Affinity propagation

Clustering data by identifying a subset of representative examples allows the detection of patterns in data and the processing of sensory signals. Most methods, including

the popular k-means clustering technique, use the data to learn a set of centers such that the sum of squared errors between data points and their nearest center is small. These methods (MacQueen, 1967) require the *a priori* specification of the number of exemplars which are then assessed by iterative refinement starting from a random initial choice. However, these techniques are sensitive to the initial selection and they work well only when the number of clusters is small and chances are good that at least one random initialization is close to a good solution.
The affinity propagation clustering (APC) algorithm introduced in (Frey and Dueck, 2007) takes a different approach. The method recursively transmits real-valued messages along edges of the network until a good set of exemplars and corresponding clusters emerges. Messages are updated on the basis of simple formulae that search for minima of an appropriately chosen energy function. At any point in time, the magnitude of each message reflects the current affinity that one data point has for choosing another data point as its exemplar. Figure 3.2 illustrates how clusters gradually emerge during the message-passing procedure.

Two kinds of messages are exchanged between data points and these messages can be combined at any stage to decide which points are exemplars and which are the points that belong to exemplars. The evidence for how appropriate is point k to serve as the exemplar for point i is given by the *responsibility* $r(i,k)$. The *availability* $a(i,k)$ provides the evidence for how suited would be for point i to choose point k as its exemplar.
In the context of uterine contraction detection, the inputs for the APC are the similarities $s(i,q) = -\left\|y_i - y_q\right\|^2$ between data points y_i and y_q, set to negative squared error (Euclidean distance). The APC does not require the *a priori* specification of the number of clusters. Instead, the algorithm takes as input a real number $s(k,k)$ for each data point k so that data points with larger values of $s(k,k)$ are more likely to be chosen as exemplars. These values are referred to as *preferences*. The values of the input preferences as well as the message-passing procedure can influence the amount of identified exemplars (number of clusters).
Real-valued messages are exchanged between data points of $y(k)$ until the optimal number of exemplars (equivalent to the cluster centroid in K-means algorithm) and corresponding clusters are found.
The rules for the computation of the responsibilities and availabilities are given below as in (Frey and Dueck, 2007) :

$$r(i,k) \leftarrow s(i,k) - max_{k' \neq k}\{a(i,k') + s(i,k')\} \tag{3.12}$$

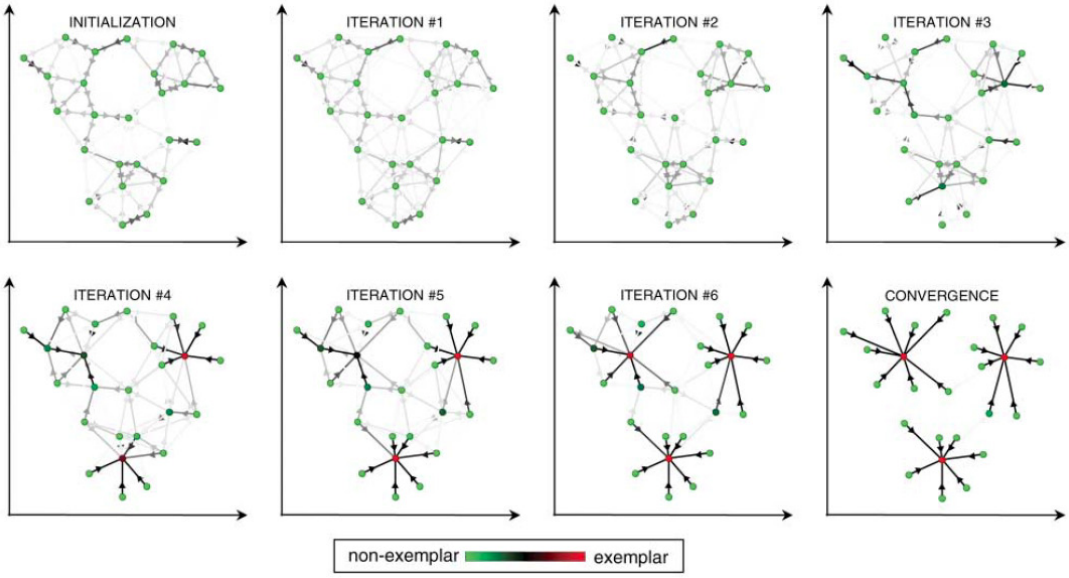

Figure 3.2: Affinity propagation. The figure shows an illustration for two-dimensional data points where negative Euclidean distance (squared error) was used to measure similarity. Each point is colored according to the current evidence that it is a cluster center (exemplar). The darkness of the arrow directed from point i to point k corresponds to the strength of the transmitted message that point i belongs to exemplar point k. (Figure from Frey, B. J. and Dueck, D. (2007). Clustering by passing messages between data points. *Science (New York, N.Y.)*, 315(5814):972-976. PMID: 17218491. Reprinted with permission from AAAS)

$$a(i,k) \leftarrow min\{0, r(k,k) + \sum_{i' \notin \{i,k\}} max\{0, r(i',k)\}\} \tag{3.13}$$

where i' and k' denote candidate exemplars.

To separate the clusters representing the contractions from clusters of non-contractile regions, the signal to noise ratio (SNR) is computed following:

$$SNR = \max\left(\frac{y(k)}{\min(y)}\right) \tag{3.14}$$

A certain percentage of SNR is defined as a threshold (a detailed description is given in section 3.4.2) and the clusters above this threshold are quantified as *contractile bursts* and the rest as *non-contractile bursts*. A contraction marker is constructed by defining one in the instances corresponding to the exemplars (i.e., integrated average power values) that exceeded the threshold and zero at all other instances.

3.4.2 Threshold fitting

A proper selection of threshold is a crucial part as it will determine the sensitivity/specificity of the algorithm and it mainly depends on how one decides to base the algorithm.
If one desires the algorithm to operate highly sensitive, more bursts will be quantified at the expense of identifying erroneous burst patterns. On the other hand if one wants the algorithm to operate highly specific only the prominent bursts will be identified at the expense of losing a few real bursts which are in the noise region. In this study the algorithm was set to operate highly specific. To estimate a threshold for the current study a stochastic model, based on the second order autoregressive process (AR2), is proposed:

$$s(t) = a_1 s(t-1) + a_2 s(t-2) + \eta(t) \tag{3.15}$$

where $a_1 = 1.81$ and $a_2 = -0.9$ are the parameters of the AR2 process and η is the Gaussian white noise. The estimation of the two parameters (a_1 and a_2) of the second order autoregressive model (AR2) was performed as follows. For a particular dataset (*MMGT202 39w0d*) the MMG data from each sensor was fitted using the second order autoregressive process. This resulted in different realizations (matching the amount of primary magnetic sensors) for each, first and second, parameter describing the process. In the next step, the median of all the realizations was considered and the resulting coefficients were used in the proposed stochastic model.
Next, $s(t)$ is simulated for a duration of 30 min with a sample frequency of 32 Hz. Further, the following two variables are considered for the proposed model: (i) θ, which determines the percentage of occurrence of the bursts in the data and (ii) ρ, which modulates the amplitude to the desired level. As done in MMG data analysis, $s(t)$ is divided into disjoint 30 s windows. In order to determine the burst locations, random numbers uniform distribution are generated for each window. If the random number generated for a window is less than or equal to θ a burst is inserted in that window. To model the contraction the data is separated from the window (in which the burst is to be inserted) and band pass filtered in the frequency band of 0.25 - 0.5 Hz using 4^{th} order Butterworth filter with zero phase distortion. In the next step the filtered data is inserted at the place of the original data. This procedure is repeated individually for all windows that are chosen for the insertion of bursts and denote the modified signal

as $s'(t)$. The SNR of $s'(t)$ is modified as follows:

$$F(t) = s'(t) + z(t) \cdot \frac{var(s'(t))}{var(z(t)) \cdot \rho} \tag{3.16}$$

where $z(t)$ represents the Gaussian white noise and *var* denotes variance.

3.4.3 Threshold selection

For the model described in 3.16 two parameters are varied:

- θ, which determines the percentage of occurrence of the bursts in the data
- ρ, which modulates the amplitude to the desired level

θ runs from 0.1 to 0.9 in steps of 0.1 (i.e., the inserted windows cover from 10 to 90% of the signal length in steps of 10%) and ρ runs from 1.2 to 9 in steps of 0.2 which yields SNRs similar to those observed in the real MMG data. $F(t)$ is processed using the same approach as performed for MMG data using the HTWD approach. For each value of θ, 40 different realizations of the data are synthesized by varying ρ between the specified range. In the next step, for each realization a threshold value is determined so that only true contractile regions are picked. That is, different threshold values are tried until all or a minimal number of the events are picked. This resulted in 40 different *intermediate* threshold values. In addition to that the SNR is also computed in that particular realization as performed for the MMG data (see equation 3.14). After this step, the mean of the thresholds, denoted with T and the mean of the SNRs, denoted with S, are computed for each ρ value. To this end T and S are modeled as an exponential decay function (see Figure 3.3) using equation 3.17, solved for the coefficients numerically using Newton-Raphson approach and obtain the coefficients $a = 1.179$ and $b = -0.273$.

$$T = a \cdot e^{b \cdot S} \tag{3.17}$$

Figure 3.4 (a) presents the case in which the first parameter θ was set to 0.1 (i.e., ten percent of the data - six windows - containing bursts) and the second parameter ρ was at its minimum value, that is, low SNR is produced. Figure 3.4 (b) presents the data simulated from the model for $\theta = 0.1$ and $\rho = 9$. The instances at which contractions are inserted are shown with thin dashed lines. Additionally, the marker computed based on the manually chosen threshold value that yielded the highest specificity is plotted over the synthetic signal.

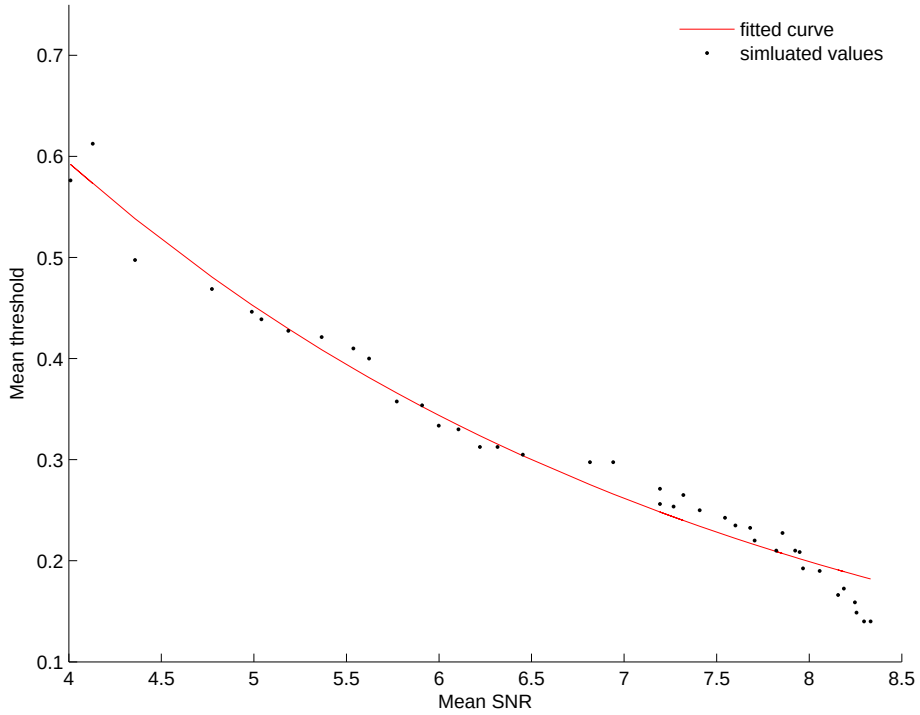

Figure 3.3: Threshold decay modeling. Mean of the thresholds and signal-to-noise ratios modeled as an exponential decay.

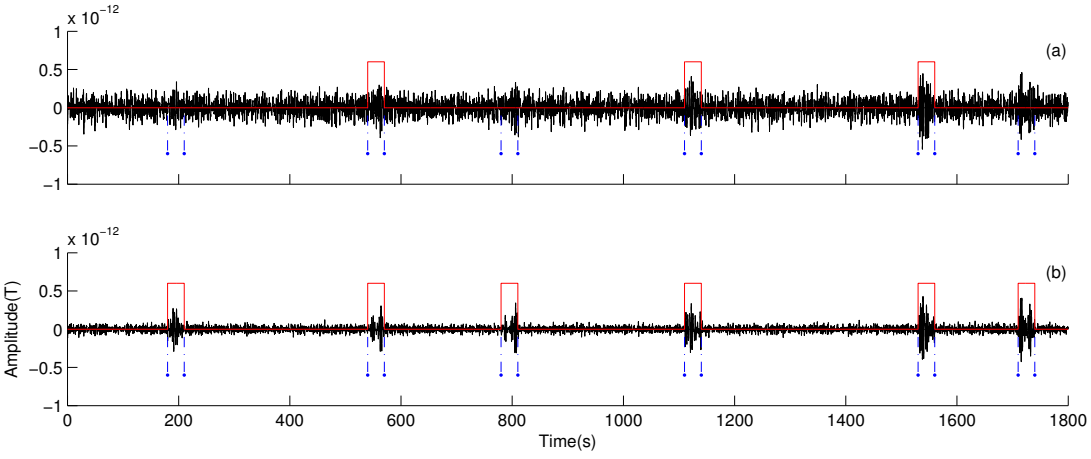

Figure 3.4: Example of low and high SNR. (a) low SNR, (b) high SNR in the synthetic signal that was created to compute the threshold. Figure from (Furdea et al., 2009).

From the simple model (see equation 3.17), we clearly note that for $SNR = 1$ one has to select all the exemplars that are greater than 90% of SNR (0.9·SNR) as a burst pattern. However, this cannot reflect the real scenario. Hence, if the $SNR \leq 1$ we set the algorithm not to mark any burst regions and consider this scenario as the limiting case of the method. For MMG signals, the SNR obtained using equation 3.14 is substituted in equation 3.17 to compute the threshold and identify the burst regions.

3.4.4 Comparison to IUPC data

Due to the need for a comparison with a gold standard, in a parallel study, a simultaneous IUPC/MMG recording was carried out with special arrangements to minimize interferences between the two systems (Eswaran et al., 2009). The performance of the HTWD approach was tested by applying it to the gold standard data set (obtained from the simultaneous IUPC/MMG recording) from the SARA database. A significant cross-correlation has been found between the IUPC signal and the contractile instances detected by the HTWD approach, $r = 0.83,\ p < 0.001$, with a delay of $-9.72\ s$. The result indicates that the delayed mechanical activity, displayed by the IUPC signal, follows the activity observed in the magnetic signal, see Figure 3.5. To further assess the degree of agreement in the contractions detected with the IUPC and HTWD methods, the rate of true positives (TP), true negatives (TN), false positives (FP) and false negatives (FN) was computed. The obtained values, $TP = 0.71$, $TN = 0.92$, $FP = 0.08$ and $FN = 0.29$ indicate a high degree of sensitivity and specificity between the two approaches. In addition, it was also shown that in parts of the data, the proposed method can also identify low-amplitude contraction, which mothers can not perceive (Eswaran et al., 2009).

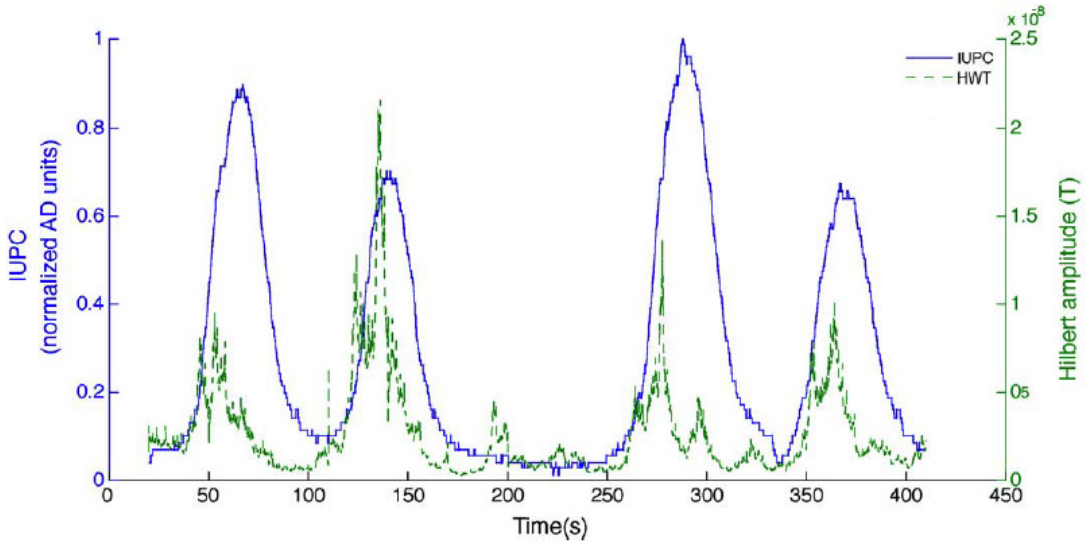

Figure 3.5: Comparison of the IUPC data with the outcomes of the HTWD algorithm. The delayed mechanical activity, displayed by the IUPC signal, follows the activity observed in the magnetic signal. Reprinted from the European Journal of Obstetrics & Gynecology and Reproductive Biology, Vol 144, Supplement 1, Eswaran, H., Govindan, R. B., **Furdea, A.**, Murphy, P., Lowery, C. L., Preissl, H. - Extraction, quantification and characterization of the uterine magnetomyographic activity - A proof of concept case study, pages S96-S100, ©2009, with persimisions from Elsevier.

3.5 Preliminary conclusions

A new method for the automatic detection of uterine contractile activity was introduced. MMG signals from a multi-sensor array are decomposed by wavelet analysis into multilevel approximate and detail coefficients. In each level, the signals are reconstructed using the detail coefficients followed by the computation of Hilbert transform. The Hilbert amplitude of the reconstructed signals from frequency bands ranging between 0.1 - 1 Hz is integrated over all sensors and frequency bands to increase the signal to noise ratio. The procedure is referred to as the Hilbert transform of the wavelet decomposition (HTWD). Using the affinity propagation clustering technique the contractile bursts are separated from the noise level and a single marker for the contractile events is created. The proposed technique has the advantage to capture the dominant frequency information, thus providing an accurate estimation of the contractile activity throughout the gestational age.
To determine its robustness, the method was applied on simulated MMG data, using a simple stochastic model. A comparison of the proposed HTWD approach with data obtained from IUPC revealed a significant correlation of the two measures. In addition, the method was applied to serial MMG recordings obtained from pregnant women with gestational age ranging between 36 and 41 weeks. The results are presented and discussed in chapter 5.
During a MMG recording, which typically lasts 30 min, subjects are instructed to sit still and try to avoid movement. However, during a session slight or sudden changes in the positioning of the body are inevitable. These movements lead to sporadic and spurious artifacts which remain blind to the filtering technique. The next chapter (4) presents a method, that relies on the computation of the center of gravity (CoG), developed to identify and discard MMG segments that are contaminated with movement artifacts.

4

Conduction velocity

The first section of this chapter presents the methodology to identify the uterine contractions using the power information obtained from individual sensors. The method described in chapter 3 was extended to provide a contraction marker for each magnetic sensor. The second section provides a description of an algorithm to identify and discard artifacts introduced by the movement of the subject. The last section introduces a novel approach to compute the conduction velocity (CV) of the multidimensional MMG signals (Furdea et al., 2011).

4.1 Introduction

The method described in chapter 3 has the advantage to capture the dominant frequency information, allowing the computation of a marker that labels the contractile events in a MMG recording. However, a single contraction marker is created for all sensors. This has the inconvenience that if one decides to investigate specific sensors, in some of them one might find instances labeled as *contractile pattern* although in reality there is no activity. Therefore, the approach presented in chapter 3 was extended to encompass all magnetic sensors, that is, for each sensor a contraction marker is computed using the signal power information from the respective sensor.
To compute the contraction marker (the label for the contractile events) in individual sensor data the procedure presented in section 3.4 was modified. More precisely, the mean value of the analytic signal (described in section 3.4) was integrated only over the decomposition levels leading thus to $y(k, s)$. In a next step $y(k, s)$ was partitioned using the APC algorithm as described in section 3.4.1 followed by the steps described in 3.4.2 and 3.4.3 to finally obtain the contraction markers for individual sensors.
By integrating over the frequency decomposition levels (and not over the sensors), the method becomes more susceptible to artifacts introduced by movement of the subject. Therefore, a new approach was adopted to identify and discard the time instances where such movement artifacts occurred.

4.2 Artifact rejection

SARA allows the recording of the magnetic fields that are associated to different biological processes such as fetal magnetocardiogram (fMCG), fetal magnetoencephalogram (fMEG), magnetomyogram (MMG) or maternal magnetocardiogram (mMCG) and voluntary contraction of the abdominal muscles. A previous study has shown that the activity associated to uterine contraction is mainly localized in the 0.1 - 1 Hz frequency band (Garfield and Maner, 2007).
When compared to the uterine contractile activity, some of the previously mentioned physiological processes, namely the fMEG and voluntary abdominal muscle contraction are high frequency by their nature (Buhimschi et al., 1997; Vrba et al., 2012). Therefore, in the context of the current work, the artifacts introduced by these processes can be easily removed (or at least attenuated to a level at which they become negligible) by using the available basic filtering techniques (i.e., by setting the appropriate parameters of a band-pass filter). After band-pass filtering, the MMG signals are confined to a band

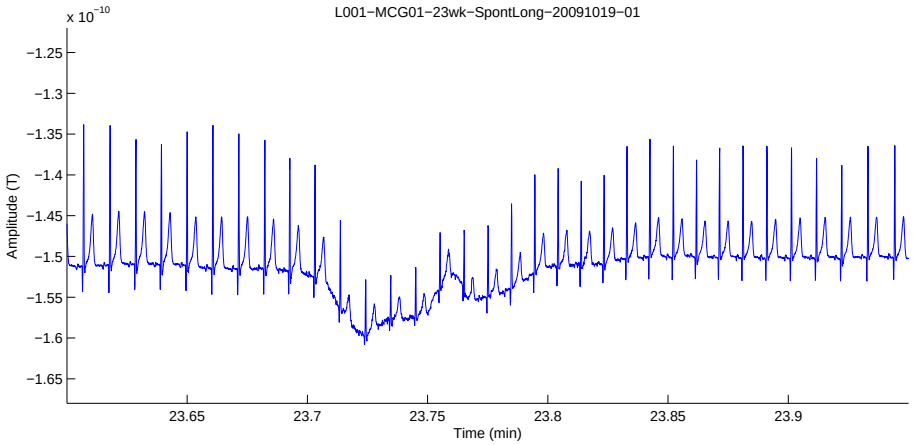

Figure 4.1: Example of an artifact in the mMCG introduced by subject movement*.

* two-dimensional representation

which is upper bounded by the frequency of the fetal and maternal heart rate (in the range of 1.1 - 2 Hz).

During a measurement, which typically lasts between 20 and 30 min, the subjects are requested to sit still and avoid any kind of movement as much as possible. However, slight adjustments of the body position are inevitable. The slight movement of the body is low frequency in nature (see Figure 4.1), similar to the uterine contractile activity, thus rendering the removal of motion artifacts (by current filtering techniques) inefficient. The elimination of such artifacts are of particular concern if one decides to extend the analysis to the level of individual sensors. The following sections introduce and describe a method to identify and discard the artifacts introduced by the movement of the subject. In particular, the detection of slow frequent movement artifacts is targeted.

4.2.1 Center of gravity of the R-peaks

To overcome the issue of artifacts introduced by the subject's movement the time segment, wherein a movement artifact occurs, is identified and rejected from the analysis. For this purpose, the R-peaks are extracted from the mMCG (Govindan et al., 2011; Ulusar et al., 2009) of an entire recording (see Figure 4.2).

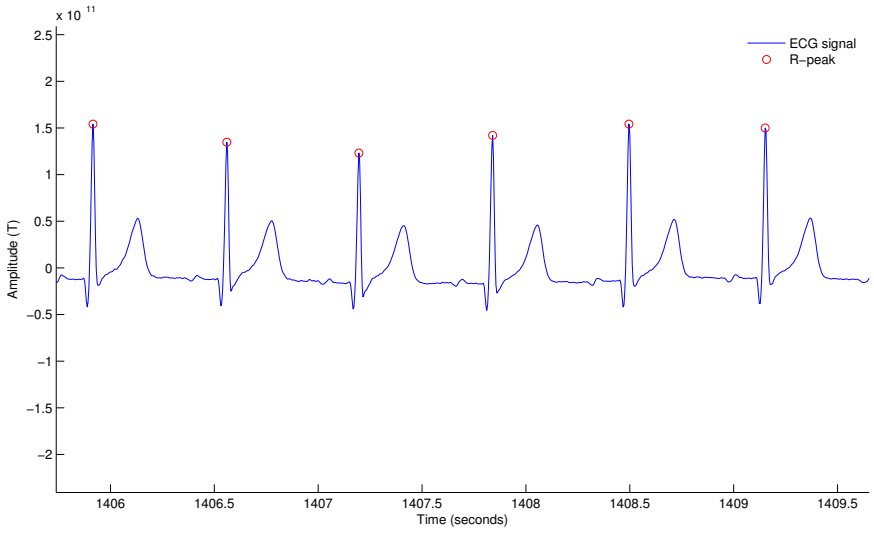

Figure 4.2: Example of R-peaks detected in the mMCG. Red circles represent the detected R-peaks.

In a next step the signals are partitioned into 3 *min* disjoint windows and in each window the center of gravity (CoG) for the R-peaks is computed.
The j^{th} sample of the R-peaks vector at k^{th} sensor is denoted as S_k^j and the corresponding amplitude is represented as A_k^j where $j = 1 \ldots m$ and m is the number of primary magnetic sensors. We define the CoG for the j^{th} sample as follows:

$$CoG^j = \frac{\sum_{k=1}^{\mathrm{m}} (x_k, y_k, z_k) \cdot A_k^j}{\sum_{k=1}^{\mathrm{m}} A_k^j}, \tag{4.1}$$

In any given inspection window, the average CoG is computed and denoted with m_{CoG}. In a next step, the pairwise distance from each R-peak's CoG to the m_{CoG} is computed and denoted with d_{CoG}. Whenever in the 3 *min* inspection window d_{CoG} exceeds a certain threshold, defined as

$$d_{CoG}(i) > m_{CoG} + 3 \cdot std(m_{CoG}) \tag{4.2}$$

where *std* denotes the standard deviation, the corresponding sample is marked as movement artifact (see Figure 4.4). Empirical observations have shown that equation 4.2 provides a fairly good discrimination of the peaks that correspond to maternal movement. This was also in agreement with the protocol recordings that were carried out during each measurement. Later on, whenever a sample marked as movement artifact is encountered in the analysis of the biological signals the corresponding inspection window is discarded from further analysis. A schematic representation of the movement detection algorithm is provided in Figure 4.3.
The algorithm for computing the uterine contractile activity marker was complemented with the movement detection algorithm and it represents the last preprocessing step prior to the computation of the HTWD (see Figure 4.5).

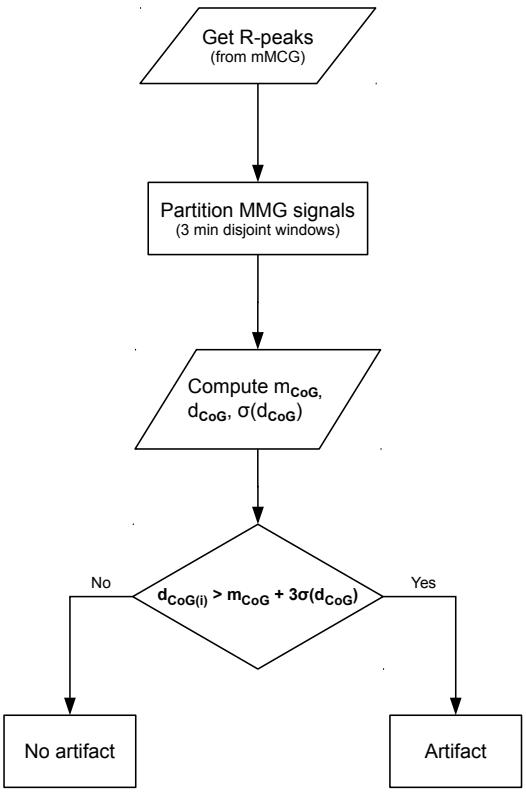

Figure 4.3: Schematic representation of the movement detection algorithm.

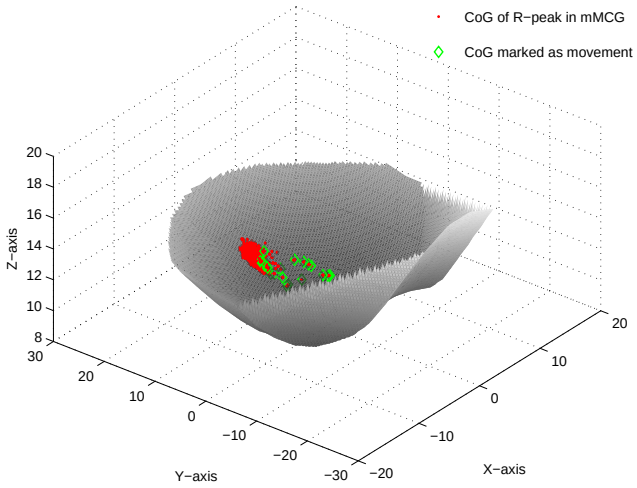

Figure 4.4: Example of movement detection in a 30 min recording. The grey surface corresponds to the 3D coordinates of the primary magnetic sensors. Red dots show the center of gravity of the R-peaks (detected in the mMCG) and green diamonds represent the center of gravity for the R-peaks (detected in the mMCG) identified as movement artifact.

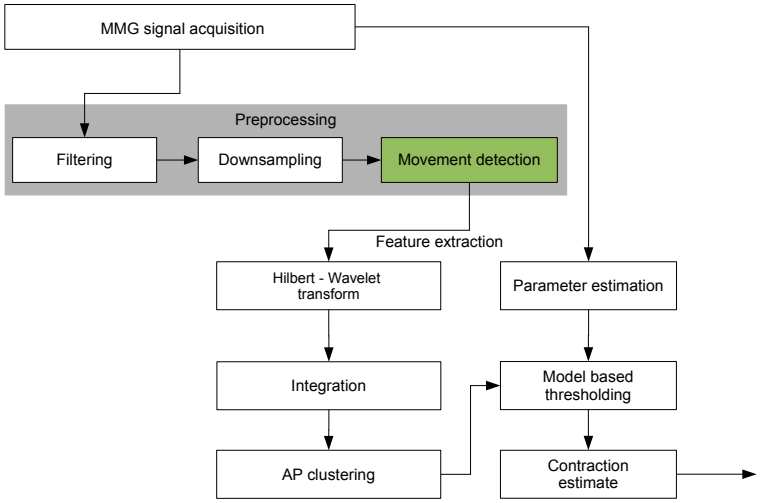

Figure 4.5: Schematic representation of the complemented uterine contraction detection algorithm. The movement detection (highlighted with green) was added to the preprocessing stage.

4.3 Conduction velocity

The propagation of AP through an adequate number of smooth muscle cells results in coordinated contractions of the myometrium. These contractions can simultaneously induce a progressive cervical dilatation and an increase of the internal uterine pressure which are both prerequisites for a successful delivery.
Several studies investigated the use of either EMG or MMG signals for the prediction of labor and for the discrimination of contractions leading to preterm delivery. Both time (Buhimschi et al., 1998; Verdenik et al., 2001) and frequency domain (Buhimschi et al., 1998; Doret et al., 2005; Eswaran et al., 2009; Garfield et al., 2005; Maner et al., 2003, 2006) parameters were analyzed and the most significant observable characteristic is the shift of the burst frequency components from low (in early gestational age) to higher frequencies (close to term and during labor). Such spectral changes were observed close to delivery (Eswaran et al., 2009; Vinken et al., 2009).
The spreading of the coordinated electrical activity (and the resulting magnetic activity) in the myometrium is a prerequisite for effective contractions (Garfield et al., 1988). The prediction of preterm labor on the basis of MMG signal frequency content could be tackled by means of a multichannel analysis. Therefore the conduction velocity (CV) of the propagating MMG signal could provide a fundamental contribution for the prediction of delivery. Muscle fibre CV has been considered an important physiological parameter as it reflects the membrane muscle fibre properties and thus the modifications of the peripheral properties of the neuromuscular system as a consequence of either pathology, fatigue, pain or exercise (Farina and Merletti, 2004).
The CV of electrical events in the myometrium is a concept that goes back to 1948 (Bozler, 1948). Early studies report that sheets of smooth muscle cells behave as a syncitium in the transmission of electrical activity. No direct protoplasmic connexions exist but several types of intercellular junction have been shown by electron microscopy. Areas of adjacent cells are parallel and separated by a gap between 0 to 30 nm where as much as 6% of the cell surface area can be involved (Duthie, 1974).
CV has been studied by many authors and there is a wide range of values that depend on the species and the equipment used (Lucovnik et al., 2011a; Miller et al., 1989; Miyoshi et al., 1998; Rabotti et al., 2010b; Vinken et al., 2009).
Early studies showed increased CV of the uterine myometrial cells before delivery and this has been attributed to the increase in the gap junction between the myometrial cells (Miller et al., 1989; Miyoshi et al., 1998). Garfield and colleagues have measured cell-to-cell conduction after they noted the presence of gap junctions (which are low-resistance

contacts for current spread) between myometrial cells during term and preterm labor (Garfield et al., 1977). A more recent study has shown that the power spectrum peak frequency of the uterine EMG, along with CV can identify more accurately true preterm labor than current clinical methods (Lucovnik et al., 2011a). The authors used a bipolar electrode setup and the electrode arrangement was standardized as follows (i) 2.5 *cm* electrode-electrode vertical and horizontal separation distances (measured from center to center), (ii) in a square-shaped pattern about the navel and with each electrode positioned in the vertex of each of the four corners of the square yielding a bipolar setup. This setup has the advantage (over a monopolar setup) of better signal quality, which in turn allows to identify individual uterine voltage peaks more accurately. However, the disadvantage of a bipolar setup is that purely vertical propagation produces a minimal measurement because of the common mode rejection of the amplifiers. Purely horizontal waves are registered, and these horizontally moving waves impinge at adjacent upper and lower pairs in rapid succession. This results in an underestimation of the signal time of arrival interval between electrodes and produces a poor CV estimation (Lucovnik et al., 2011b).

Recent studies also advanced the hypothesis that the analysis of the CV in combination with other parameters that are derived by the electrohysterogram (EMG) has potential value for discriminating between productive and unproductive uterine contractions (Rabotti et al., 2010b; Vinken et al., 2009). EMG analysis poses demanding requirements with respect to the number and relative position of the recording channels that are used for deriving the value of CV, that is, the value of velocity along the propagation direction. As an example, the use of two recording channels may lead to inaccurate CV values that do not correspond to the actual values (Rabotti et al., 2011).

At this time the prognostic capability of the CV has only been evaluated by means of EMG (Lucovnik et al., 2011a; Rabotti et al., 2011). The MMG technique has the potential to provide a better estimate of the CV mainly because when using magnetic signals the inconvenience related to the spatial location and distribution of the recording sensors is eliminated. Earlier studies suggest that there might be a preferential direction of propagation in the human uterus (Planes et al., 1984; Wolfs and Rottinghuis, 1970). For geometrical and physical reasons, this could result in the expulsion of the fetus given that, during active labor, contractions propagate generally from the fundus toward the isthmus. This would also support the idea that although there may not be a specific type of individual pacemaker cell, there may be general pacemaker regions later in gestation (Garfield and Maner, 2007). But again, no clear direct evidence of pacemaker cells has

been found in humans.

To study the CV in MMG signals, first the contractile patterns are detected and marked. The detection is performed within a 30 s sliding non-overlapping window, in each sensor as described in (Furdea et al., 2009) and section 4.1. Second, the sensor space is subdivided into four quadrants (Q) or regions (see Figure 4.6). To compute the delay (i) pairwise combinations of quadrants are created (e.g., $Q1$-2, $Q1$-3, $Q1$-4, etc.), (ii) inspection windows are identified wherein contractile activity simultaneously occurs in any given quadrant pair and (iii) the delay between the center of gravities (CoG), that correspond to different quadrants in a pair, is computed using the high dimension cross-correlation function (HDCC) (see section 4.3.2). Once the delay is computed the CV can be easily calculated by dividing the euclidean distance between CoGs that belong to different quadrants in a pair, and the amount of time by which they are delayed (the index k at which the euclidean distance between the two CoGs is computed is given by the same index at which the delay occurs).

$$CV = \frac{\|CoG_{i,k} - CoG_{j,k}\|^2}{t_k}, \text{ where } i \neq j \tag{4.3}$$

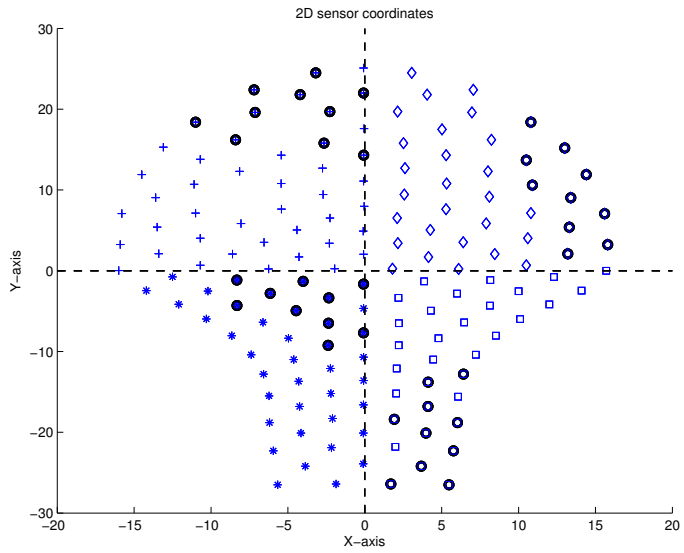

Figure 4.6: Partitioning of the sensor space in four quadrants according to their x and y coordinates. Diamonds, crosses, asterisks and squares are marking the sensor coordinates that belong to the first, second, third and fourth quadrant, respectively. Black circles mark the sensors in which the AR2 processes are modified. Adapted from (Furdea et al., 2011), © 2011 IEEE.

4.3.1 Center of gravity and Hilbert amplitude

The j^{th} sample of the MMG signal at k^{th} sensor is denoted as S_k^j and the corresponding amplitude of the Hilbert transform is represented as H_k^j where $j = 1 \ldots n$ with n representing the number of primary magnetic sensors. The center of gravity (CoG) for the j^{th} sample is defined as follows:

$$CoG^j = \frac{\sum_{k=1}^{\mathrm{n}} (x_k, y_k, z_k) \cdot H_k^j}{\sum_{k=1}^{\mathrm{n}} H_k^j}, \tag{4.4}$$

The Hilbert transform of the MMG signal at k^{th} sensor can be easily computed using the MATLAB (Mathworks Inc.) built-in function. The function returns a complex signal as a linear combination of the original signal with its Hilbert transform (see equation 3.1).

4.3.2 High dimension cross-correlation function (HDCC)

To compute the delay between pairs of CoGs (where each CoG is represented as a 3-dimensional vector) time shifted correlation analysis is performed. For this purpose CoGs from one of the quadrants are held constant and the CoGs from the second are shifted (back in time) by τ samples. The last τ samples are discarded from the CoGs that are held constant in order to match the number of samples in the later. To this end the correlation coefficient is computed between these two CoGs. However, in this approach there is an element of bias as the correlation coefficient is computed for different number of samples for each shift. To avoid this bias and thereby to quantify the correlation correctly, for each shift τ, the same number of data points (that corresponds to number of samples minus the maximum lag) are discarded from both CoGs. The maximum lag up to which the correlation analysis is performed is therefore set to 15 s of data. For each shift, the correlation is quantified using the equation introduced in (Smilde et al., 2009):

$$C = \frac{tr(X^t Y)}{\sqrt{tr(X^t X) tr(Y^t Y)}}, \tag{4.5}$$

where X^t and tr(X) represents the transpose, respectively the trace (the sum of diagonal elements) of the matrix X.

4.3.3 Modeling

A stochastic model based on the second order autoregressive process (AR2) is proposed:

$$X(t) = a_1 X(t-1) + a_2 X(t-2) + \eta(t) \tag{4.6}$$

where the initial parameters of the AR2 process are computed as in (Furdea et al., 2009). The purpose of the proposed stochastic model is to mimic the amplitude of the MMG signals by modifying the parameters of the model. This model is just sufficient to understand the limitation of the approach as to capture the delay between the selected sensors. Moreover, this model cannot explain the different frequency characteristic that may be present in the measured MMG signals.

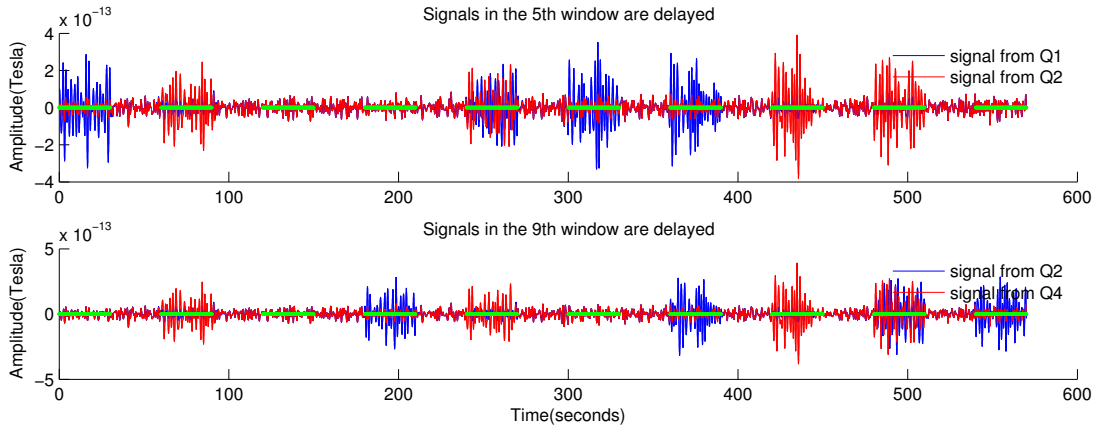

Figure 4.7: An example of the modeled signals. Top: signals belonging to $Q1$ (blue) and $Q2$ (red), note that in the fifth active window the signal in $Q2$ is delayed with respect to the signal in $Q1$. Bottom: signals belonging to $Q2$ (blue) and $Q4$ (red), note that in the ninth active window the signal in $Q4$ is delayed with respect to the signal in $Q2$. Figure from (Furdea et al., 2011), © 2011 IEEE.

To match the total number of magnetic sensors, n different realizations of the AR2 process are created for a duration of 9.5 min with a sampling frequency of 250 Hz. The sensor space is divided into four quadrants and in each quadrant ten sensors are chosen where burst activity will be inserted. For the actual data analysis the algorithm will perform further operations only if the number of active sensors (NAS), that is, the amount of sensors wherein contractions were detected, exceeds the preset value of ten sensors. Next, $X(t)$ is divided into disjoint windows and alternate every 30 s between *active* and *rest* periods. During the active periods the signals in the ten selected sensors

are replaced with a filtered (bandpass filter at 0.35 - 0.8 Hz) and amplified version of the corresponding original AR2 processes. The first four active periods the signal is modified only in one quadrant, that is, in the first active period signals are modified in $Q1$, in the second active period in $Q2$, etc. Starting with the fifth active period the signal is modified in quadrant pairs, that is, in the fifth active period, signals are modified in $Q1$-2, in the sixth period in $Q1$-3, etc. In addition, whenever signals are modified in quadrant pairs, a delay of 5 ± 1 seconds is introduced in the signals of the second quadrant of the pair. The duration of the delay was arbitrarily chosen and the values were drawn from a Poisson random distribution. For a schematic representation of the model with the modified signals see Figure 4.7.
The results of the event based simulation and the results obtained by applying the conduction velocity approach are presented in chapter 5.

5

Application to biological data

This chapter discusses the application of the different methods described in the third and fourth chapter and to characterize the uterine contraction signals. In the first section, serial MMG recordings, obtained from six subjects in different gestational age, were investigated with the aim to automatically identify and mark the time segments which are corresponding to uterine contractile activity.
The second section presents the results of the conduction velocity analysis in 45 serial MMG recordings obtained from nine subjects.

5.1 Contraction burst identification using the global power of multisensor data

Six healthy pregnant women, one of pre-term and five of term, at gestational ages between 36 and 41 weeks were investigated (a total of seven datasets). Table 5.1 presents subject and recording related information.

Subject ID	GA [days]	Duration	Type of delivery
MMGP201	252	15 min	normal
MMGT201	273	20* min	normal
MMGT202	273	20 min	normal
MMGT203	262	20 min	normal
MMGT204	265	20 min	normal
MMGT205	281	20 min	normal

* recording split in two separate datasets

Table 5.1: Contraction marker computation: overview of the investigated datasets

The uterine activity was recorded with the 151 channel SARA system installed at University of Arkansas for Medical Sciences, Little Rock, USA. Each recording session was designed to last 20 min at a sampling rate of 250 Hz. Based on comfort of the pregnant women, the recording on the preterm subject *MMGP201 36w0d* lasted only for 15 min and for one term subject *MMGT201 39w0d* two shorter duration recordings with a break in between were performed. The resulting two data sets were analyzed and presented separately. The study was approved by the Institutional Review Board and all subjects signed the informed consent prior to participation.
For a typical data set, *MMGt205_40w1d*, Figure 5.1 presents in (a-d) the mean of the Hilbert-wavelet transform (in each 30 s non-overlapping inspection window) integrated across all sensors in four different frequency bands that range between 0.0625 - 1 Hz. It can be observed that, despite the notch filter, the 0.25 - 0.5 Hz band is the highest active band. However, MMG activity can also be seen in the neighboring bands suggesting, for this particular case, a spread of contractions through the entire 0.125 - 1 Hz range. In addition, Figure 5.1 e) depicts the integrated signal $y(k)$ (see section 3.4) over all sensors in the four frequency bands Figure 5.1 a) - d). Red diamonds represent the instances that exceed the threshold (see section 3.4.2) and received the *contractile pattern* label. Figure 5.2 illustrates the estimated contractions in the seven datasets. For each dataset, the contraction marker is plotted over the pre-processed signal, obtained from one

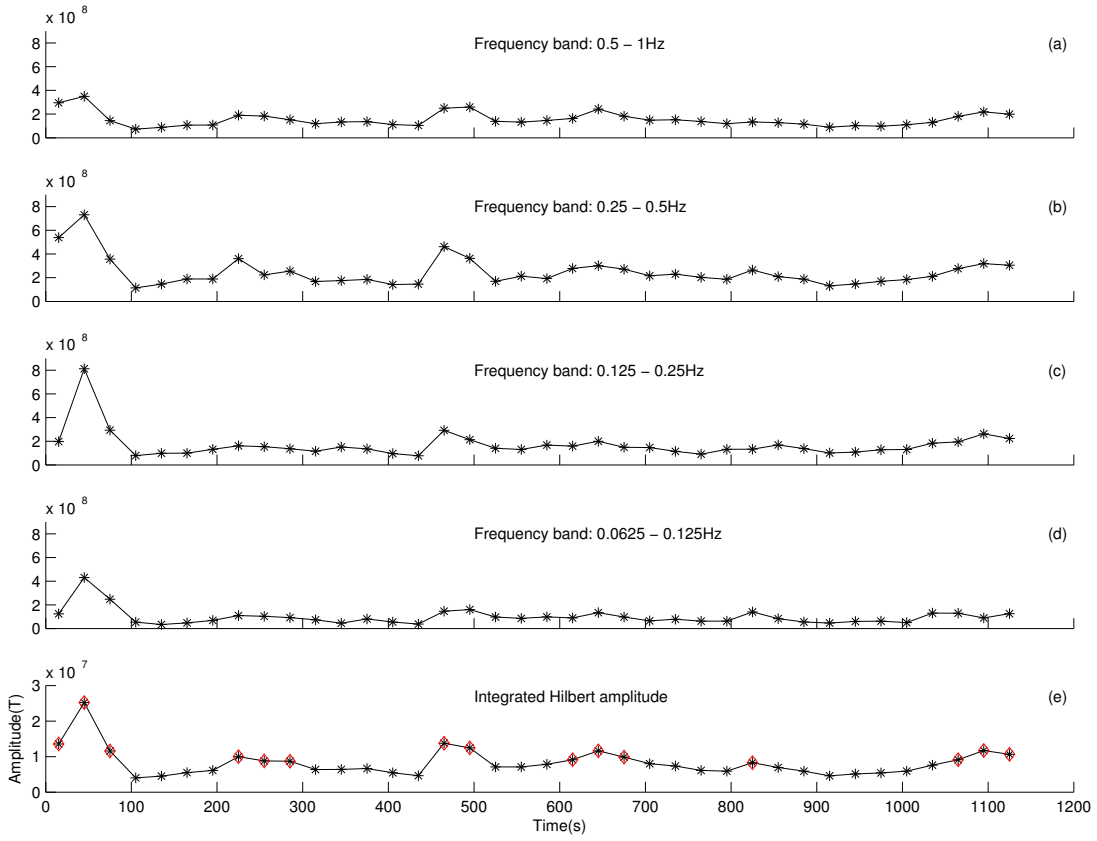

Figure 5.1: Example of the mean Hilbert-wavelet transform. The mean values are computed in each 30s non-overlapping inspection window. Dataset MMGt205_40w1d: (a-d) The mean of the Hilbert-wavelet transform integrated across all sensors in four different frequency bands ranging between 0.0625 - 1 Hz. (e) The integrated signal $y(k)$. Red diamonds represent the instances that exceed the threshold. Figure from (Furdea et al., 2009).

representative sensor with the highest SNR.

Here, the APC algorithm is applied on the integrated Hilbert amplitude from all the sensors and from all the frequency bands. As a result the contraction marker incorporates information from all the investigated frequency bands (0.1 - 1 Hz). Moreover, by using this approach the contractions which are identified are characteristic of the highest active frequency band. For the same dataset, *MMGt205_40w1d*, Figure 5.3 presents the spatial distribution of the Hilbert-wavelet amplitude (averaged over the 0.0625 - 1 Hz frequency band). It can be observed that there is an agreement between the peaking activity and the contraction marker (see Figure 5.2 and 5.3).

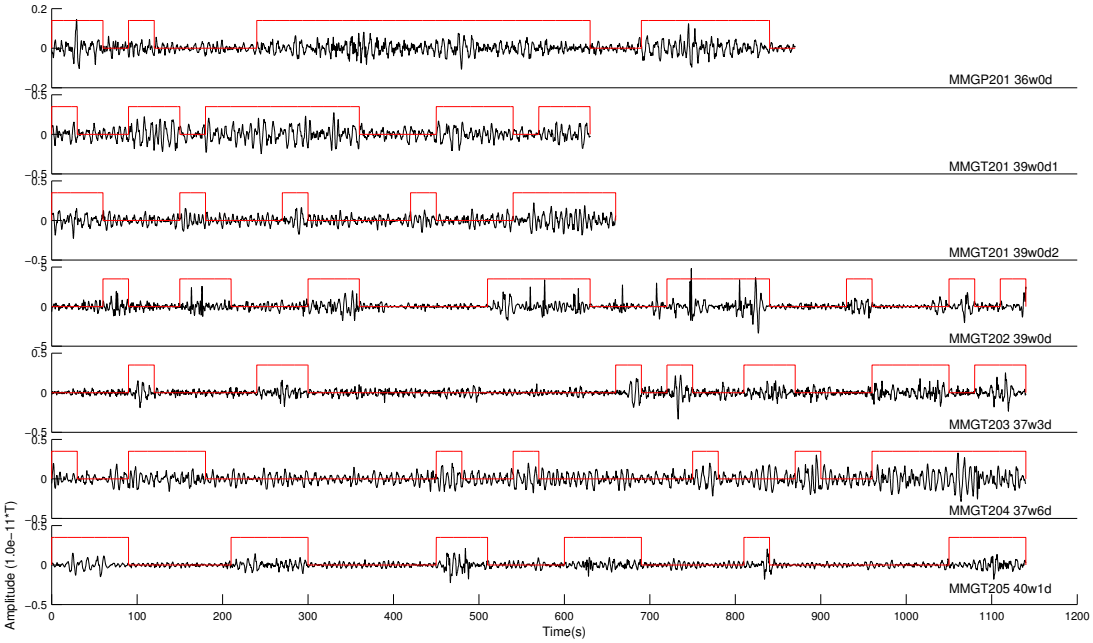

Figure 5.2: Estimates of the contractions detected in seven data sets. The contraction marker (red) is plotted over the pre-processed MMG signal (black). An agreement between the bursty activity and the contraction marker can be observed. The MMGP and MMGT prefixes indicate the preterm and term patients, respectively. The prefixes are followed by the patient code and gestational age (week and day). The first and second recordings of MMGT201 39w0d are marked with 1 and 2, respectively. Figure from (Furdea et al., 2009).

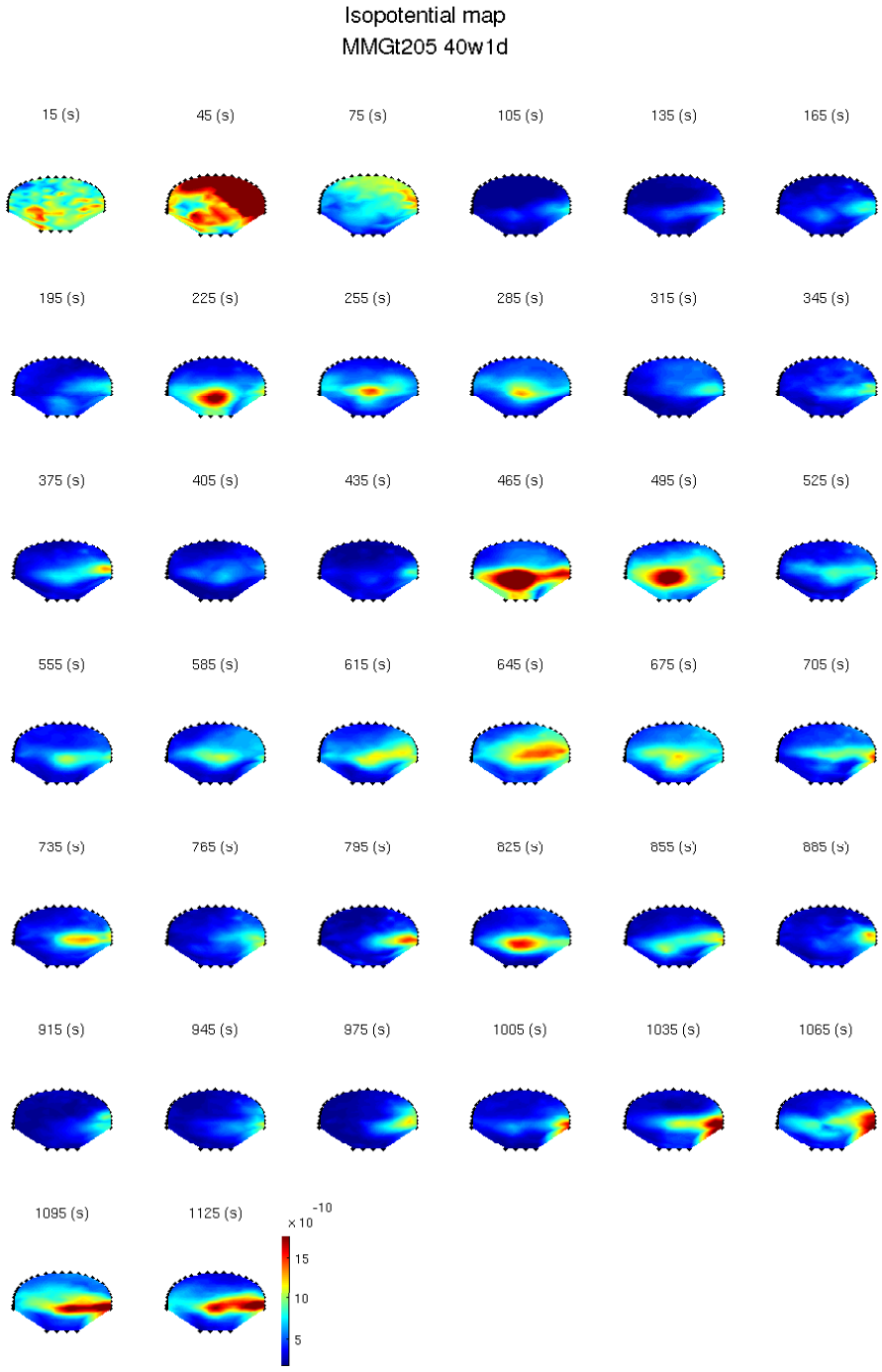

Figure 5.3: Isofield map of the spatial distribution of the mean Hilbert-wavelet amplitude. The mean values are computed for every sensor in each $30s$ non-overlapping inspection window and integrated over four frequency bands ranging between 0.0625 - 1 Hz. The data is presented for subject *MMGt205 40w1d*. Warm colors indicate high and cold colors indicate low mean Hilbert-wavelet amplitude, respectively.

5.1.1 Contraction burst identification in serial MMG data

The contraction burst detection algorithm was applied to biological datasets using the methods described in chapter 3. Artifacts introduced by the movement of the subject were exclded prior to the computation of the contraction marker (see Figure 4.5). Table 5.2 provides a summary of the serial MMG recordings. The first column of the table contains the subject ID, the second columns shows the amount of recordings performed with one subject. Column three and four indicate the gestational age (GA) in weeks wherein the first and last recording were performed. The fifth column displays the approximate duration of one recording. The last column of the table indicates whether the delivery was performed normally or by C-section. In all subjects the time to delivery was greater than 24 hours. The term gestational age is related to the age of a fetus and it indicates the amount of time a baby has been in the uterus. It is counted from the subject's last menstrual period and in the clinical practice it is usually expressed in completed weeks plus the number of day in the current week, e.g., $37w2d$. However, because the statistical analysis required continuous data, the gestational age was converted to days.

Subject ID	Recording				Type of delivery
	Total	First [days]	Last [days]	Duration	
L001	14	161	266	30 min	normal
L002	5	217	259	30 min	C-section
I021	4	224	260	10 min	normal
I022	4	224	252	10 min	normal
I023	4	224	273	10 min	normal
I029	4	238	287	10 min	normal
I035	4	196	238	10 min	normal
I012	3	231	280	10 min	C-section
I028	3	224	260	10 min	normal

Table 5.2: Overview of the serial MMG recordings.

The HTWD method proposed for the detection of contractile events is applied on the MMG signals collected from the subjects listed in table 5.2. For subject L001, typical results obtained from the time-frequency decomposition are presented in Figure 5.4 and 5.5. The figures illustrate the contour maps of the mean HTWD derived from recordings that correspond to the 23^{rd} (161 days) and 37^{th} (260 days) week of gestation, respectively. The mean HTWD values are computed in each 30 s non-overlapping inspection window. In each figure the contraction marker is displayed at the bottom

of the top-right subplot. It can be observed that in early gestation the bursts have a longer duration and a smaller amplitude but as the subject approaches term the bursts tend to become shorter with higher amplitude.

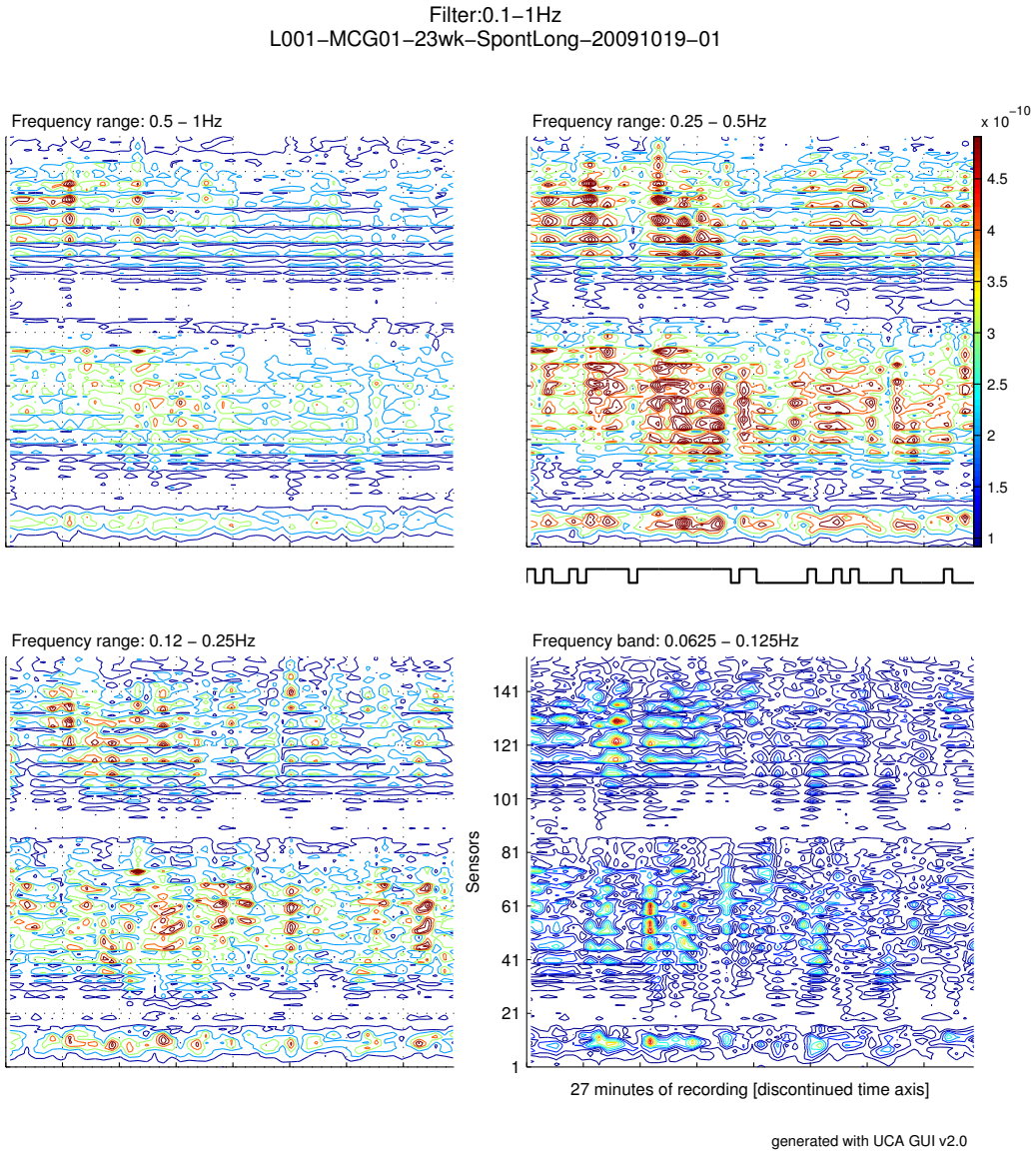

Figure 5.4: Mean HTWD of data collected in the 23^{rd} week of gestation. Data is presented for subject L001 in the four frequency bands ranging between 0.0625 - 1 Hz. Mean values of the HTWD computed in 30s non-overlapping inspection windows are plotted for each sensor. The discrete-time binary decision signal which marks the contractile events is shown at the bottom of the top-right subplot.

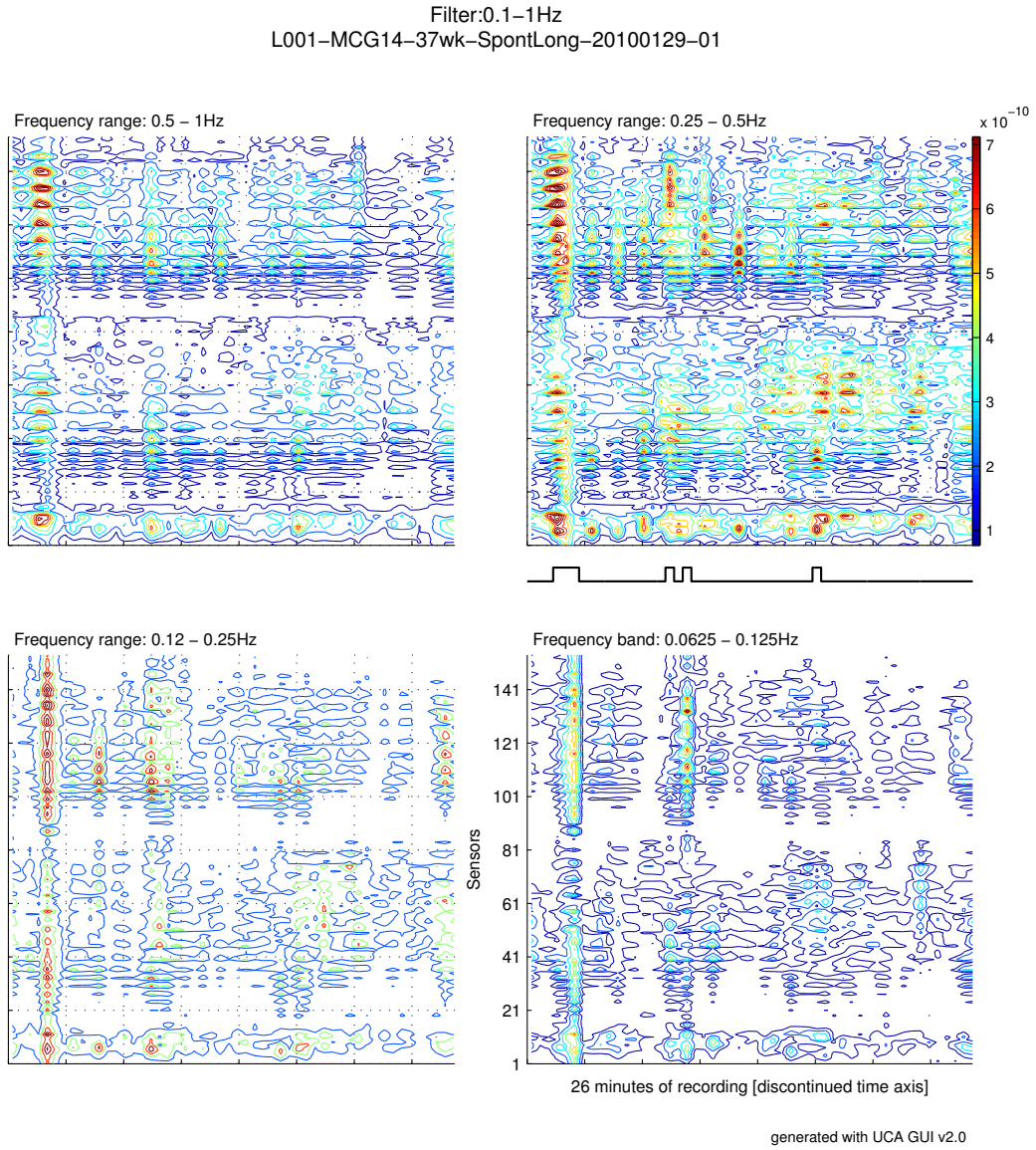

Figure 5.5: Mean HTWD of data collected in the 37^{th} week of gestation. Data is presented for subject L001 in the four frequency bands ranging between 0.0625 - 1 Hz. Mean values of the HTWD computed in 30s non-overlapping inspection windows are plotted for each sensor. The discrete-time binary decision signal which marks the contractile events is shown at the bottom of the top-right subplot. Notice the increase in power compared to data collected in the 23^{rd} week of gestation.

In a next step, the mean burst duration (BD) along with the standard deviation of BD and the median of BD are computed to study their variation with the GA. In addition, for the same purpose, the mean burst frequency (BF) along with the standard deviation of the BF and the median BF are computed. Table 5.3 presents the mean BD, $std(BD)$ and GA for subject L001.

Subject L001		
mean BD [s]	std(BD) [s]	GA [days]
70.9	93.2	161
130.0	168.4	168
106.7	113.4	175
37.5	13.9	182
120.0	195.1	196
105.0	90.8	203
63.0	62.4	217
42.0	21.0	224
40.0	15.0	231
36.0	12.7	245
36.0	13.4	252
50.0	49.7	259
45.0	30.0	260
37.5	15.0	266

Table 5.3: Mean BD (in seconds), std(BD) (in seconds) and GA (in days). Data computed for subject L001.

Negative significant correlations were found between the mean BD and GA, $p(two\text{-}tailed) < 0.01,\ r = -0.679$ (see Figure 5.6). The interaction between $std(BD)$ and GA showed also a negative correlation which was significant at $p(two\text{-}tailed) < 0.05,\ r = -0.653$. Similarly, the median BD correlated negatively with the GA, $p(two\text{-}tailed) < 0.05,\ r = -0.554$. No significant correlations were found between GA the mean BF, $std(BF)$ or median BF.

Due to insufficient amount of available recordings, no statistical test were carried out on the data of the remaining subjects. However, in participant L002, I012, I021 and I023 descriptive statistics show, similarly to the observations made in subject L001, a decrease in the mean BD and $std(BD)$ with the increase of GA (see Table 5.4).

The availability of several longitudinal recordings in subject L001 (see Table 5.2) rendered possible the analysis of the power density of the uterine MMG bursts. Many studies carried out on EMG signals collected from pregnant women have shown that the power density of uterine bursts in subjects during active labor peaked at $0.71 \pm 0.05\ Hz$

Subject L002			Subject I012		
mean BD [s]	std(BD) [s]	GA [days]	mean BD [s]	std(BD) [s]	GA [days]
158.6	198.0	217	110.0	113.6	231
51.0	37.5	224	60.0	52.0	260
78.7	47.9	231	45.0	21.2	280
72.0	83.9	238			
36.7	20.0	259			
Subject I021			**Subject I023**		
mean BD [s]	std(BD) [s]	GA [days]	mean BD [s]	std(BD) [s]	GA [days]
130.0	121.3	224	97.5	115.9	224
70.0	45.8	245	50.0	17.3	238
50.0	34.6	248	50.0	17.3	252
45.0	21.2	260	30.0	0.0	273

Table 5.4: Mean BD, std(BD) and GA. Data computed for subjects L002, I012, I021 and I023.

as compared to non-laboring term patients $0.48 \pm 0.03\ Hz$ (Garfield et al., 2005, 1998; Maner et al., 2006).

Due to the limitations imposed by the dyadic decomposition of the $db2$ wavelet, the decompositions closest to those reported by Garfield et al. were (i) low frequency 0.25 - 0.5 Hz and (ii) high frequency 0.5 - 1 Hz. Based on this, the time-frequency analysis on the spatial-temporal data obtained from uterine MMG recordings was performed to understand the variation of frequency of the process as a function of

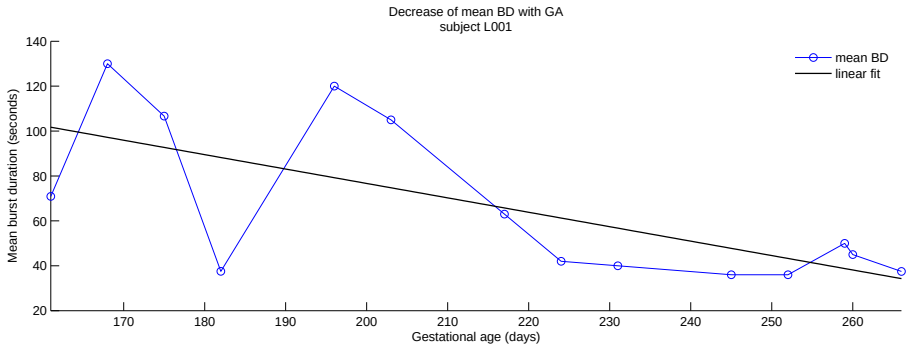

Figure 5.6: Decrease of mean BD with GA in subject L001. A linear fit is computed and overlaid on the data collected along the gestational age.

time. To quantify the power, the average of the Hilbert amplitude in both bands was computed.

In order to understand the shift in the power from lower-frequency to higher-frequency, the ratio of the power (high to low) was computed in the two bands. This ratio was calculated for MMG signals from each SARA sensor in the instances where contraction was detected. Figure 5.7 shows for subject L001 a contour diagram of the power ratio overlaid on the magnetic sensor array covering the maternal abdomen. For the sake of simplicity, the power ratio in the first three (top) and last (bottom) three recordings is presented. The top row shows, from left to right, the ratio of power (high to low) in the data collected between the 23^{rd} and 25^{th} week of gestation. Similarly, the bottom row illustrates (from left to right) the ratio of power (high to low) in the data collected between the 37^{th} and 38^{th} week of gestation (subject L001 underwent two recording sessions in the 37^{th} week of gestation). The frequency content of the MMG bursts is color coded and the contour plot is overlaid on the magnetic sensor map to show the spatial distribution. Warm colors indicate an increase in the power ratio of the MMG signals.

The map reflects the progression of change in the power shift towards higher-frequency starting from the first recording (23^{rd} week of gestation) to the last recording (38^{th} week of gestation) before the subject went into active labor. In addition, based on the enhanced SARA spatial resolution, a wider distribution of the increased MMG power ratio can be observed over larger sensor area as the uterus prepares to approach towards labor.

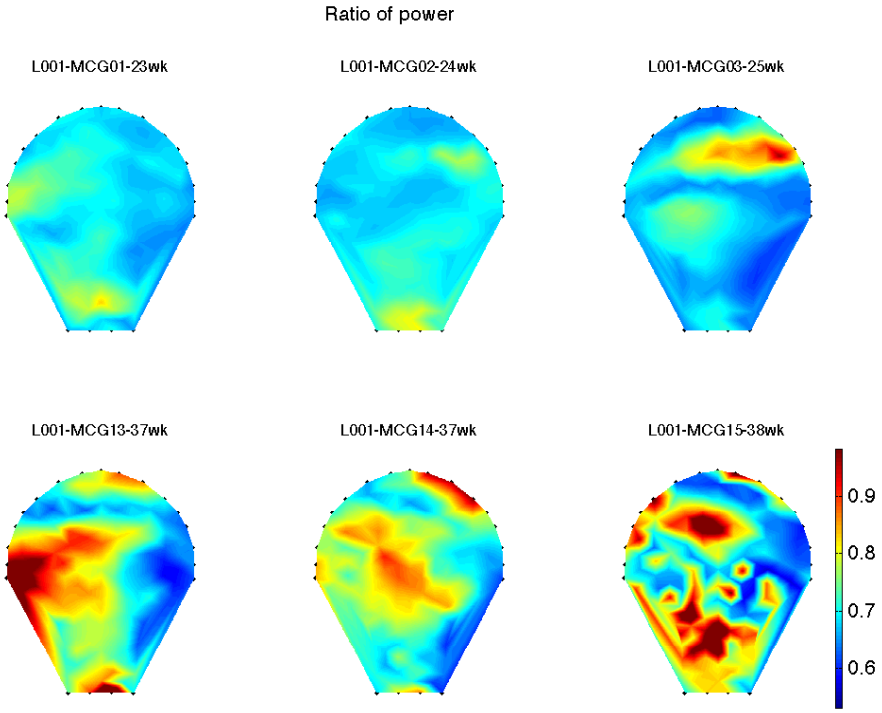

Figure 5.7: The ratio of power in higher-frequency (0.5 - 1 Hz) **to lower-frequency** (0.25 - 0.5 Hz) **bands.** Typical data is provided for subject L001. Top row shows the ratio of power in the first three recordings (collected between the 23^{rd} and 25^{th} week of gestation) and the bottom row presents the ratio of power in the last three recordings (collected between the 37^{th} and 38^{th} week of gestation). The frequency content of the MMG bursts is color coded and the contour plot is overlaid on the magnetic sensor map to show the spatial distribution.

5.2 Conduction velocity

5.2.1 Event based simulation

Results of the event based simulation which was described in subsection 4.3.3 are summarized in Table 5.5. As a reminder for the reader, the event based simulation was necessary to evaluate whether the high-dimension cross-correlation (HDCC) is able to capture the delay between CoGs belonging to different quadrant pairs. For this purpose the MMG signals were modeled using an AR2 model. The purpose of the proposed stochastic model was to mimic the amplitude of the MMG signals by tweaking the parameters of the model. The model is just sufficient to understand the limitation of the approach as to capture the delay between the selected sensors and it cannot explain the different frequency characteristic that may be present in the measured MMG signals (see subsection 4.3.3 for more details).
The first row in Table 5.5 contains the average delay that was inserted in the preselected ten sensors. The duration of the delay was arbitrarily chosen (± 5 s) and the values were drawn from a poisson random distribution. The second row shows the delay as computed by the HDCC function. The results show that the HDCC which was described in section 4.3.2 is able to reliably capture the delay between the CoGs of the simulated data.

Delay	Quadrant pair					
	$Q1$-2	$Q1$-3	$Q1$-4	$Q2$-3	$Q2$-4	$Q3$-4
Inserted	5.09	4.90	5.04	4.93	4.98	4.98
Detected	5.31	4.91	5.13	4.75	5.09	4.94

Table 5.5: Event based simulation results. The delay as inserted in the stochastic model (first row) and as captured by the high-dimension cross-correlation function (second row). Table from (Furdea et al., 2011), © 2011 IEEE.

5.2.2 Conduction velocity estimation in serial MMG data

To estimate the CV the contraction burst detection algorithm described in chapter 3 was applied to biological datasets, followed by the approach described in chapter 4. Again, the rejection of the artifacts introduced by the movement of the subject was performed prior to the computation of the contraction marker (see Figure 4.5).
Figure 5.8 shows the CV in the nine investigated subjects, obtained from the analysis of each quadrant pair over the gestational age.
A total of 45 recordings were investigated (see Table 5.2). The values for each day were obtained as follows: for any given quadrant pair, in each *active* inspection window (see section 4.3.3) the delay between corresponding CoGs was computed using the HDCC. In a next step, a bootstrap test was conducted. Here, the null hypothesis was that the delay identified in the original data was due to random chance and it was tested against the alternate hypothesis that the delay was not due to a random process, i.e., the CoGs represent delayed versions of the same process. In order to test the null hypothesis, surrogate data was generated by shuffling blocks of data, followed by the computation of HDCC (as done for the original data) on the block-shuffled data. By using block-shuffling instead of random-shuffling, the (two-point) correlations properties of the original signals remain preserved (Govindan et al., 2008). This property is necessary to correctly address a certain type of null hypothesis that is related to biological signals as presented here.
Based on earlier work of Schreiber and Schmitz (Schreiber and Schmitz, 2000), to reject the null hypothesis at $\alpha = 0.05$ level, a total of $N = 100$ different surrogates were synthesized, wherein data were block-shuffled. If the delay in the original data was greater than the K^{th} maximum or less than the K^{th} minimum of the delay of all the surrogates then the null hypothesis could be rejected, that is, the detected delay was significantly different compared to the delay coming from a block-shuffling process. In a next step, the velocity (for inspection windows wherein contraction was detected) was calculated as the ratio of the distance between CoGs (belonging to different quadrants) and the delay between the same CoGs. In case of negative delay, its absolute value was used (at this point the focus was the temporal separation rather than the direction of information flow).

Finally, for a given dataset the CV is quantified by taking its highest value from all quadrant pairs. Table 5.6 presents the CV values which were obtained in the 45 investigated recordings (that belong to the nine subjects). The delay values that correspond to the CV values presented in Table 5.6 are summarized in Table 5.7.

GA [days]	Conduction velocity values [cm/s]								
	Subject								
	L001	L002	I021	I022	I023	I029	I035	I012	I028
161	6.02								
168	4.06								
175	5.68								
182	6.91								
196	5.07						1.45		
203	10.37								
210							2.29		
217	10.20	9.40							
224	10.94	13.49	1.74	2.02	NaN		11.57		NaN
231	16.92	8.93						4.97	
238		9.24		1.64	3.51	8.63	NaN		
245	12.57		NaN						
250	13.16		22.31						4.41
252				9.64	15.34	1.32			
259	7.83	4.25							
260	18.03		38.49					3.16	5.97
266	53.29								
273					85.02	2.59			
280				38.31				1.46	
287						3.30			

NaN - the CV computation did not yield any result

Table 5.6: Conduction velocity values (in cm/s) in the nine investigated subjects. The values for each day of recording represent the maximum velocity that occurred in all quadrant pairs.

The two-tailed bivariate correlation analysis performed at the level of the entire group revealed a positive significant relationship between CV and gestational age, $p < 0.05$, $r = 0.348$, that is, an increase in the CV can be observed with the advancement of the pregnancy.

The grand-averaged CV and estimated delay across subjects indicates a signal propagation speed of 11.98 cm/s and an average delay of 4.57s.

GA [days]	Estimated delay values [seconds]								
	Subject								
	L001	L002	I021	I022	I023	I029	I035	I012	I028
161	2.38								
168	4.06								
175	2.31								
182	4.16								
196	3.72						7.84		
203	4.64								
210							8.84		
217	1.41	5.79							
224	2.98	7.29	6.91	1.09	NaN		1.72		NaN
231	5.42	6.39						4.81	
238		6.45		8.50	3.69	4.98	NaN		
245	4.43		NaN						
250	5.63		0.72						4.53
252				2.00	3.83	13.06			
259	5.67	5.58							
260	3.67		0.38					5.41	3.38
266	3.06								
273					0.06	4.25			
280				0.59				7.25	
287						4.99			

NaN - the computation of the delay did not yield any result

Table 5.7: Estimated delay values (in seconds) for the nine investigated subjects.

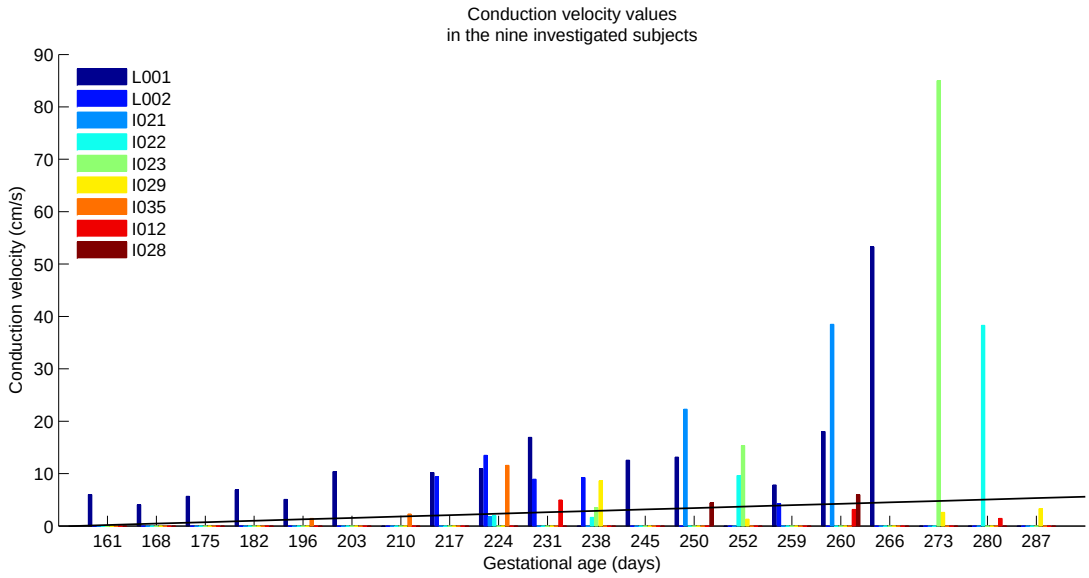

Figure 5.8: Conduction velocity values in the nine investigated subjects. The values for each day of recording represent the maximum velocity that occurred in all quadrant pairs. Black thick line shows the average trend in the analyzed data.

6

Discussion

The quantitative assessment of the uterine contractile activity throughout pregnancy can have an important role in the timely identification of complications and preterm labor. The detection of acute risks along with a more accurate prediction of preterm delivery would allow timely medical intervention and consequently would improve the effectiveness of the required treatments.

The current state-of-the-art in labor monitoring employed in the clinical practice is either inaccurate or has an invasive nature. Present uterine monitors, such as tocography (TOCO), are uncomfortable, less accurate and depend on the examiner for proper placement (Arulkumaran et al., 1991; Iams, 2003; Peaceman et al., 1997). Similarly, the predictive power of biomarkers is not sufficient for a successful diagnostic and the use of Bishop scoring has not lead to a reduction in preterm labor either (Garfield and Maner, 2007). While the evaluation of cervical change is probably the most frequently used clinical method for assessing labor, there is still a high amount of controversy regarding its prognostic value. However, contractions are routinely monitored in the last stage of pregnancy and during labor. The intrauterine pressure catheter (IUPC), the current golden standard for contraction monitoring, provides the most accurate quantitative assessment of the uterine contractions but with limited usability due to its invasive nature (rupture of the amniotic membranes) (Rabotti, 2010). Therefore the use of the IUPC is generally limited to patients in whom delivery is necessary or it presents complications.

The uterine magnetic activity which reflects the original process of muscle fiber excitation due to the propagation of the action potentials (AP) can be non-invasively measured by means of magnetomyography (MMG). Therefore, the magnetomyographic signal has great potential for uterine contraction monitoring both during pregnancy (for

the prediction of preterm labor) and during delivery (for the detection of complications).

6.1 Contraction identification

From a cellular level, the uterine contractions are results of the transmission of action potentials in the myometrial cells of the uterine muscle. This electrical activity is transmitted to the different regions of the uterus through the coupling of the myometrial cells by means of gap junctions. It has been postulated by Garfield and colleagues that the gap junction increases during the labor in various species (Garfield et al., 1977). Further, spectral analysis of EMG shows an increase in power around 0.7 - 0.8 Hz for subjects in labor compared to the non-laboring subjects (Garfield et al., 2005). A global synchronization of the electrical activity over the entire uterus has been related to successful progress of labor and delivery of the fetus. In the past, uterine contractile activity has been successfully measured by means of MMG (Eswaran et al., 2002). However, to further understand the uterine dynamics and to identify the contractions (bursts) in the MMG signals a more sophisticated method would be required. As uterine contraction is not a continuous process, to correctly understand the uterine dynamics, the spectral analysis has to be done exactly in the time window where the contraction has occurred. This is a tedious process as one has to manually score the contraction patterns prior to the application of the spectral analysis. Instead, a time-frequency approach to localize the contractile patterns is attempted in this work using Hilbert and wavelet transforms.

Based on the approach introduced in chapter 3 the MMG power is classified into signal and noise components by using the affinity propagation clustering technique. However, the definition of noise level is ill defined in the MMG data. Hence, based on the SNR obtained by processing the MMG using the algorithm, a stochastic model is proposed to understand the performance of the approach. The data simulated using the model was processed in the same manner as performed for the real MMG data and the SNR was computed. To this end an appropriate threshold was chosen to identify the contractions incorporated in the model. In this procedure, the threshold has been chosen to operate highly specific to identify the true contractile events in the model. Based on this simulation, it can be observed that the threshold used to identify the contraction, decays exponentially with the SNR. To quantify this behavior an exponential model was fitted and it's parameters were identified. This model was then used to compute the threshold for the SNRs obtained for the MMG datasets. It was shown that the proposed method is able to accurately identify the beginning and the end of the contractile burst

activity (see Figure 5.2).

This thesis presents a novel time-frequency approach, based on the Hilbert transform of the wavelet decomposition (HTWD), to identify the contractile burst in MMG signals. In order to aid the approach in distinguishing MMG burst patterns from noise, a stochastic model was introduced. The threshold derived based on the model is used to delineate contractile bursts from the background activity.
This is the first step in the analysis process of making this technique a clinically viable tool. Once the events have been accurately identified one can further process the burst duration, or number of bursts per minute, or the frequency content of the burst and spatial-temporal spread of the burst across the sensor space. Using spectral analysis Garfield and colleagues have shown that the power spectral density (PSD) of uterine EMG bursts in patients during active labor peaked at $0.71 \pm 0.05\ Hz$ as compared to non laboring term ($0.48 \pm 0.03\ Hz$) patients (Garfield et al., 2005). Also, the PSD peak values were comparatively low for patients not in labor with respect to patients in active labor. Further the number of burst per minute and spread of the burst across the sensors will increase as the pregnant mother approaches active labor. All these factors in a certain combination can be potential indicators for the clinical diagnosis of labor. The proposed method provides an accurate temporal evaluation of the occurrence of contractile activity.
In a recent study, Hill and colleagues used recursive partitioning to identify gestational age specific and threshold values for infectious and endocrine biomarkers to predict preterm delivery (Hill et al., 2008). The results indicate that, according to gestational age, two biomarkers provide high accuracy in predicting preterm delivery within 48 hours. These are the corticotropin releasing hormone (CRH) and white blood-cell count (WBC). However, most potential biomarkers of preterm birth investigated in women with threatened preterm labor are similar, with respect to diagnostic performance and accuracy. That is, negative predictive values are superior to positive predictive values and the tests are usually more specific than sensitive (Berghella et al., 2008; Hill et al., 2008; McGregor et al., 1995). Therefore, to predict preterm labor with the current approach and thus to achieve a practical use in the clinical setting, future studies should also concentrate on correlation analysis between MMG outcomes of contractile activity and bio-physiological measures.

6.1.1 Contraction burst identification in serial MMG data

The current work shows that the uterine myometrial burst activity can be successfully identified using the HTWD approach. Statistical analysis carried out on the data collected from subject L001 shows a significant decrement in the mean burst duration (BD) as the subject reaches advanced gestational age (38^{th} week of gestation). The other measures, that is, the standard deviation of the burst duration ($std(BD)$) and in the median BD also displayed a significant decrement with respect to the progression of the pregnancy. Similar behavior was observed in the MMG signals collected from four other participants, namely subject L002, I012, I021 and I023.

An earlier EMG study carried out on a larger population also showed that the mean BD can be used as a parameter that discriminates between preterm contractions that lead to preterm delivery and those that do not, at 2.5 to 4 weeks before delivery (Leman et al., 1999).

The results obtained in the current work are in agreement with earlier findings of Maner and colleagues who also used the standard deviation of the BD in combination with neural networks with good results in terms of sensitivity and negative predictive value (Maner and Garfield, 2007). The authors observed a decrease in the standard deviation of the BD of EMG signals with the progression of pregnancy, in other words, the duration of a contraction is more stable in advanced gestation and during labor. The results of Maner and colleagues as well as the outcomes of the current work are in agreement with observed physiology, as contractions should be more coordinated and synchronous during the labor that precedes delivery (Demianczuk et al., 1984; Eswaran et al., 2004; Garfield and Maner, 2007). However, due to the low energy of the signal, contractions are more difficult to detect in the early gestation than in later pregnancy or during labor. As a consequence, the accuracy of BD detection can be hindered, thus affecting their interpretation. Therefore, the greater variability of BD found in early gestation might be related to inaccurate assessment of the duration itself (which can be highly influenced by the low signal to noise ratio).

One of the most investigated parameters with respect to the timely prediction of delivery is the PSD. The shift of the burst frequency components from low frequencies, during pregnancy, to higher frequencies, during labor, is one of the most significant and one of the earliest observable characteristics (Doret et al., 2005; Garfield and Maner, 2007; Vinken et al., 2009). EMG studies carried out on both humans and animals show shifting of the EMG signal power to higher frequencies as subjects approach delivery. Similar spectral changes, as delivery approaches in both term and preterm deliveries,

were observed in both EMG and MMG studies (Eswaran et al., 2009; Garfield et al., 2005; Vinken et al., 2009).

An explanation of the shift is provided by the underlying physiology: the frequency of APs within one burst is a direct measure of the rate of the depolarization/repolarization process (largely governed by Ca^{2+} influx across ion channels) in the myometrial cells (Sanborn, 2000). The uterus becomes more excitable and the signal propagation distance and contraction strength increase when the modifications in the myometrial cell's plasma membrane ion channel initiate labor (Vinken et al., 2009), thus, resulting in higher frequency cycles within bursts of activity (Maner and Garfield, 2007; Maner et al., 2003).

The current work has shown that the proposed method, besides the identification of instances wherein contraction bursts occur, is also suited to keep track of the shift of burst frequency components. However, this could be shown in only one subject due to the lack of available longitudinal recordings. Future clinical studies should validate the predictive capabilities of the proposed approach (and PSD shift) on a larger population.

6.2 Conduction velocity

Currently there is a lack of studies which address the issue of signal conduction velocity in MMG multisensor recordings. However, few dedicated studies exist which investigate the EMG signal conduction properties by multichannel recordings (Euliano et al., 2009; Rabotti et al., 2010b, 2009, 2011). These studies investigated the conduction on a large scale by analyzing the EMG bursts on the whole uterine muscle. A similar approach has also been attempted by multichannel tocography (Spaetling et al., 1997).
A recent study has shown a better performance in predicting the preterm labor using the conduction velocity in combination with the peak frequency compared to the standard clinical methods such as Bishop score, contractions, and cervical length (Lucovnik et al., 2011a).
In a previous study (Fele-Zorz et al., 2008) the authors investigated several linear and non-linear signal processing methods on groups of term and pre-term delivery records recorded before and after the 26^{th} week of gestation. The authors emphasize that their goal was not to predict the beginning of labor nor following the changes in spectra prior to delivery but to differentiate these groups early during the pregnancy. The authors conclude that when using a 0.3 - 3 Hz filter two methods (i) the median frequency of the power spectrum and (ii) the sample entropy provide best discrimination for the investigated groups. For their term recordings the authors observe a slight decrease in the median frequency of the power spectrum as time of gestation progresses, while other studies show an increase in the power spectra distribution (Maner et al., 2003, 2006). The decrease is later explained by the difference in the processing of the recorded data. Fele-Zorz and colleagues processed entire records, the entire electrical activity of the uterus, while in those other studies individual contractile events, i.e., the bursts associated to contractions, were processed. The authors also conclude, that if entire records are processed and records are taken more than seven weeks prior to delivery, a slight decrease of the power spectra distribution is observed for term records.
As both uterine contractile activity and artifacts due to subject movement are low frequency processes, contamination of the myometrial activity by movement artefacts might occur, thus hindering the interpretation of the result. Therefore, in the context of CV analysis, the detection of movement artifacts is necessary to avoid the possible interference of the two processes.
This thesis was able to show that the conduction velocity is positively correlated with the gestational age. The two-tailed bivariate correlation analysis carried out on the pooled data revealed a significant positive relationship between the two measures,

$p < 0.05$, $r = 0.348$. Therefore, it is safe to assume that, at the level of the entire group, this correlation can be attributed to the gradual increase in the gap junction between the myometrial cells during pregnancy. Indeed, subject L001 delivered within two weeks from the last study. In some of the remaining subjects, descriptive statistics (due to insufficient amount of available data) show an increase of CV with the increase of GA as well. These are subjects I021, I022, I023, I035 and I028. In all other participants, no clear trend is seen between conduction velocity and gestational age, which could be either due to (i) an insufficient amount of available recordings or to (ii) no significant change in the uterine dynamics at the time of the measurement. Subject L002 delivered within four days from the last study but by C-section mode. In addition, the computation of the average CV led to a value of 11.98 cm/s which is within the expected physiological range. Various estimates of the CV in the human uterus during labour are in the same range as the estimate values reported for different animal species: 1 - 6 cm/s for the pregnant rabbit uterus, 6 - 12 cm/s for the pregnant cat uterus and 4 - 9.6 cm/s for the pregnant rat uterus (Wolfs and Leeuwen, 1979). Miller and colleagues reported CV values in rats which ranged between 7.9 ± 3.0 cm/s and 13.5 ± 4.2 cm/s at preterm and during delivery (Miller et al., 1989). In future work this should be investigated on a larger population, i.e., on preterm and term subjects, and compare CV with the traditionally used clinical measures in predicting the term/preterm labor.

To conclude, the results show that the proposed method is suitable for the three dimensional estimation of the MMG surface AP conduction velocity. Additionaly, the proposed method can be employed for the analysis of other types of signal, in particular, when the direction of propagation is *a priori* unknown.

6.3 Conclusions and future directions

This thesis provides sustained evidence that, in multi sensor MMG recordings, the proposed method is able to reliably capture patterns of activation that are characteristic of uterine contractile activity. In addition, it has been also shown that the relative strength of the MMG burst frequency components increased from early gestational age (as early as 23^{rd} week of gestation) as compared to recordings of advanced gestational age (close to term). Similar behavior was observed in patients in active labor (cervical dilatation $\geqslant 3\ cm$) as compared to patients with contractions in non-active labor (both term and preterm) (Eswaran et al., 2009, 2004). These findings are inline with those reported in several EMG studies, that is, the shift of the burst frequency components (from lower towards higher frequencies) represent the earliest and most significant variation in term and preterm delivery (Doret et al., 2005; Garfield et al., 2005; Vinken et al., 2009). However, despite these observations, a proper frequency threshold for an accurate contraction discrimination and delivery prediction could not be determined. Future MMG studies should investigate, in a large population, the presence of such threshold.
The development of the proposed method for MMG conduction analysis followed according to knowledge of the physiological background and was specifically tailored to the analysis of spatial temporal MMG signals. Nevertheless, the methods proposed in the current work can be applied to other applications related to the detection of propagating electrophysiological signals, provided the presence of an invariant distance between recording sites.
Due to the limited amount of analyzed data, further clinical validations are required to assess the robustness of the method and also to account for physiological differences among subjects. Such validations are of particular importance for the perspective of introducing the proposed methods in the daily clinical practice.

The current work provides a quantitative characterization of the uterine activity during pregnancy and delivery. The methods proposed for the analysis of the MMG signals provide an accurate characterization of the uterine contractile activity, which in turn, can result in a better interpretation of parameters with clinical relevance. Therefore, with regard to the medical challenges faced by obstetricians and the inconveniences presented by the current monitoring and assessment methods, the current work creates new perspectives for clinical applications and studies. A thorough understanding of the processes underlying the onset of labor will advance obstetrical monitoring technologies

and will not only reduce the incidence of preterm birth but will also improve the perinatal outcome.

Previous studies highlighted the potential prognostic and diagnostic value of EMG signal analysis and investigated the possibility of accurately estimating the intra uterine pressure from noninvasive EMG recordings (Rabotti et al., 2008). Also, important issues like the effect of the tissues interposed between the uterus and the skin (volume conductor) on EMG recordings have been recently studied (Rabotti et al., 2010a). However, when compared to MMG recordings, EMG signal interpretation has been typically based on measurements wherein information is conveyed from a relative small area. The use of a magnetic sensor array that can cover a much larger area has the potential to convey additional (better) information with respect to the estimation of intra uterine pressure or the distribution and dynamics of the electrical activation and can ultimately lead to a better prediction of delivery.

The concept of pacemaker cells in the myometrium has been considered by many and it has engaged several research groups. It has been suggested that the uterus is myogenic in that it can contract without the need of external stimuli. In addition, any myometrial cell is capable of acting either as a pacemaker or pace-follower (Kao, 1959). However, studies using a variety of histological techniques failed to provide clear evidence for the presence of cells with the histological and electrophysiological properties of a functional pacemaker. Perhaps the concept of pacemaker cells, along with the conduction direction, needs to be revised, with targeted and extensive studies which investigate the fundus *vs.* isthmus regions of the uterus, looking for regional differences (e.g., gap junction density) or for preferred propagation pathways. Hormonal or protein concentration differences in the different regions of the uterus may be also held responsible for the onset of the signal propagation in late gestation (Kumar and Barnes, 1961). Therefore it would be of a great advantage if future studies will take into account and combine the knowledge gained from histological and electrophysiological outcomes. For such purpose, the SARA system represents an ideal candidate, as the arrangement of the magnetic sensors permits to investigate all the possible CV directions along the abdominal plane by conveying accurate information from a relatively large surface (approximately $1,400\ cm^2$).

The method presented for the estimation of CV can be further improved by the fine tuning or the regularization of some of the processing parameters, e.g., the maximum lag allowed for the computation of HDCC, maximum distance between sensors over which the CV can be computed.

Another important aspect which needs to be mentioned is that the MMG signal, which

is characteristic for the uterine contractile activity, can also originate and propagate from the dorsal part of the uterus and thus cannot be directly monitored. Therefore, future work could also focus on the computation of uterine activation maps which are related to pacemaker regions situated on the dorsal side of the uterus.

Smooth muscle fibre CV represents an important physiological parameter because it reflects the membrane muscle fibre properties and thus the modifications of the peripheral properties of the neuromuscular system as a consequence of pathology, fatigue or exercise (Farina and Merletti, 2004). Therefore, the assessment of the CV might have a major clinical relevance as it could facilitate an objective quantification of the labor's progression and provide, in the same time, an accurate separation of a normal, physiological development of labor from a pathological one.
However, the underlying physiological mechanism of the uterine contraction is only partially understood and it is believed that substantial increase in the knowledge of this field could be gained by improving the computational and analysis techniques available for the SARA recording system. This advancement could lead to the establishment of this technology as a clinical tool by providing the linkage between the electrophysiology of the uterine contractions and the data acquired using the SARA system.

Appendices

Appendix A

A.1 Organization and labeling of the magnetic sensors

The magnetic sensor arrangement of the SARA I and SARA II systems is depicted in Figure A.1. In both systems the sensors are organized in nearly straight rows (in x-y projection) with labels roughly corresponding to the geometrical sensor positionLowery et al. (2006); Robinson et al. (2001). The prefixes L, R indicate the sensors on the left and right side of the mother (front view), respectively. The prefix C indicates the sensors on the center line (maternal body axis). Row A is in the perineal region and row Q is at the top of the maternal abdomen.

A.2 Analysis tool for the uterine contraction

In an effort to make the contraction analysis tools available to the medical personnel, a graphical user interface (GUI) has been created. A snapshot of the uterine contraction analysis tool is provided in figure A.2. The GUI is subdivided in four panels. The top left panel contains the editing windows and buttons which allow the modification of the parameters needed for the computation of the contraction marker, (i.e., band pass filter cutoff, downsampling frequency, inspection window size, notch filter cutoff and the sensitivity of the algorithm).
The top right panel groups the editing windows and button which are necessary for the computation of the conduction velocity, (i.e., number of quadrants, maximum lag for the HDCC and the interval to be discarded from the velocity analysis - to avoid *divide by zero* errors). The bottom panels provide information regarding the loaded dataset(s) (bottom left) and information regarding the status of the analysis (bottom right).
At start up, the edit boxes of the graphical user interface are filled with default values,

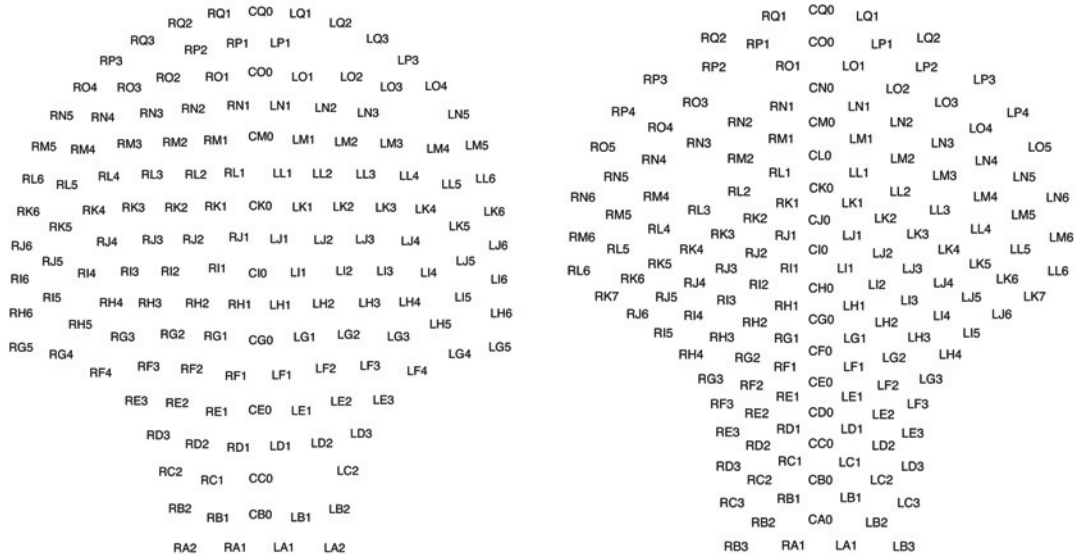

Figure A.1: Organization and labeling of the magnetic sensors. Left: front view of the SARA I sensor layout, installed at the University of Arkansas for Medical Sciences, Little Rock, USA. Right: the layout of the SARA II system, installed at the University of Tübingen, Germany.

which can be further customized by the user.

The user has the possibility to load the MMG signals either from Matlab binary files (multiple selection of *.mat* files is also possible) or from a *ctf* directory (only one *.ds* directory can be opened at a time).

Once the required variables are found and successfully loaded, the *Contraction marker* button becomes active allowing the analysis of the loaded data. During the analysis the operations presented in Figure 4.5 are performed. After the analysis has completed, the variables are saved to a .mat file which can be further used for the computation of the conduction velocity.

Pressing the *Conduction velocity* button allows the computation of the conduction velocity which follows the steps presented in Figure 2.3. In addition, instead of the standard sensor partitioning (corresponding to quadrants) the user can provide customized sensor partitioning schemes, which would allow the analysis of a different amount of quadrants.

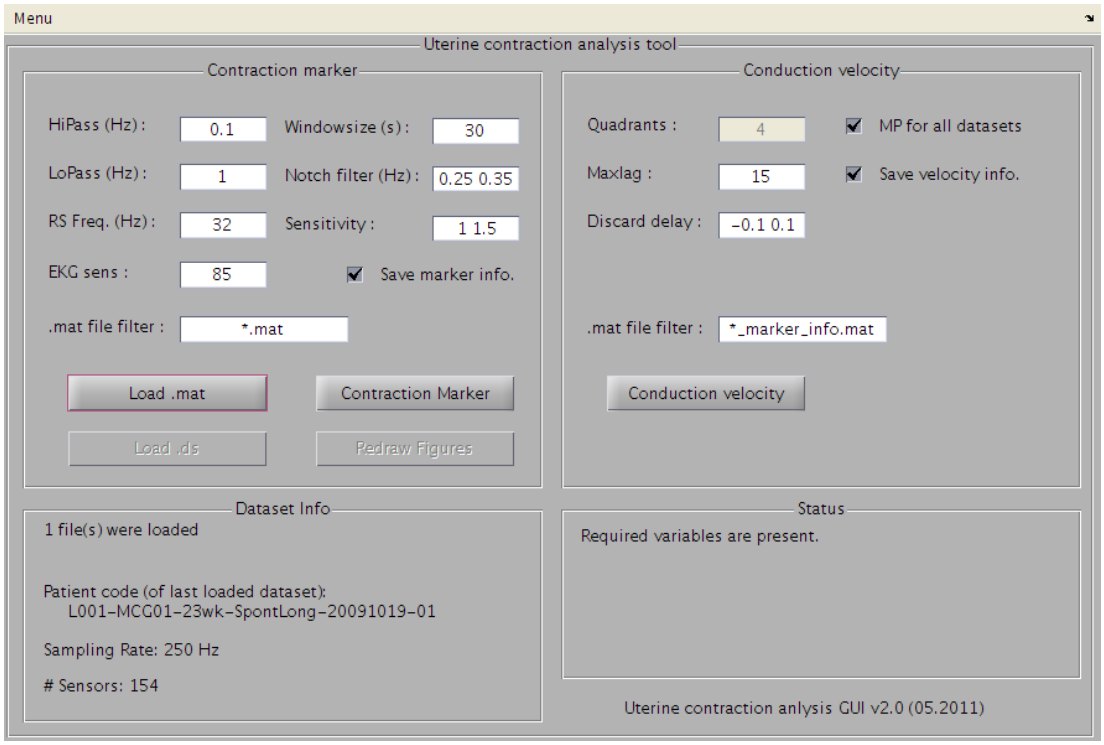

Figure A.2: The user interface of the analysis tool.

Appendix B

B.1 Additionally investigated methods

Prior to the HTWD approach, two additional methods were considered as possible candidates for the identification of the uterine contractile activity. These were the short-time Fourier transform (STFT) and the root mean square (RMS). The application of these methods on MMG signals is described in the following subsections.

B.1.1 Short-time Fourier transform

The short-time Fourier transform (STFT) was also investigated as an alternative to perform time-frequency analysis on the MMG signals. For a given signal $x(t)$ the STFT can be used to determine the sinusoidal frequency and phase content of local sections of $x(t)$. In the continuous-time case, the function to be transformed is multiplied by a window function which is nonzero for only a short period of time. The Fourier transform of the resulting signal is taken as the window is slid along the time axis, resulting in a two-dimensional representation of the signal.
Mathematically, this can be expressed as:

$$x(t) = \int_{-\infty}^{\infty} x(t)w(t-\tau)e^{-j\omega t}dt \tag{B.1}$$

where $w(t)$ represents the window function and $x(t)$ the signal that is transformed.
The STFT is more similar to the wavelet transform, in that it is also time and frequency localized, but there are issues with the frequency/time resolution trade-off. Wavelets often give a better signal representation with balanced resolution at any time and frequency. Compared to the discrete wavelet transform STFT is also computationally more complex.
The STFT employs spectral estimation procedure. To capture the low-frequency

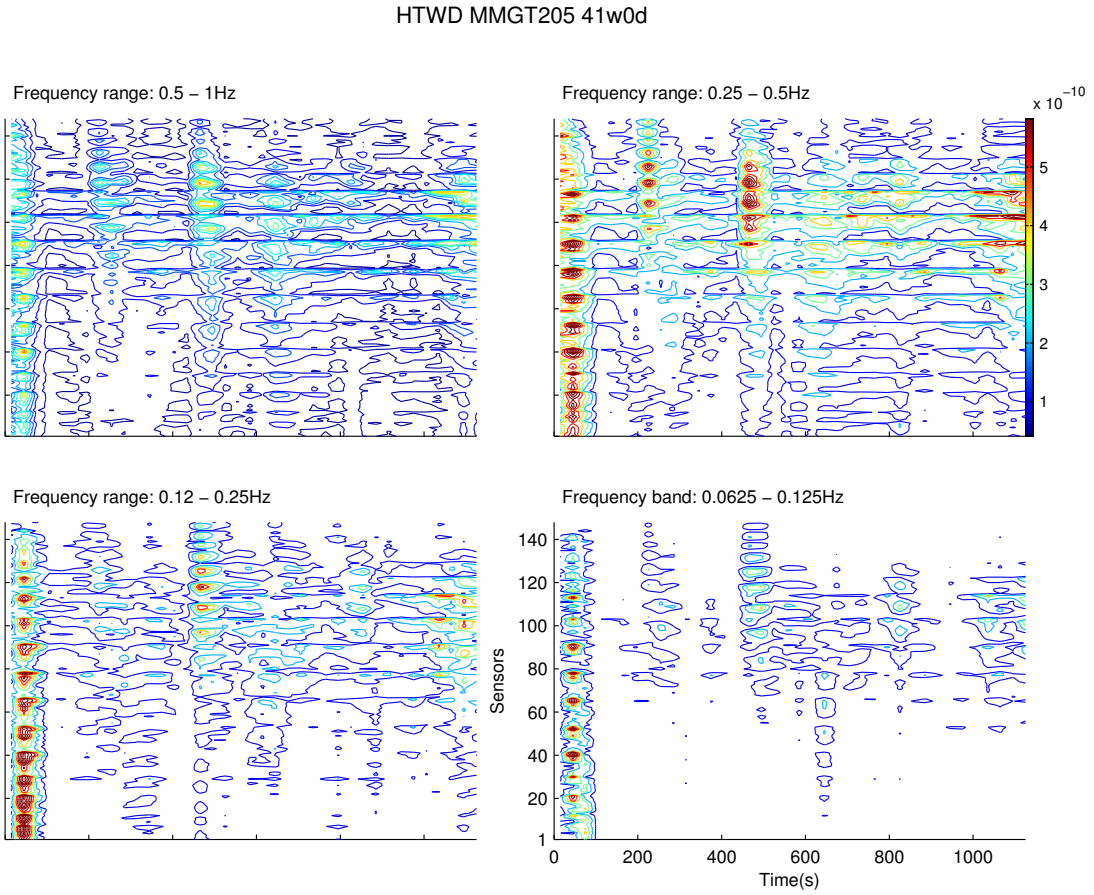

Figure B.1: HTWD processing of MMG data for the MMGt205 40w1d dataset. The figure shows the contour map of the mean HTWD computed in 30s non-overlapping windows in four different frequency bands (0.0625 - 1 Hz range).

contraction burst in a 30 s window, one has to use a Fast Fourier Transform (FFT) length of at least 10 s to get a frequency resolution of 0.1 Hz. On the other hand, if one decides to use a longer FFT window, one will get a good estimation of the spectrum but will not get the desired frequency range of 0.1Hz. Thus, if high frequency resolution is desired, one will have to compromise for the reliability in the estimation. Hence, the use of this technique may not allow to correctly characterize the spectral properties of the signals. Figures B.1 and B.2 show the contour maps obtained after applying both methods (HTWD and STFT) to a selected dataset. To obtain the same frequency resolution in STFT as in HTWD the spectrum was estimated in a 60 s window. As discussed above, this results in a good frequency resolution but a poor estimation of the

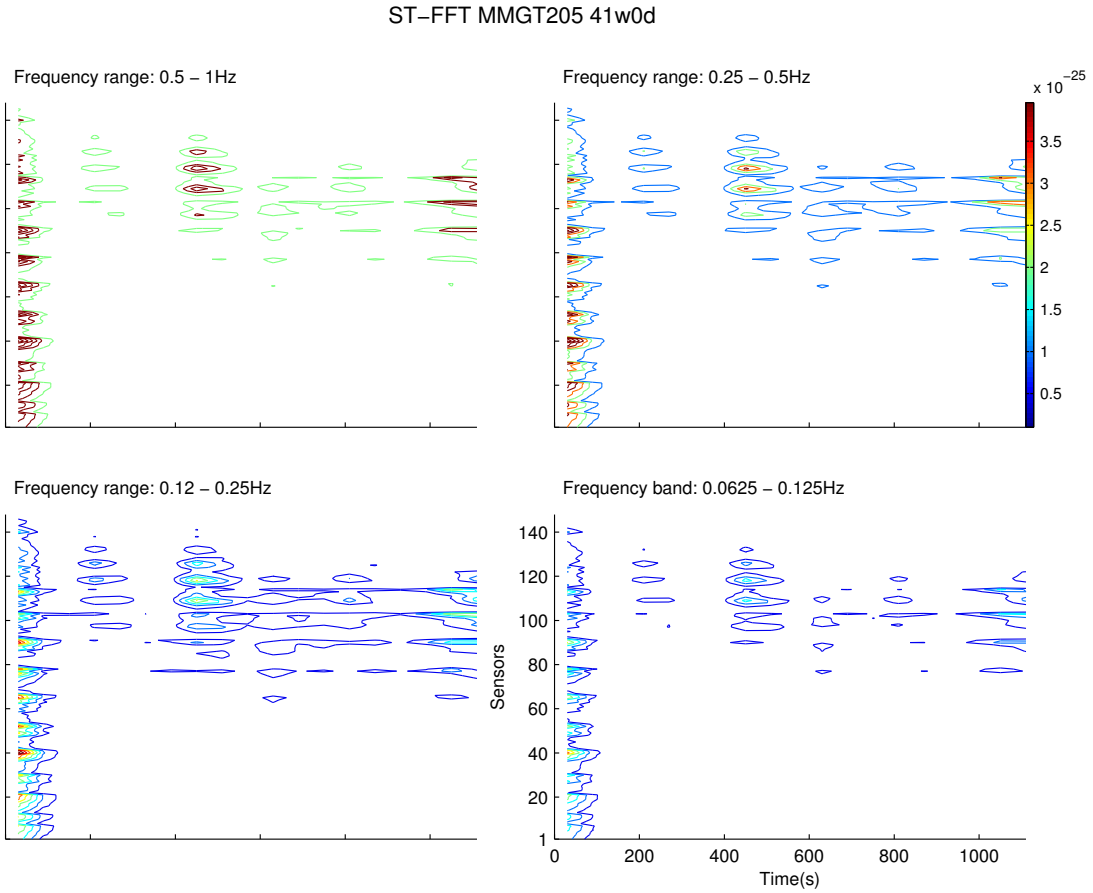

Figure B.2: STFT processing of MMG data for an exemplary dataset MMGt205 40w1d. The figure shows the contour map of the mean STFT computed in 60 s non-overlapping windows in four different frequency bands (0.0625 - 1 Hz range). To obtain the same frequency resolution the STFT window was set twice the length of the HTWD window.

spectrum. Figure B.2 shows spuriously higher power in the 0.5 - 1 Hz. This may be due to the residual power because of improper truncation of bandpass filtering. However, the HTWD is able to correctly localize the power (0.25 - 0.5 Hz band) and therefore the STFT approach was not further explored.

B.1.2 Root mean square

The root mean square (RMS) or the quadratic mean is a statistical measure of a varying quantity. For a continuous signal $x(t)$ defined over an interval $T_1 \leq t \leq T_2$ the RMS

can be computed as follows (Cartwright, 2007):

$$x_{RMS} = \sqrt{\frac{1}{T_2 - T_1} \int_{T_1}^{T_2} [f(t)]^2 dt} \tag{B.2}$$

In the context of the current work the computation of RMS of the signal was also considered. The procedure is equivalent to quantifying the power of the signal in the time domain. However, this method proved to be inadequate for the purpose of the current work because the frequency of the uterine contraction varies dynamically. Such behavior has been observed in (Garfield et al., 2005) and (Eswaran et al., 2009). This dynamic variation cannot be reliably captured by studying the integral plot of the squared MMG signal.
Furthermore, the integral part of the squared signal provides the global power of the signal and hence it is not possible to understand from which frequency component the power came. This represents a strong reason for not to choose the RMS approach.

Glossary

ADP	adenosine diphosphate, the product of adenosine triphosphate dephosphorylation.
AP	action potential.
APC	affinity propagation clustering.
AR	autoregressive model.
AR2	second order autoregressive model.
ATP	adenosine triphosphate, a multifunctional nucleoside triphosphate used in cells as a coenzyme.
BD	burst duration.
BF	burst frequency.
chorion	one of the membranes that exist during pregnancy between the developing fetus and mother.
CoG	center of gravity.
CRH	corticotropin releasing hormone.
C-section	a surgical procedure in which one or more incisions are made through a mother's abdomen and uterus to deliver the baby.
CV	conduction velocity.
db2	Daubechies second-order discrete wavelet.
decidua	term used for the endometrium during pregnancy.
dephosphorylation	the removal of a phosphate group from a protein.
dewar	a special insulating storage vessel meant to keep its contents cooler than its surroundings.

EHG	electrohysterography/electrohysterogram.
EMG	electromyography/electromyogram.
fFN	fetal fibronectin.
FFT	fast Fourier transform.
fMCG	fetal magnetocardiography/magnetocardiogram.
fMEG	fetal magnetoencephalography/magnetoencephalogram.
FOZC	first-order zero-crossing.
fundus	the top portion of the uterus, opposite from the cervix.
GA	gestational age.
gap junction	a specialized intercellular connection between a multitude of cell types.
GUI	graphical user interface.
HDCC	high dimension cross correlation.
HT	Hilbert transform.
HTWD	Hilbert transform of the wavelet decomposition.
isthmus	the inferior-posterior part of uterus, on its cervical end.
IUGR	intrauterine growth restriction, refers to the poor growth of a fetus.
IUP	intrauterine pressure.
IUPC	intrauterine pressure catheter.
MLCK	myosin light-chain kinase.
mMCG	maternal magnetocardiography/magnetocardiogram.
MMG	magnetomyography/magnetomyogram.
NAS	number of active sensors.

phosphorylation	the addition of a phosphate group to a protein.
PKC	proteine kinase C, a family of protein kinase enzymes involved in controlling the function of other proteins through the phosphorylation.
PSD	power spectral density.
RMS	root mean square.
SARA	SQUID array for reproductive assessment.
SIC	Schwarz information criterion.
SNR	signal to noise ratio.
SQUID	super quantum interference device.
std	standard deviation.
STFT	short-time Fourier transform.
syncytium	a multinucleate cell which can result from multiple cell fusions of uninuclear cells.
TOCO	tocography, technical means of recording the uterine contractions.
tr(X)	trace of matrix X.
var	variance.
WBC	white blood-cell count.

References

Aguilar, H. N., Xiao, S., Knoll, A. H., and Yuan, X. (2010). Physiological pathways and molecular mechanisms regulating uterine contractility. *Human Reproduction Update*, 16(6):725.

Anderson, N C, J. (1969). Voltage-clamp studies on uterine smooth muscle. *The Journal of General Physiology*, 54(2):145–165. PMID: 5796366.

Arulkumaran, S., Yang, M., Tien, C. Y., and Ratnam, S. S. (1991). Reliability of intrauterine pressure measurements. *Obstetrics and Gynecology*, 78(5 Pt 1):800–802. PMID: 1923200.

Baumgartner, C. (1995). *Biomagnetism: fundamental research and clinical applications. Proceedings of the 9th International Conference on Biomagnetism.* IOS Press.

Berghella, V., Hayes, E., Visintine, J., and Baxter, J. K. (2008). Fetal fibronectin testing for reducing the risk of preterm birth. *Cochrane Database of Systematic Reviews (Online)*, 1(4):CD006843. PMID: 18843732.

Bishop, E. H. (1964). Pelvic scoring for elective induction. *Obstetrics and Gynecology*, 24:266–268. PMID: 14199536.

Bode, O. (1931). Das elektrohysterogramm. *Archiv für Gynäkologie*, 146(1):123–128.

Bozler, E. (1948). Conduction, automaticity, and tonus of visceral muscles. *Experientia*, 4(6):213–218. PMID: 18869660.

Buhimschi, C., Boyle, M. B., and Garfield, R. E. (1997). Electrical activity of the human uterus during pregnancy as recorded from the abdominal surface. *Obstetrics and Gynecology*, 90(1):102–111. PMID: 9207823.

Buhimschi, C., Boyle, M. B., Saade, G. R., and Garfield, R. E. (1998). Uterine activity during pregnancy and labor assessed by simultaneous recordings from the myometrium and abdominal surface in the rat. *American Journal of Obstetrics and Gynecology*, 178(4):811–822. PMID: 9579450.

Buhimschi, C. and Garfield, R. E. (1996). Uterine contractility as assessed by abdominal surface recording of electromyographic activity in rats during pregnancy. *American Journal of Obstetrics and Gynecology*, 174(2):744–753. PMID: 8623816.

Buhimschi, C. S., Buhimschi, I. A., Malinow, A. M., Saade, G. R., Garfield, R. E., and Weiner, C. P. (2003). The forces of labour. *Fetal and Maternal Medicine Review*, 14(04):273–307.

Cartwright, K. V. (2007). Determining the effective or RMS voltage of various waveforms without calculus. *Technology Interface*, 8(1):20 pages.

Chard, T. (1994). *The uterus*. Cambridge University Press.

Cox, S. M., Sherman, M. L., and Leveno, K. J. (1990). Randomized investigation of magnesium sulfate for prevention of preterm birth. *American Journal of Obstetrics and Gynecology*, 163(3):767–772. PMID: 2206069.

Csapo, A. (1954). Dependence of isometric tension and isotonic shortening of uterine muscle on temperature and on strength of stimulation. *The American Journal of Physiology*, 177(3):348–354. PMID: 13158573.

Csapo, A. and Goodall, M. (1954). Excitability, length tension relation and kinetics of uterine muscle contraction in relation to hormonal status. *The Journal of Physiology*, 126(2):384–395. PMID: 13222291.

Demianczuk, N., Towell, M. E., and Garfield, R. E. (1984). Myometrial electrophysiologic activity and gap junctions in the pregnant rabbit. *American Journal of Obstetrics and Gynecology*, 149(5):485–491. PMID: 6742016.

Devedeux, D., Marque, C., Mansour, S., Germain, G., and Duchne, J. (1993). Uterine electromyography: a critical review. *American Journal of Obstetrics and Gynecology*, 169(6):1636–1653. PMID: 8267082.

Doret, M., Bukowski, R., Longo, M., Maul, H., Maner, W. L., Garfield, R. E., and Saade, G. R. (2005). Uterine electromyography characteristics for early diagnosis of mifepristone-induced preterm labor. *Obstetrics and Gynecology*, 105(4):822–830. PMID: 15802412.

Duchene, J., Marque, C., and Planque, S. (1990). Uterine EMG signal : Propagation analysis. In *, Proceedings of the Twelfth Annual International Conference of the IEEE Engineering in Medicine and Biology Society, 1990*, pages 831–832. IEEE.

Duthie, H. L. (1974). Electrical activity of gastrointestinal smooth muscle. *Gut*, 15(8):669–681. PMID: 4371683.

Eswaran, H., Govindan, R. B., Furdea, A., Murphy, P., Lowery, C. L., and Preissl, H. (2009). Extraction, quantification and characterization of uterine magnetomyographic activity–a proof of concept case study. *European Journal of Obstetrics, Gynecology, and Reproductive Biology*, 144 Suppl 1:S96–100. PMID: 19303190.

Eswaran, H., Preissl, H., Wilson, J. D., Murphy, P., and Lowery, C. L. (2004). Prediction of labor in term and preterm pregnancies using non-invasive magnetomyographic recordings of uterine contractions. *American Journal of Obstetrics and Gynecology*, 190(6):1598–1602; discussion 1602–1603. PMID: 15284746.

Eswaran, H., Preissl, H., Wilson, J. D., Murphy, P., Robinson, S. E., and Lowery, C. L. (2002). First magnetomyographic recordings of uterine activity with spatial-temporal information with a 151-channel sensor array. *American Journal of Obstetrics and Gynecology*, 187(1):145–151. PMID: 12114902.

Euliano, T. Y., Marossero, D., Nguyen, M. T., Euliano, N. R., Principe, J., and Edwards, R. K. (2009). Spatiotemporal electrohysterography patterns in normal and arrested labor. *American Journal of Obstetrics and Gynecology*, 200(1):54.e1–7. PMID: 19121657.

Euro-Peristat Project, S. (2004). European perinatal health report. `http://www.europeristat.com/publications/european-perinatal-health-report.shtml`.

Farina, D. and Merletti, R. (2004). Methods for estimating muscle fibre conduction velocity from surface electromyographic signals. *Medical & Biological Engineering & Computing*, 42(4):432–445.

Fele-Zorz, G., Kavsek, G., Novak-Antolic, Z., and Jager, F. (2008). A comparison of various linear and non-linear signal processing techniques to separate uterine EMG records of term and pre-term delivery groups. *Medical & Biological Engineering & Computing*, 46(9):911–922. PMID: 18437439.

Fischer, E. (1944). Vertebrate smooth muscle. *Physiological Reviews*, 24(4):467–490.

Fonseca, E. B., Celik, E., Parra, M., Singh, M., and Nicolaides, K. H. (2007). Progesterone and the risk of preterm birth among women with a short cervix. *The New England Journal of Medicine*, 357(5):462–469. PMID: 17671254.

Frey, B. J. and Dueck, D. (2007). Clustering by passing messages between data points. *Science (New York, N.Y.)*, 315(5814):972–976. PMID: 17218491.

Furdea, A., Eswaran, H., Wilson, J. D., Preissl, H., Lowery, C. L., and Govindan, R. B. (2009). Magnetomyographic recording and identification of uterine contractions using hilbert-wavelet transforms. *Physiological Measurement*, 30(10):1051–1060. PMID: 19738317, `http://dx.doi.org/10.1088/0967-3334/30/10/006`.

Furdea, A., Preissl, H., Lowery, C. L., Eswaran, H., and Govindan, R. B. (2011). Conduction velocity of the uterine contraction in serial magnetomyogram (MMG) data: Event based simulation and validation. *Conference Proceedings: ... Annual International Conference of the IEEE Engineering in Medicine and Biology Society. IEEE Engineering in Medicine and Biology Society. Conference*, 2011:6025–6028. PMID: 22255713.

Garfield, R. E. (1984). Control of myometrial function in preterm versus term labor. *Clinical Obstetrics and Gynecology*, 27(3):572–591. PMID: 6488606.

Garfield, R. E., Ali, M., Yallampalli, C., and Izumi, H. (1995). Role of gap junctions and nitric oxide in control of myometrial contractility. *Seminars in Perinatology*, 19(1):41–51. PMID: 7754410.

Garfield, R. E., Blennerhassett, M. G., and Miller, S. M. (1988). Control of myometrial contractility: role and regulation of gap junctions. *Oxford Reviews of Reproductive Biology*, 10:436–490. PMID: 3072507.

Garfield, R. E. and Hayashi, R. H. (1981). Appearance of gap junctions in the myometrium of women during labor. *American Journal of Obstetrics and Gynecology*, 140(3):254–260. PMID: 7246625.

Garfield, R. E. and Maner, W. L. (2007). Physiology and electrical activity of uterine contractions. *Seminars in Cell & Developmental Biology*, 18(3):289–295. PMID: 17659954.

Garfield, R. E., Maner, W. L., MacKay, L. B., Schlembach, D., and Saade, G. R. (2005). Comparing uterine electromyography activity of antepartum patients versus term labor patients. *American Journal of Obstetrics and Gynecology*, 193(1):23–29. PMID: 16021054.

Garfield, R. E., Maul, H., Shi, L., Maner, W., Fittkow, C., Olsen, G., and Saade, G. R. (2001). Methods and devices for the management of term and preterm labor. *Annals of the New York Academy of Sciences*, 943:203–224. PMID: 11594541.

Garfield, R. E., Saade, G., Buhimschi, C., Buhimschi, I., Shi, L., Shi, S. Q., and Chwalisz, K. (1998). Control and assessment of the uterus and cervix during pregnancy and labour. *Human Reproduction Update*, 4(5):673695. PMID: 10027621.

Garfield, R. E., Sims, S., and Daniel, E. E. (1977). Gap junctions: their presence and necessity in myometrium during parturition. *Science (New York, N.Y.)*, 198(4320):958–960. PMID: 929182.

Garfield, R. E., Sims, S. M., Kannan, M. S., and Daniel, E. E. (1978). Possible role of gap junctions in activation of myometrium during parturition. *The American Journal of Physiology*, 235(5):C168–179. PMID: 727239.

Gherghiceanu, M. and Popescu, L. M. (2005). Interstitial cajal-like cells (ICLC) in human resting mammary gland stroma. transmission electron microscope (TEM) identification. *Journal of Cellular and Molecular Medicine*, 9(4):893–910. PMID: 16364198.

Goldenberg, R. L., Culhane, J. F., Iams, J. D., and Romero, R. (2008). Epidemiology and causes of preterm birth. *Lancet*, 371(9606):75–84. PMID: 18177778.

Goldenberg, R. L., Goepfert, A. R., and Ramsey, P. S. (2005). Biochemical markers for the prediction of preterm birth. *American Journal of Obstetrics and Gynecology*, 192(5 Suppl):S36–46. PMID: 15891711.

Govindan, R. B., Vairavan, S., Ulusar, U. D., Wilson, J. D., McKelvey, S. S., Preissl, H., and Eswaran, H. (2011). A novel approach to track fetal movement using multi-sensor magnetocardiographic recordings. *Annals of Biomedical Engineering*, 39(3):964–972. PMID: 21140290.

Govindan, R. B., Wilson, J. D., Preissl, H., Murphy, P., Lowery, C. L., and Eswaran, H. (2008). An objective assessment of fetal and neonatal auditory evoked responses. *NeuroImage*, 43(3):521–527. PMID: 18760370.

Guyton, A. C. and Hall, J. E. (2010). *Textbook of Medical Physiology*. Saunders, 12th edition.

Hellemans, P., Gerris, J., and Verdonk, P. (1995). Fetal fibronectin detection for prediction of preterm birth in low risk women. *British Journal of Obstetrics and Gynaecology*, 102(3):207–212. PMID: 7794844.

Hill, J. L., Campbell, M. K., Zou, G. Y., Challis, J. R. G., Reid, G., Chisaka, H., and Bocking, A. D. (2008). Prediction of preterm birth in symptomatic women using decision tree modeling for biomarkers. *American Journal of Obstetrics and Gynecology*, 198(4):468.e17; discussion 468.e7–9. PMID: 18395044.

Hinescu, M. E., Gherghiceanu, M., Mandache, E., Ciontea, S. M., and Popescu, L. M. (2006). Interstitial cajal-like cells (ICLC) in atrial myocardium: ultrastructural and immunohistochemical characterization. *Journal of Cellular and Molecular Medicine*, 10(1):243–257. PMID: 16563237.

Hinescu, M. E. and Popescu, L. M. (2005). Interstitial cajal-like cells (ICLC) in human atrial myocardium. *Journal of Cellular and Molecular Medicine*, 9(4):972–975. PMID: 16364205.

Hussain, M. S., Reaz, M. B. I., MohdYasin, F., and Ibrahimy, M. I. (2009). Electromyography signal analysis using wavelet transform and higher order statistics to determine muscle contraction. *Expert Systems*, 26(1):35–48.

Iams, J. D. (2003). Prediction and early detection of preterm labor. *Obstetrics and Gynecology*, 101(2):402–412. PMID: 12576267.

Kao, C. Y. (1959). Long-term observations of spontaneous electrical activity of the uterine smooth muscle. *The American Journal of Physiology*, 196(2):343–350. PMID: 13627177.

Kenyon, A. P. and Peebles, D. (2011). Myth: tocolysis for prevention of preterm birth has a major role in modern obstetrics. *Seminars in Fetal & Neonatal Medicine*, 16(5):242–246. PMID: 21641289.

Klinke, R., Pape, H.-C., Kurtz, A., and Silbernagl, S. (2009). *Physiologie: Lehrbuch*. Thieme, Stuttgart, 6th edition.

Knowles, J. R. (1980). Enzyme-catalyzed phosphoryl transfer reactions. *Annual Review of Biochemistry*, 49:877–919.

Kumar, D. and Barnes, A. C. (1961). Studies in human myometrium during pregancy. II. resting membrane potential and comparative electrolyte levels. *American Journal of Obstetrics and Gynecology*, 82:736–741. PMID: 14460490.

La Rosa, P. S., Nehorai, A., Eswaran, H., Lowery, C. L., and Preissl, H. (2008). Detection of uterine MMG contractions using a multiple change point estimator and the k-means cluster algorithm. *IEEE Transactions on Bio-Medical Engineering*, 55(2 Pt 1):453–467. PMID: 18269980.

Leman, H., Marque, C., and Gondry, J. (1999). Use of the electrohysterogram signal for characterization of contractions during pregnancy. *IEEE Transactions on Bio-Medical Engineering*, 46(10):1222–1229. PMID: 10513127.

Lockwood, C. J. (2001). Biochemical predictors of prematurity. *Frontiers of Hormone Research*, 27:258–268. PMID: 11450431.

Lodge, S. and Sproat, J. E. (1981). Resting membrane potentials of pacemaker and non pacemaker areas in rat uterus. *Life Sciences*, 28(20):2251–2256. PMID: 7253820.

Lodish, H., Berk, A., Kaiser, C. A., Krieger, M., Scott, M. P., Bretscher, A., Ploegh, H., and Matsudaira, P. (2007). *Molecular Cell Biology*. W. H. Freeman, 6th edition.

Lowery, C. L., Eswaran, H., Murphy, P., and Preissl, H. (2006). Fetal magnetoencephalography. *Seminars in Fetal & Neonatal Medicine*, 11(6):430–436. PMID: 17067862.

Lucovnik, M., Maner, W. L., Chambliss, L. R., Blumrick, R., Balducci, J., Novak-Antolic, Z., and Garfield, R. E. (2011a). Noninvasive uterine electromyography for prediction of preterm delivery. *American Journal of Obstetrics and Gynecology*, 204(3):228.e1–228.e10. PMID: 21145033.

Lucovnik, M., Maner, W. L., and Garfield, R. E. (2011b). Reply. *American Journal of Obstetrics and Gynecology*. PMID: 21861966.

MacQueen, J. (1967). Some methods for classification and analysis of multivariate observations. In Cam, L. M. L. and Neyman, J., editors, *Proceedings of the Fifth Berkeley Symposium on Mathematical Statistics and Probability*, volume 1, page 281. University of California Press.

Maner, W. L. and Garfield, R. E. (2007). Identification of human term and preterm labor using artificial neural networks on uterine electromyography data. *Annals of Biomedical Engineering*, 35(3):465–473. PMID: 17226089.

Maner, W. L., Garfield, R. E., Maul, H., Olson, G., and Saade, G. (2003). Predicting term and preterm delivery with transabdominal uterine electromyography. *Obstetrics and Gynecology*, 101(6):1254–1260. PMID: 12798533.

Maner, W. L., MacKay, L. B., Saade, G. R., and Garfield, R. E. (2006). Characterization of abdominally acquired uterine electrical signals in humans, using a non-linear analytic method. *Medical & Biological Engineering & Computing*, 44(1-2):117–123. PMID: 16929929.

Marque, C., Duchene, J. M., Leclercq, S., Panczer, G. S., and Chaumont, J. (1986). Uterine EHG processing for obstetrical monitoring. *IEEE Transactions on Bio-Medical Engineering*, 33(12):1182–1187. PMID: 3817852.

Marshall, J. M. (1962). Regulation of activity in uterine smooth muscle. *Physiological Reviews. Supplement*, 5:213–227. PMID: 14470252.

Maul, H., Maner, W. L., Saade, G. R., and Garfield, R. E. (2003). The physiology of uterine contractions. *Clinics in Perinatology*, 30(4):665–676, v. PMID: 14714918.

McGregor, J. A., Jackson, G. M., Lachelin, G. C., Goodwin, T. M., Artal, R., Hastings, C., and Dullien, V. (1995). Salivary estriol as risk assessment for preterm labor: a prospective trial. *American Journal of Obstetrics and Gynecology*, 173(4):1337–1342. PMID: 7485350.

McNamara, H. M. (2003). Problems and challenges in the management of preterm labour. *BJOG: An International Journal of Obstetrics and Gynaecology*, 110 Suppl 20:79–85. PMID: 12763118.

Mertins, A. (1999). *Signal Analysis: Wavelets, Filter Banks, Time-Frequency Transforms and Applications*. Wiley, revised edition.

Miller, S. M., Garfield, R. E., and Daniel, E. E. (1989). Improved propagation in myometrium associated with gap junctions during parturition. *The American Journal of Physiology*, 256(1 Pt 1):C130–141. PMID: 2912131.

Misiti, M., Misiti, Y., Oppenheim, G., and Poggl, J.-M. (2007). *Wavelets and their applications*. John Wiley and Sons.

Miyoshi, H., Boyle, M. B., MacKay, L. B., and Garfield, R. E. (1998). Gap junction currents in cultured muscle cells from human myometrium. *American Journal of Obstetrics and Gynecology*, 178(3):588–593. PMID: 9539530.

Osa, T. and Katase, T. (1975). Physiological comparison of the longitudinal and circular muscles of the pregnant rat uterus. *The Japanese Journal of Physiology*, 25(2):153–164. PMID: 1152304.

Pandey, J. N. (1996). *The Hilbert transform of Schwartz distributions and applications*. Wiley-Interscience.

Parkington, H. C. and Coleman, H. A. (2001). Excitability in uterine smooth muscle. *Frontiers of Hormone Research*, 27:179–200. PMID: 11450426.

Peaceman, A. M., Andrews, W. W., Thorp, J. M., Cliver, S. P., Lukes, A., Iams, J. D., Coultrip, L., Eriksen, N., Holbrook, R. H., Elliott, J., Ingardia, C., and Pietrantoni, M. (1997). Fetal fibronectin as a predictor of preterm birth in patients with symptoms: a multicenter trial. *American Journal of Obstetrics and Gynecology*, 177(1):13–18. PMID: 9240576.

Planes, J. G., Morucci, J. P., Grandjean, H., and Favretto, R. (1984). External recording and processing of fast electrical activity of the uterus in human parturition. *Medical & Biological Engineering & Computing*, 22(6):585–591. PMID: 6503388.

Preissl, H. (2005). *Magnetoencephalography*. Gulf Professional Publishing.

Rabotti, C. (2010). *Characterization of uterine activity by electrohysterography*. PhD thesis, Technische Universiteit Eindhoven.

Rabotti, C., Mischi, M., Beulen, L., Oei, G. S., and Bergmans, J. W. M. (2010a). Modeling and identification of the electrohysterographic volume conductor by high-density electrodes. *IEEE Transactions on Bio-Medical Engineering*, 57(3):519–527. PMID: 19884073.

Rabotti, C., Mischi, M., Oei, S. G., and Bergmans, J. W. M. (2010b). Noninvasive estimation of the electrohysterographic action-potential conduction velocity. *IEEE Transactions on Bio-Medical Engineering*, 57(9):2178–2187. PMID: 20460202.

Rabotti, C., Mischi, M., van Laar, J. O. E. H., Oei, G. S., and Bergmans, J. W. M. (2008). Estimation of internal uterine pressure by joint amplitude and frequency analysis of electrohysterographic signals. *Physiological Measurement*, 29(7):829–841. PMID: 18583724.

Rabotti, C., Mischi, M., van Laar, J. O. E. H., Oei, G. S., and Bergmans, J. W. M. (2009). Inter-electrode delay estimators for electrohysterographic propagation analysis. *Physiological Measurement*, 30(8):745–761. PMID: 19550024.

Rabotti, C., Oei, G. S., van T Hooft, J., and Mischi, M. (2011). Electrohysterographic propagation velocity for preterm delivery prediction. *American Journal of Obstetrics and Gynecology*. PMID: 21880294.

Radhakrishnan, N., Wilson, J. D., Lowery, C., Eswaran, H., and Murphy, P. (2000). A fast algorithm for detecting contractions in uterine electromyography. *IEEE Engineering in Medicine and Biology Magazine: The Quarterly Magazine of the Engineering in Medicine & Biology Society*, 19(2):89–94. PMID: 10738666.

Ramon, C., Preissl, H., Murphy, P., Wilson, J. D., Lowery, C., and Eswaran, H. (2005). Synchronization analysis of the uterine magnetic activity during contractions. *Biomedical Engineering Online*, 4:55. PMID: 16197557.

Robinson, S. E., Burbank, M. B., Fife, A. A., Haid, G., Kubik, P. R., Sekachev, I., Taylor, B., Tillotson, M., Vrba, J., Wong, G., Lowery, C. L., Eswaran, H., Wilson, J. D., Murphy, P., and Preissl, H. (2001). A biomagnetic instrument for human reproductive assessment. In *Proceedings of the 12th international conference in biomagnetism*, pages 919–922, Espoo, Finland. Nenonent, J et al.

Rogalla, H. and Barker, A. T. (1991). *Biomagnetism: superconducting sensors and instrumentation : concerted action on Biomagnetism Medical and Health Research Programme of the European Communities*. The Institute of Physical Sciences in Medicine.

Sanborn, B. M. (2000). Relationship of ion channel activity to control of myometrial calcium. *Journal of the Society for Gynecologic Investigation*, 7(1):4–11. PMID: 10732311.

Schreiber, T. and Schmitz, A. (2000). Surrogate time series. *Phys. D*, 142(3-4):346–382.

Shannon, C. E. and Weaver, W. (1998). *The Mathematical Theory of Communication*. University of Illinois Press, 1st edition.

Sims, S. M., Daniel, E. E., and Garfield, R. E. (1982). Improved electrical coupling in uterine smooth muscle is associated with increased numbers of gap junctions at parturition. *The Journal of General Physiology*, 80(3):353–375. PMID: 7142952.

Smilde, A. K., Kiers, H. A. L., Bijlsma, S., Rubingh, C. M., and van Erk, M. J. (2009). Matrix correlations for high-dimensional data: the modified RV-coefficient. *Bioinformatics (Oxford, England)*, 25(3):401–405. PMID: 19073588.

Smyth, C. N. (1957). The guard-ring tocodynamometer; absolute measurement of intra-amniotic pressure by a new instrument. *The Journal of Obstetrics and Gynaecology of the British Empire*, 64(1):59–66. PMID: 13406636.

Spaetling, L., Behrens, C., Hasenburg, A., and Fallenstein, F. (1997). External four channel tocography in preterm labor. first results. *Journal of Perinatal Medicine*, 25(1):43–48. PMID: 9085202.

Suciu, L., Popescu, L. M., and Gherghiceanu, M. (2007). Human placenta: de visu demonstration of interstitial cajal-like cells. *Journal of Cellular and Molecular Medicine*, 11(3):590–597. PMID: 17635651.

Tezuka, N., Ali, M., Chwalisz, K., and Garfield, R. E. (1995). Changes in transcripts encoding calcium channel subunits of rat myometrium during pregnancy. *The American Journal of Physiology*, 269(4 Pt 1):C1008–1017. PMID: 7485440.

Tomiyasu, B. A., Chen, C. J., and Marshall, J. M. (1988). Comparison of the activity of circular and longitudinal myometrium from pregnant rats: co-ordination between muscle layers. *Clinical and Experimental Pharmacology & Physiology*, 15(9):647–656. PMID: 3271630.

Ulusar, U. D., Govindan, R. B., Wilson, J. D., Lowery, C. L., Preissl, H., and Eswaran, H. (2009). Adaptive rule based fetal QRS complex detection using hilbert transform. *Conference Proceedings: Annual International Conference of the IEEE Engineering in Medicine and Biology Society.*, 2009:4666–4669. PMID: 19964648.

Verdenik, I., Pajntar, M., and Leskosek, B. (2001). Uterine electrical activity as predictor of preterm birth in women with preterm contractions. *European Journal of Obstetrics, Gynecology, and Reproductive Biology*, 95(2):149–153. PMID: 11301159.

Vinken, M. P. G. C., Rabotti, C., Mischi, M., and Oei, S. G. (2009). Accuracy of frequency-related parameters of the electrohysterogram for predicting preterm delivery: a review of the literature. *Obstetrical & Gynecological Survey*, 64(8):529–541. PMID: 19624864.

Vrba, J., McCubbin, J., Govindan, R. B., Vairavan, S., Murphy, P., Preissl, H., Lowery, C. L., and Eswaran, H. (2012). Removal of interference from fetal MEG by frequency dependent subtraction. *NeuroImage*, 59(3):2475–2484. PMID: 21930216.

Wikipedia contributors (2012). Action potential. Page Version ID: 501929972.

Wolfs, G. and Rottinghuis, H. (1970). Electrical and mechanical activity of the human uterus during labour. *Archiv für Gynäkologie*, 208(4):373–385. PMID: 5538124.

Wolfs, G. M. J. A. and Leeuwen, M. (1979). Electromyographic observations on the human uterus during labour. *Acta Obstetricia et Gynecologica Scandinavica*, 58(S90):1–61.

Word, R. A. (1995). Myosin phosphorylation and the control of myometrial contraction/relaxation. *Seminars in Perinatology*, 19(1):3–14. PMID: 7754409.